



(19) **United States**  
(12) **Patent Application Publication**  
Wong et al.

(10) **Pub. No.: US 2014/0031697 A1**  
(43) **Pub. Date: Jan. 30, 2014**

(54) **DIAGNOSTIC AND TREATMENT METHODS USING COHERENT ANTI-STOKES RAMAN SCATTERING (CARS)-BASED MICROENDOSCOPIC SYSTEM**

(71) Applicant: **The Methodist Hospital Research Institute, Houston, TX (US)**

(72) Inventors: **Stephen T.C. Wong, Missouri City, TX (US); Zhiyong Wang, Sugar Land, TX (US); Ganesh Palpattu, Houston, TX (US); Liang Gao, Houston, TX (US)**

(73) Assignee: **The Methodist Hospital Research Institute, Houston, TX (US)**

(21) Appl. No.: **13/838,628**

(22) Filed: **Mar. 15, 2013**

**Related U.S. Application Data**

(60) Division of application No. 13/135,737, filed on Jul. 14, 2011, which is a continuation-in-part of applica-

tion No. PCT/US11/43792, filed on Jul. 13, 2011, which is a continuation-in-part of application No. 12/931,142, filed on Jan. 25, 2011.

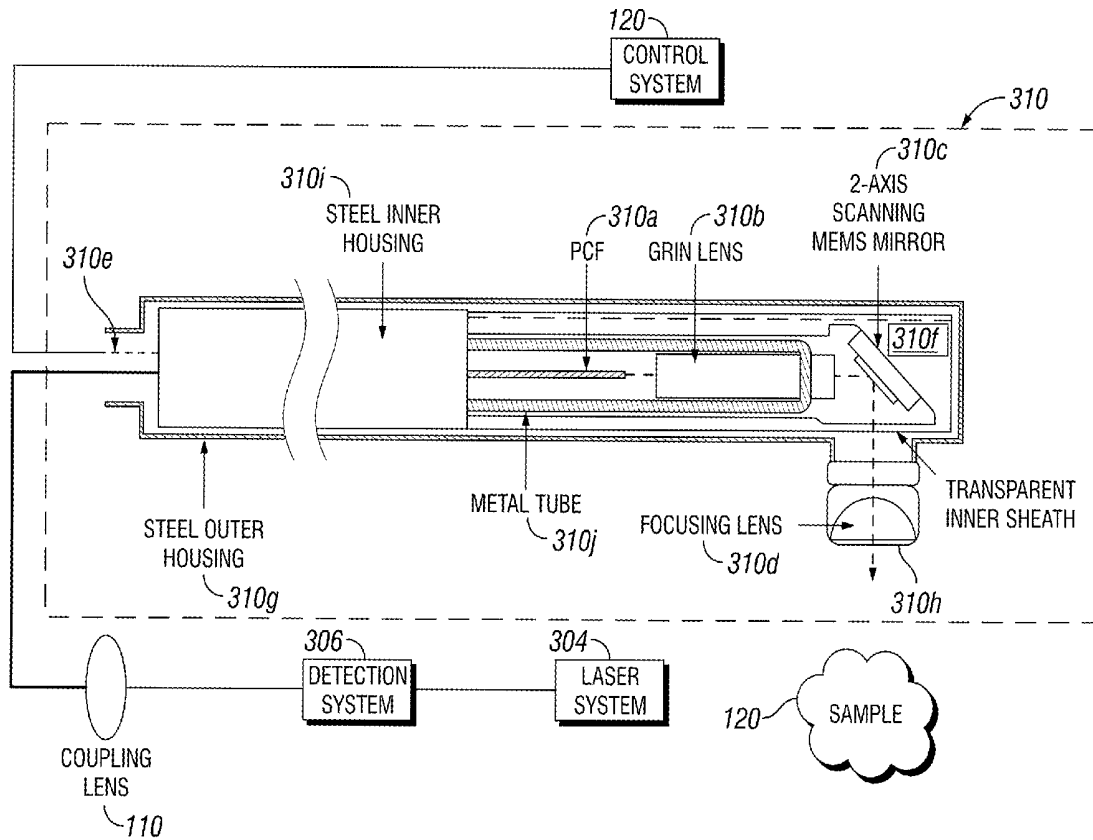
(60) Provisional application No. 61/399,182, filed on Jul. 8, 2010, provisional application No. 61/399,139, filed on Jul. 8, 2010.

**Publication Classification**

(51) **Int. Cl.**  
*A61B 5/00* (2006.01)  
*A61B 18/18* (2006.01)  
(52) **U.S. Cl.**  
CPC ..... *A61B 5/0075* (2013.01); *A61B 18/18* (2013.01)  
USPC ..... **600/476; 606/33**

(57) **ABSTRACT**

An endoscopic microscopic system for collecting and processing a sequence of images in order to provide diagnosis and treatment is disclosed. Also disclosed are methods for making and using the system in a variety of diagnostic and therapeutic applications.



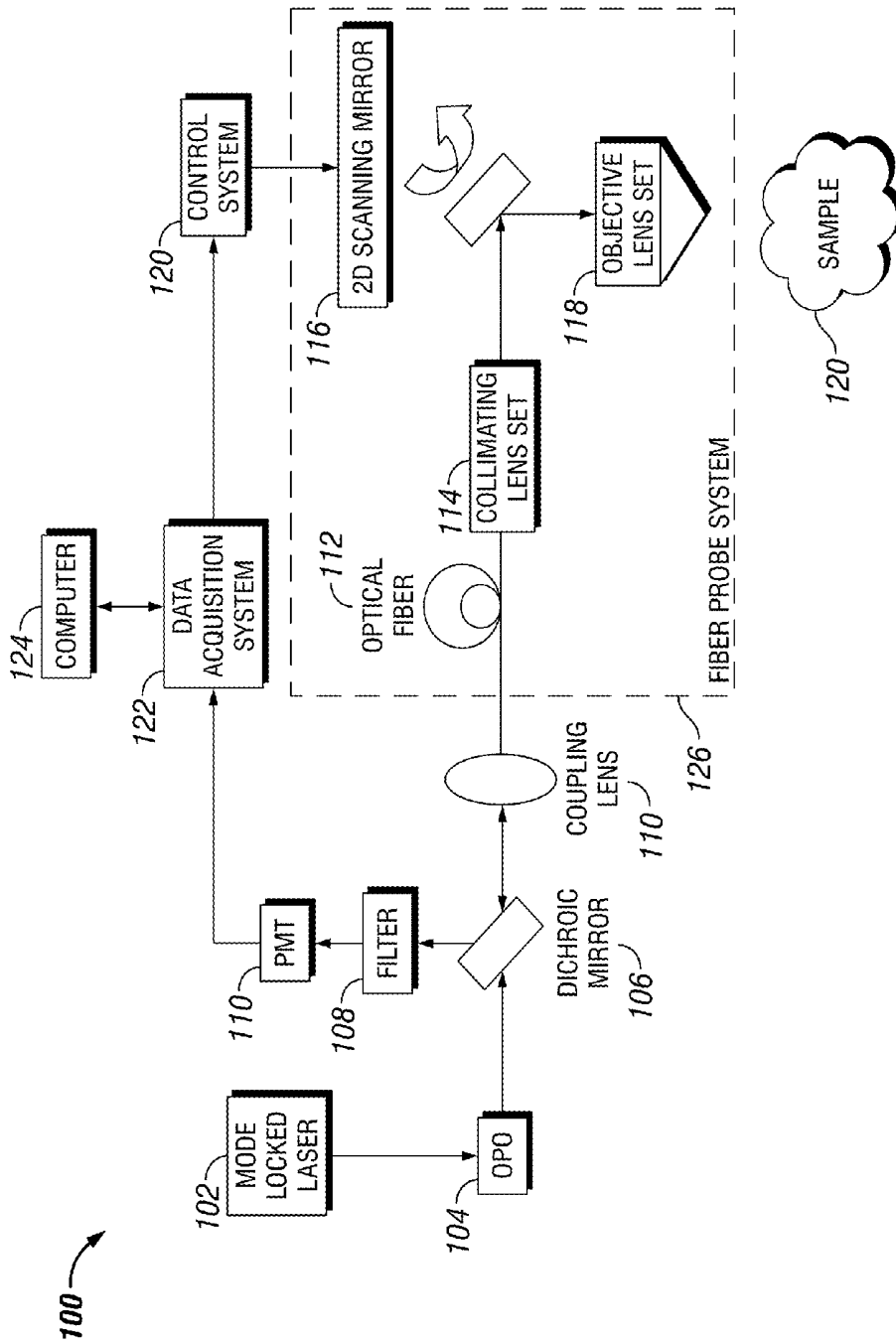


FIG. 1

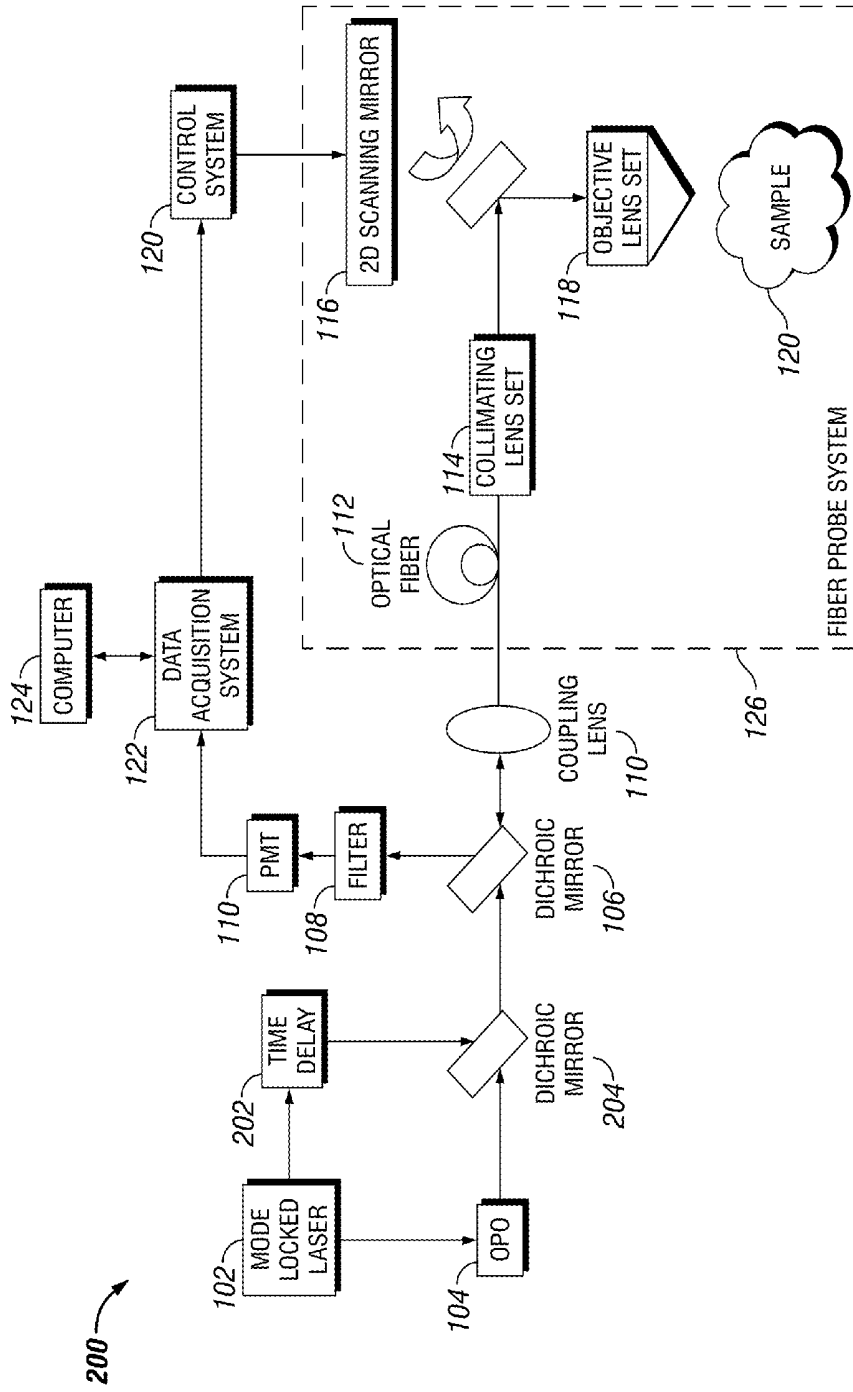


FIG. 2

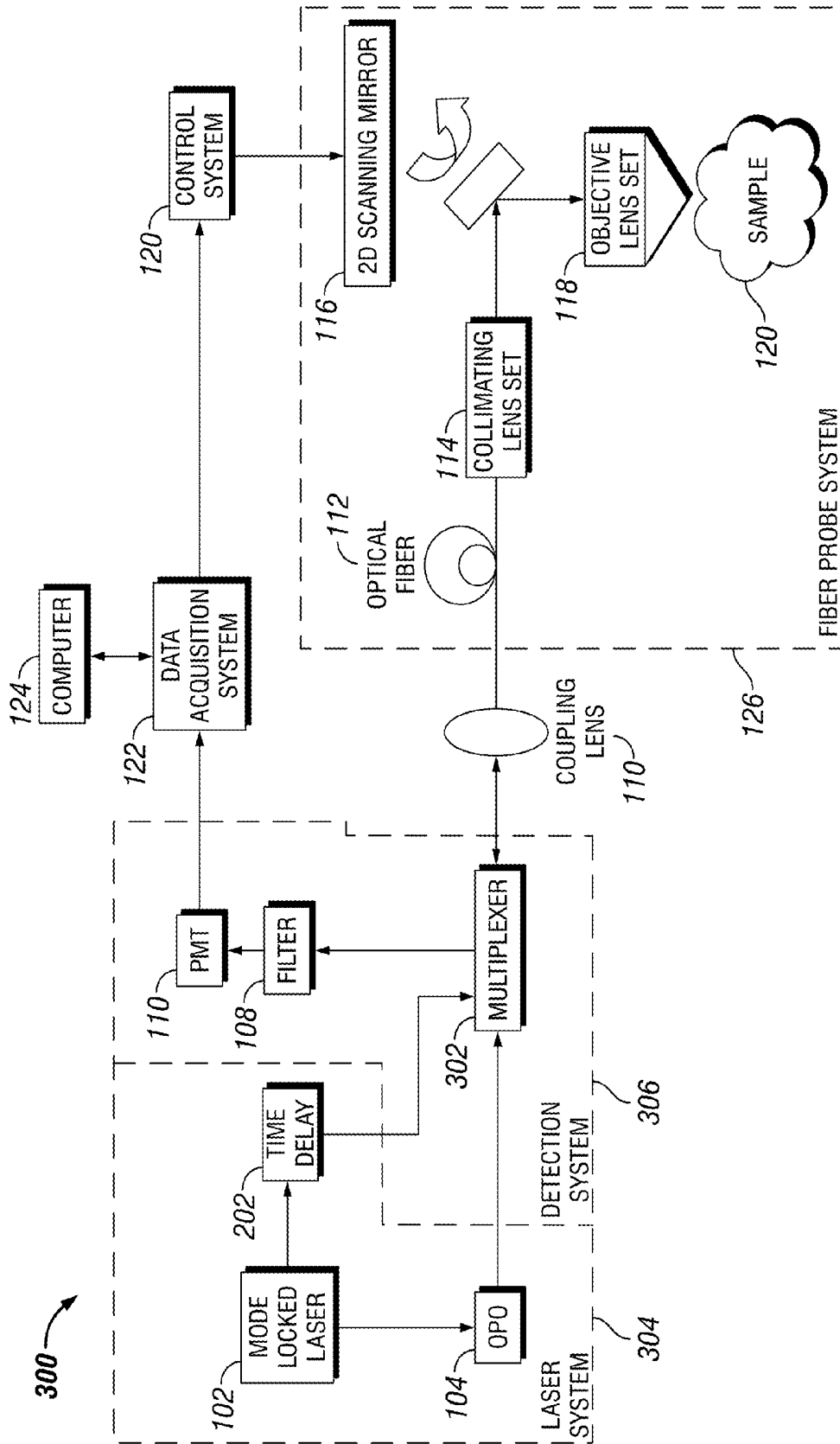


FIG. 3

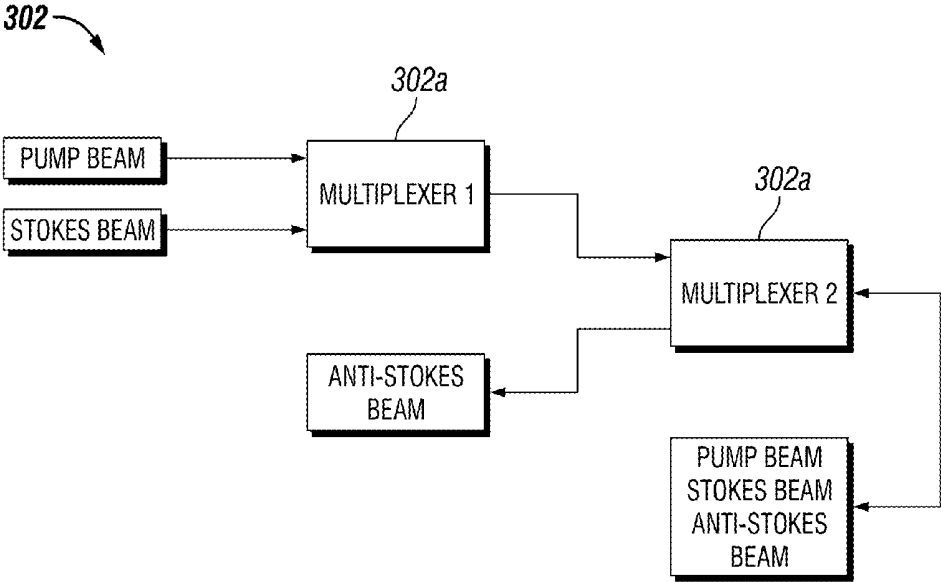


FIG. 3A

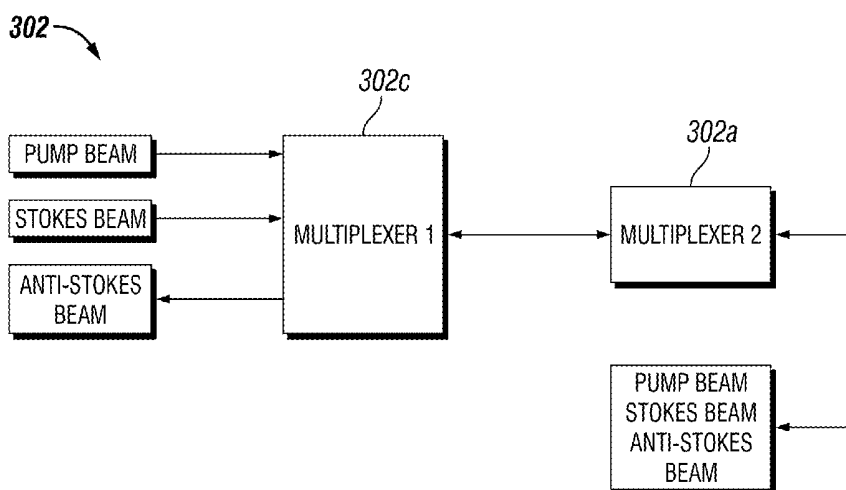


FIG. 3B

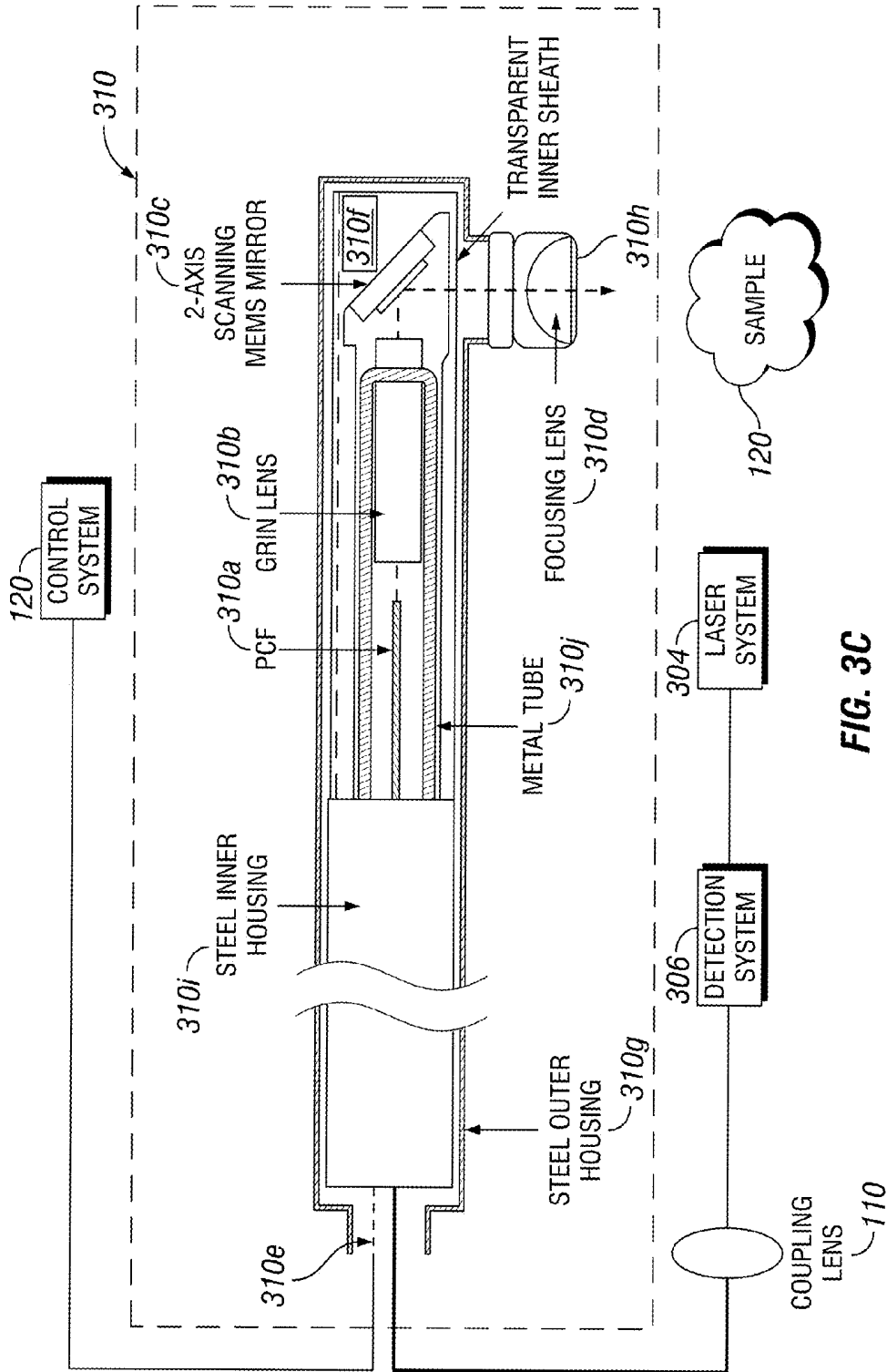


FIG. 3C

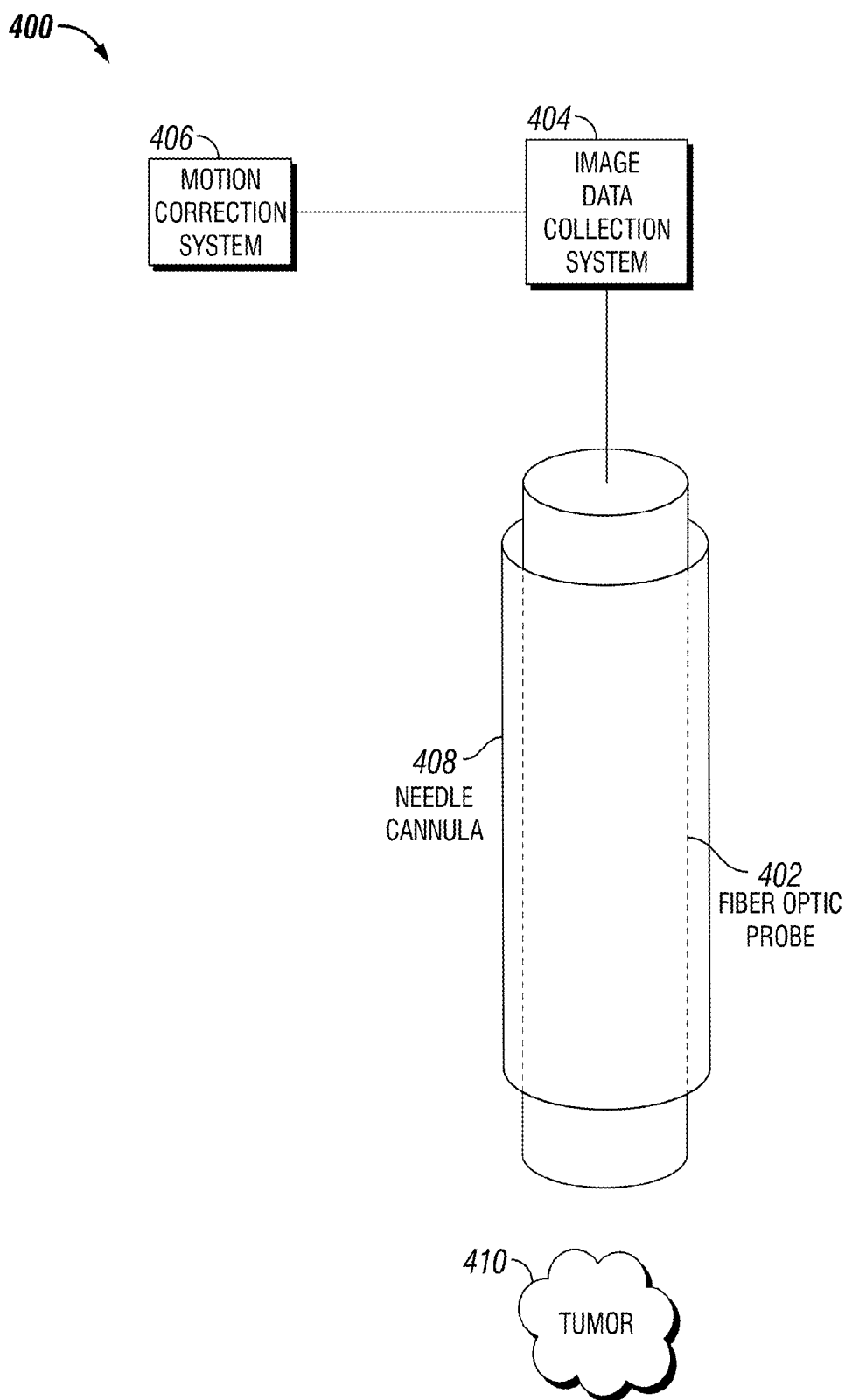


FIG. 4

500

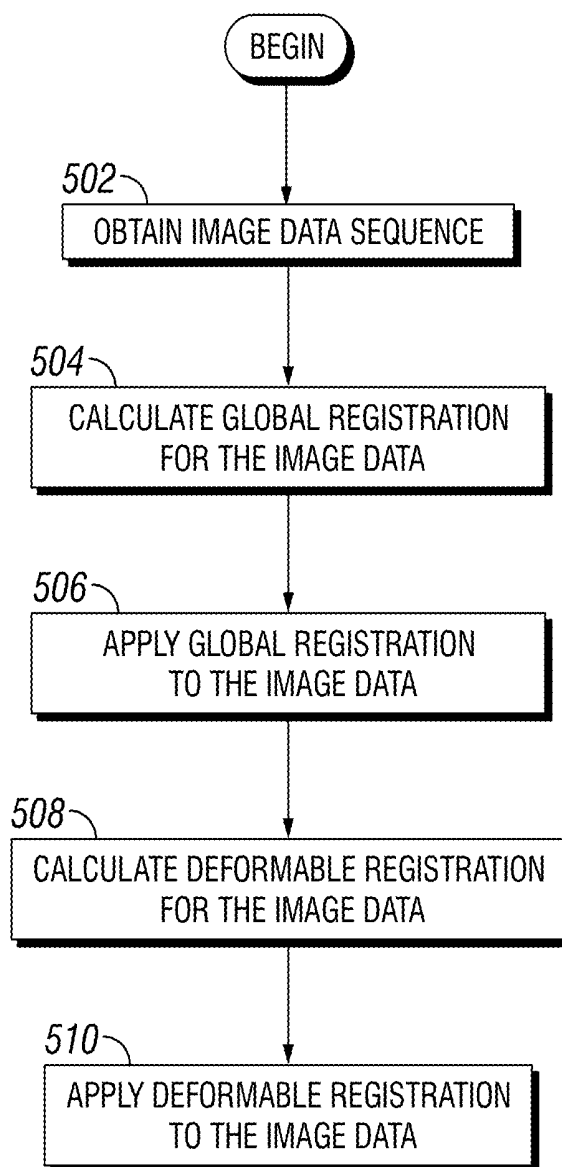


FIG. 5

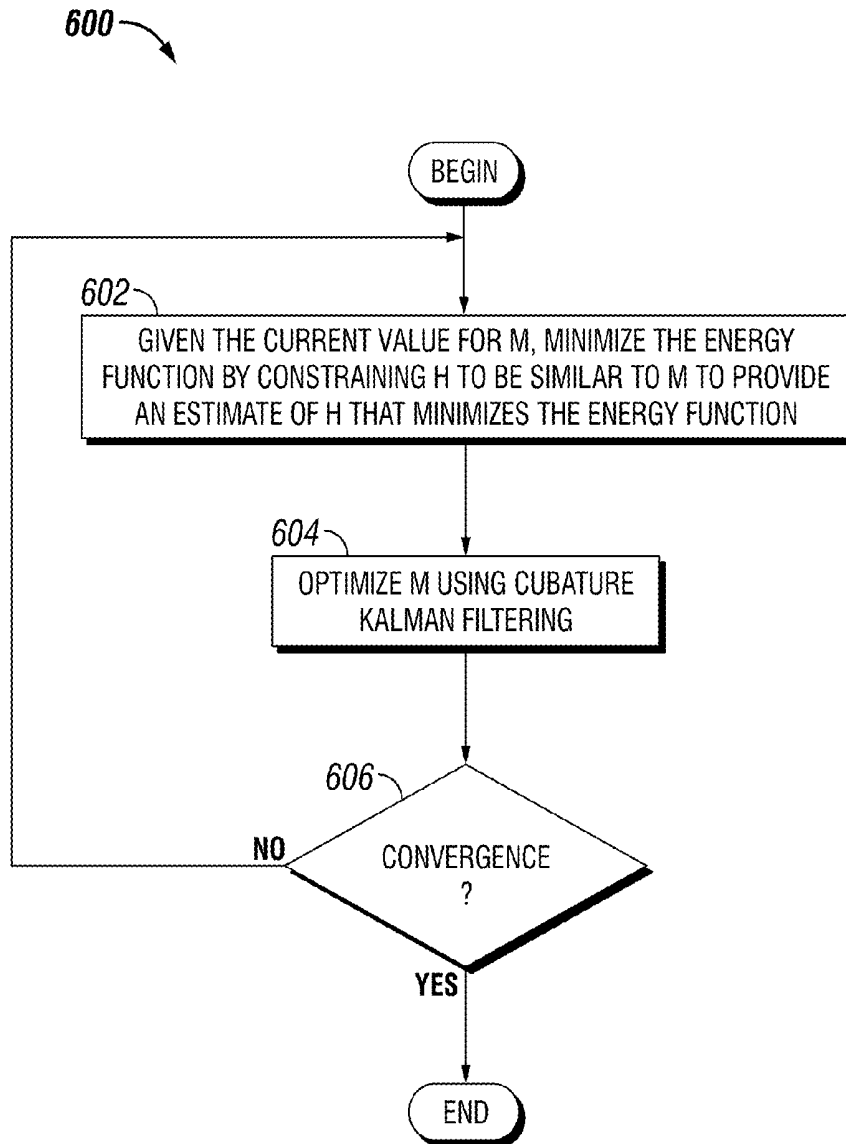
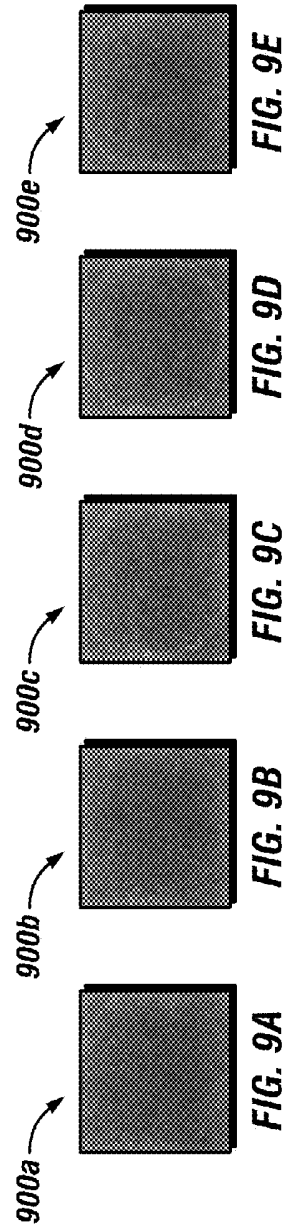
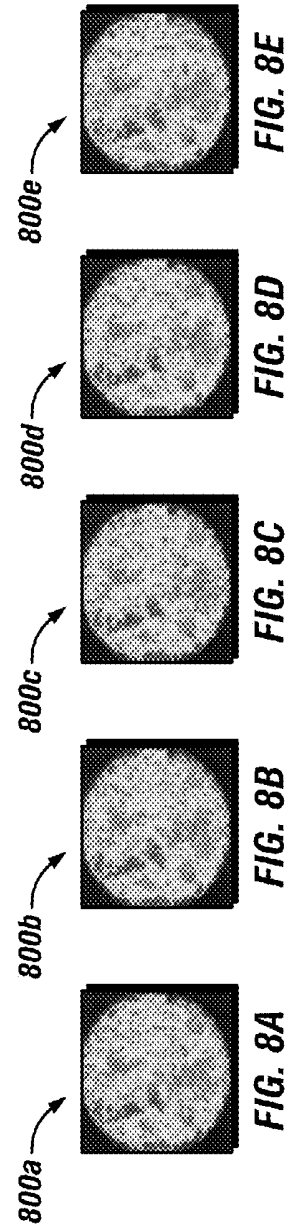
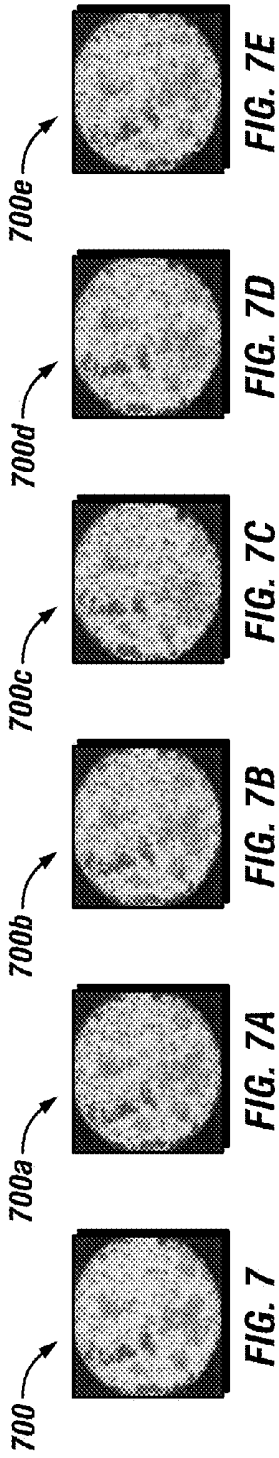


FIG. 6



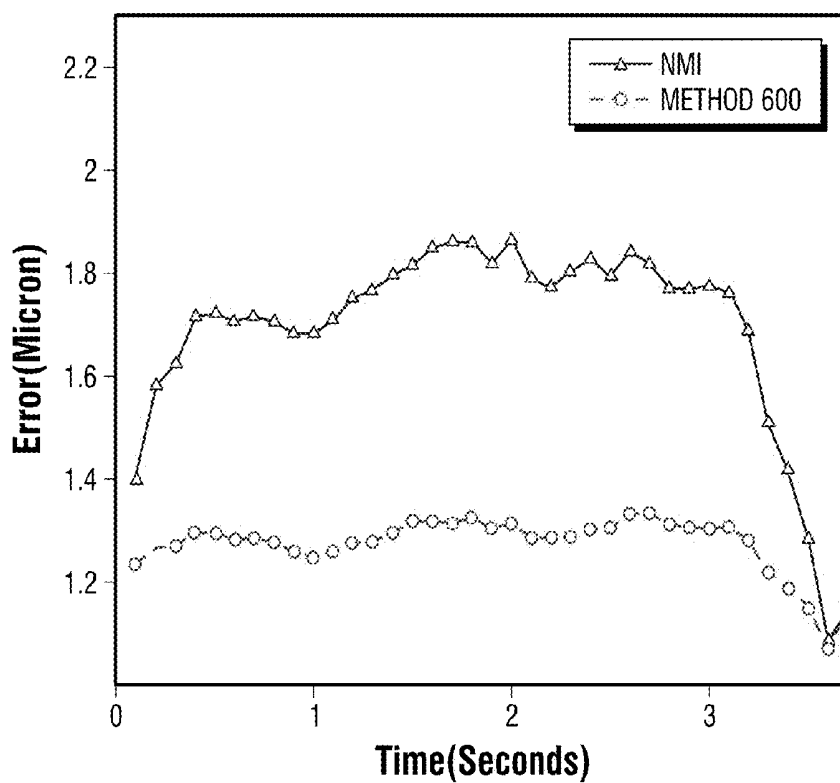
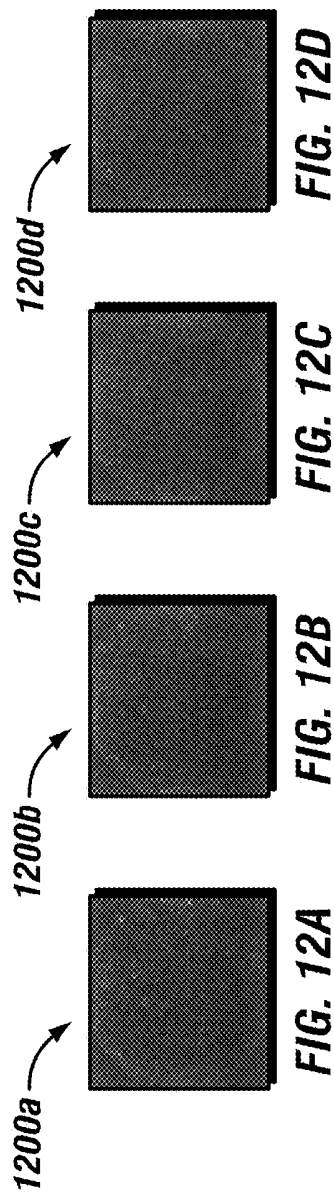
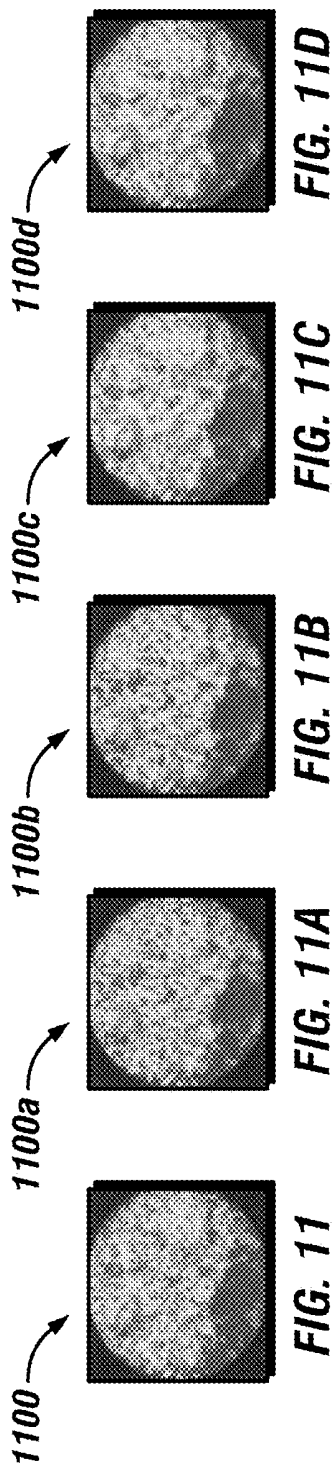


FIG. 10



13/61

1300

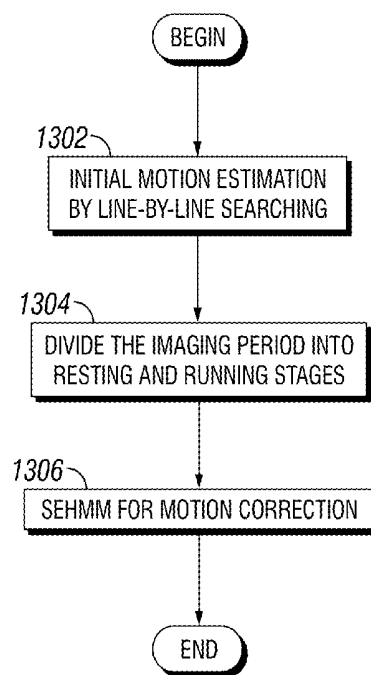


FIG. 13

1400

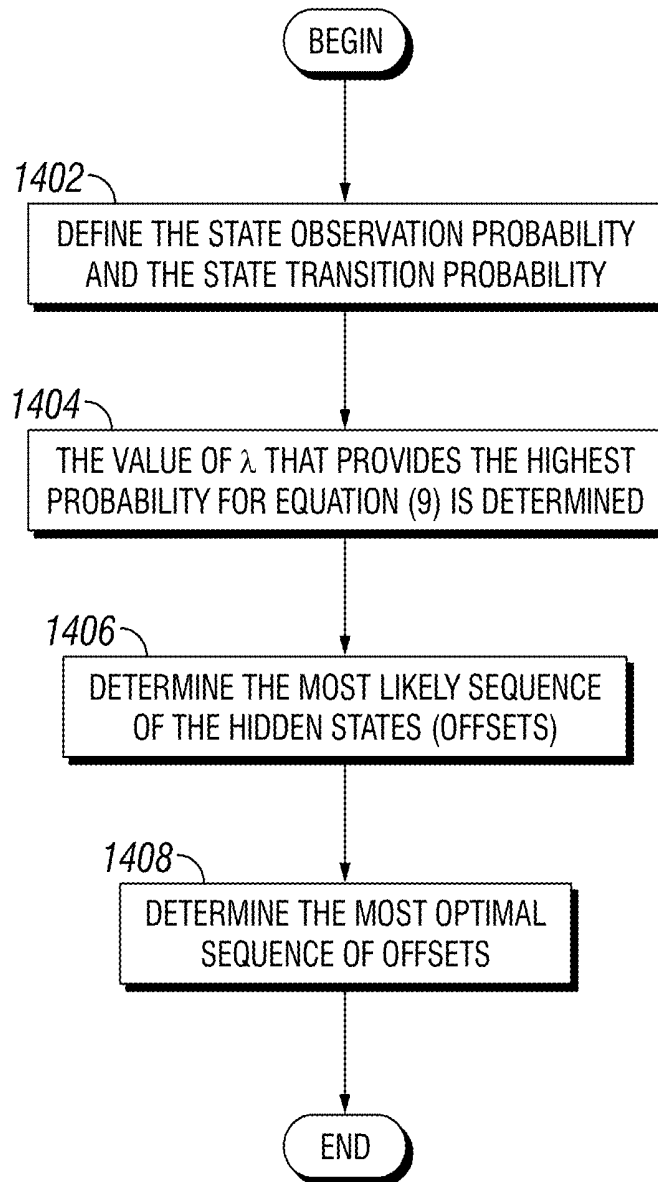


FIG. 14

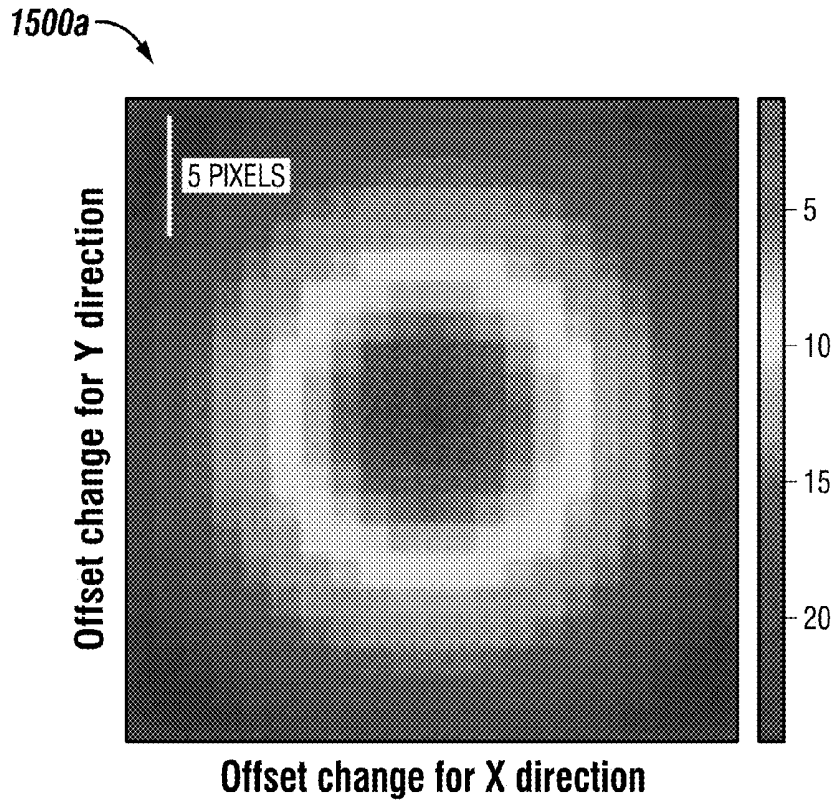


FIG. 15A

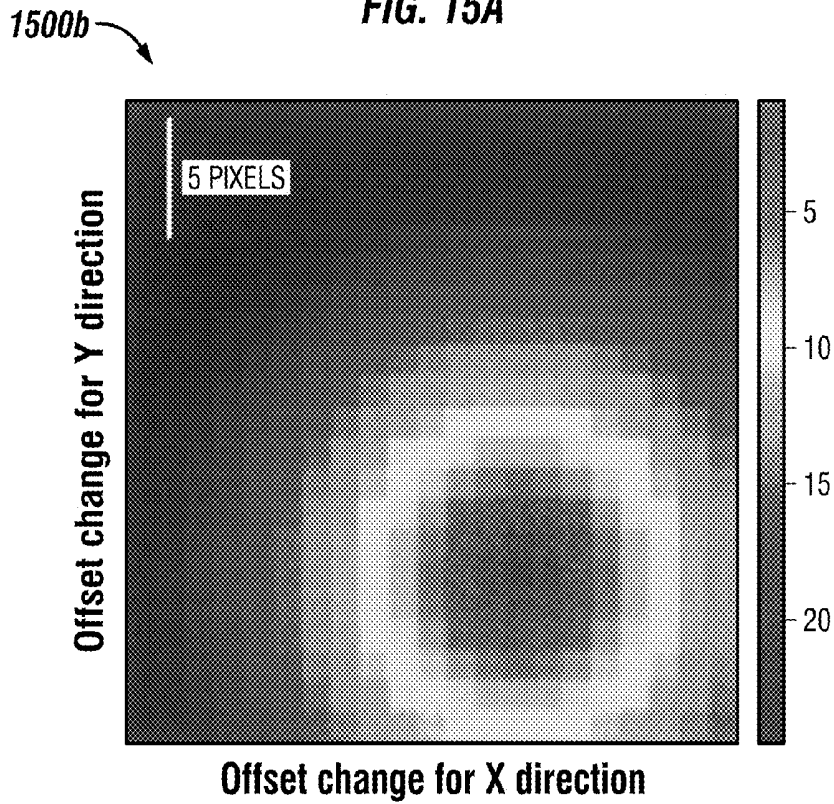
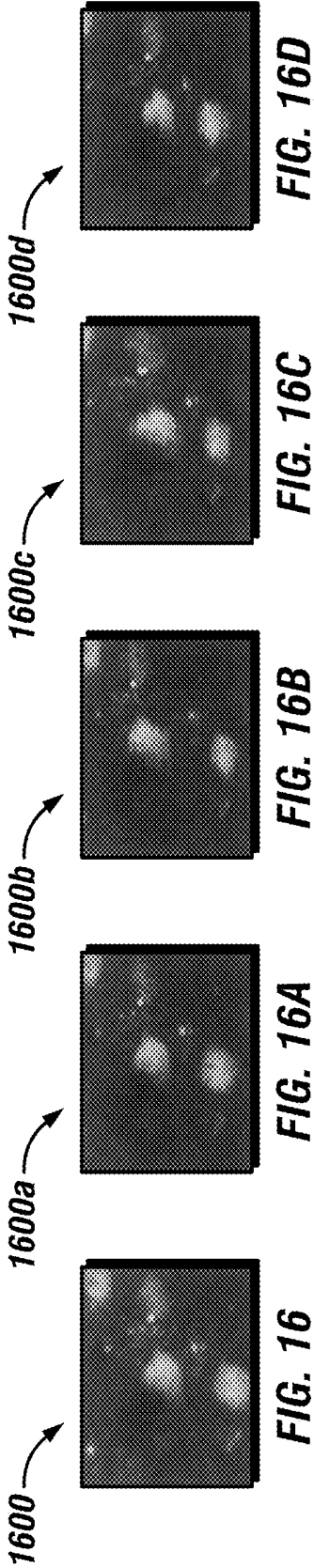


FIG. 15B



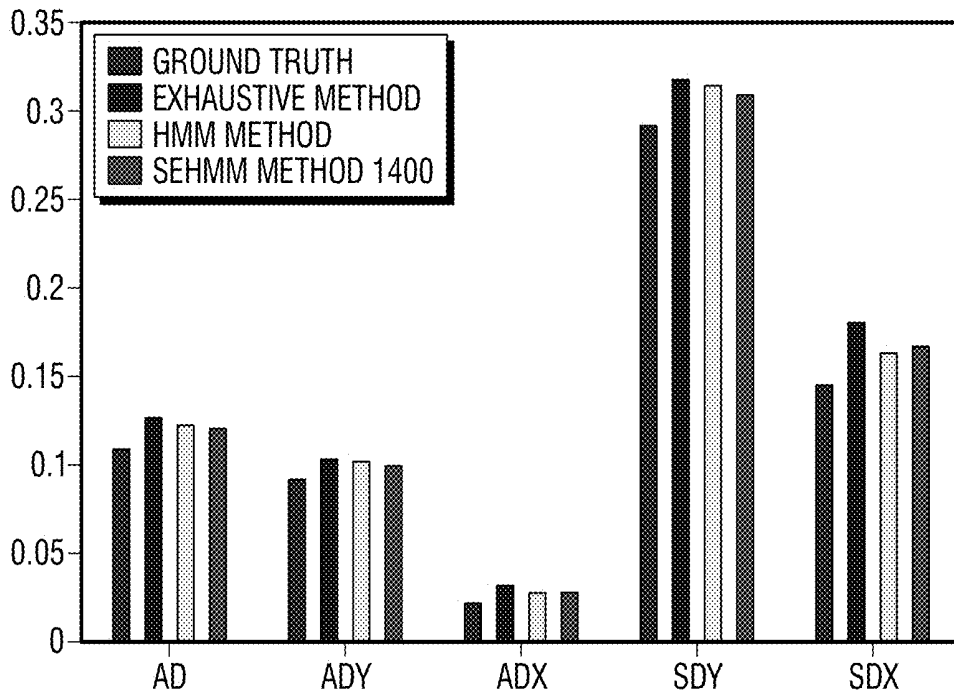


FIG. 17A

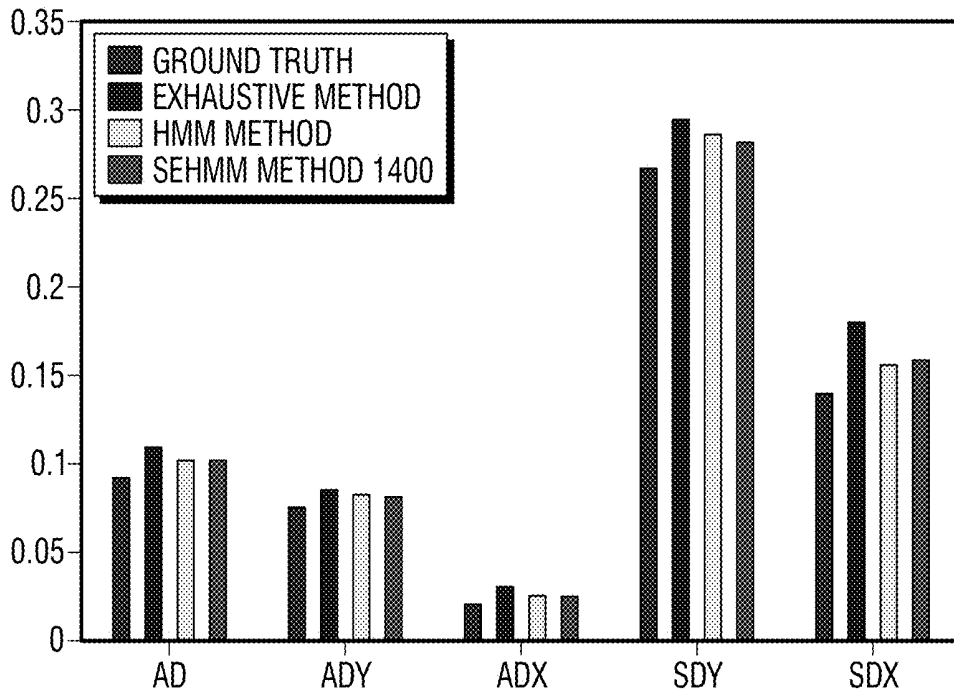


FIG. 17B

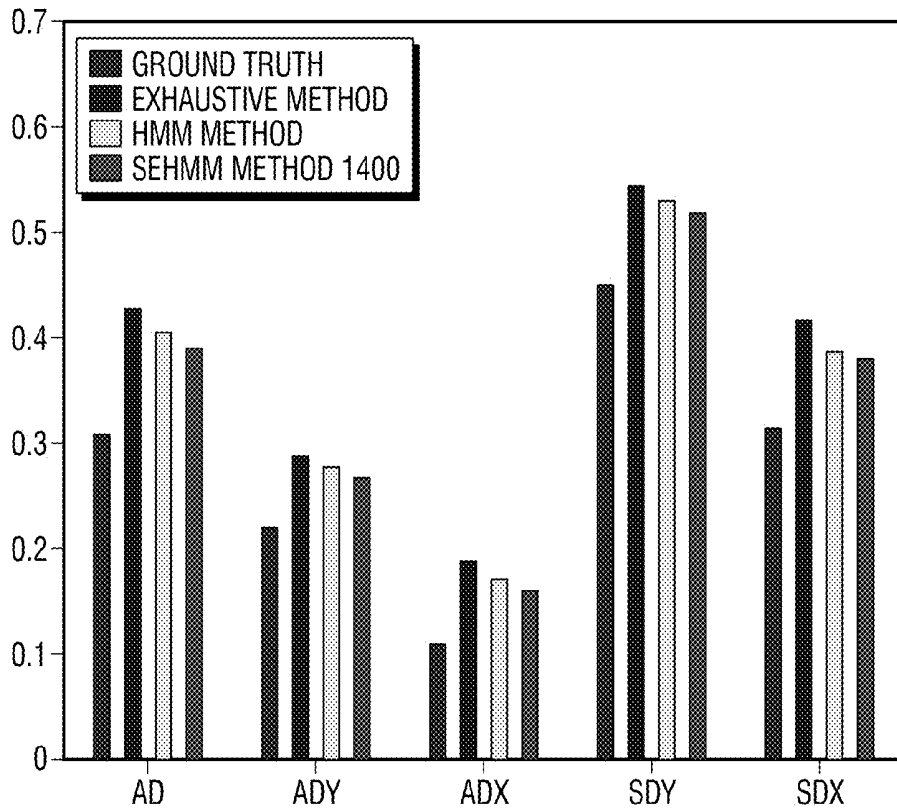


FIG. 17C

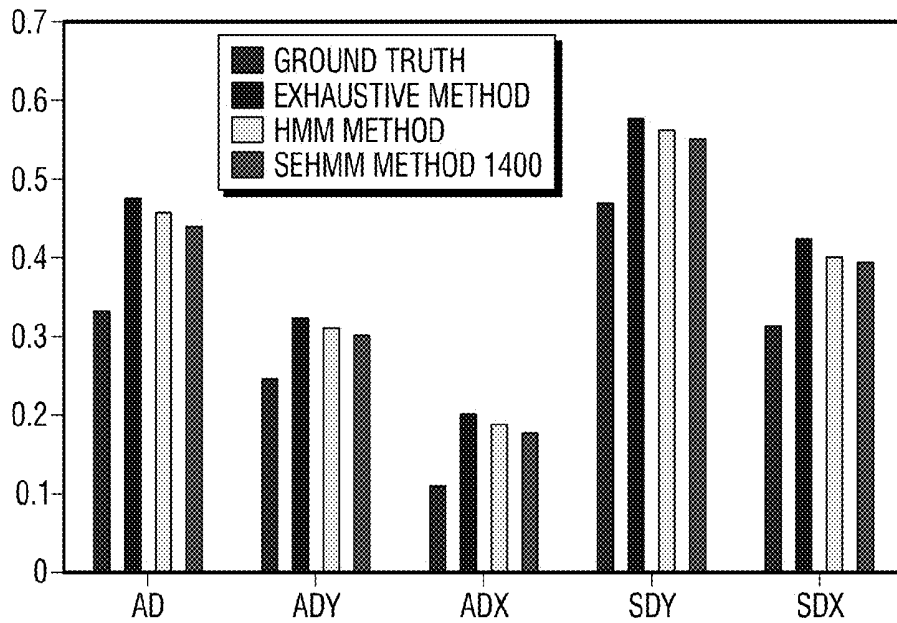


FIG. 17D

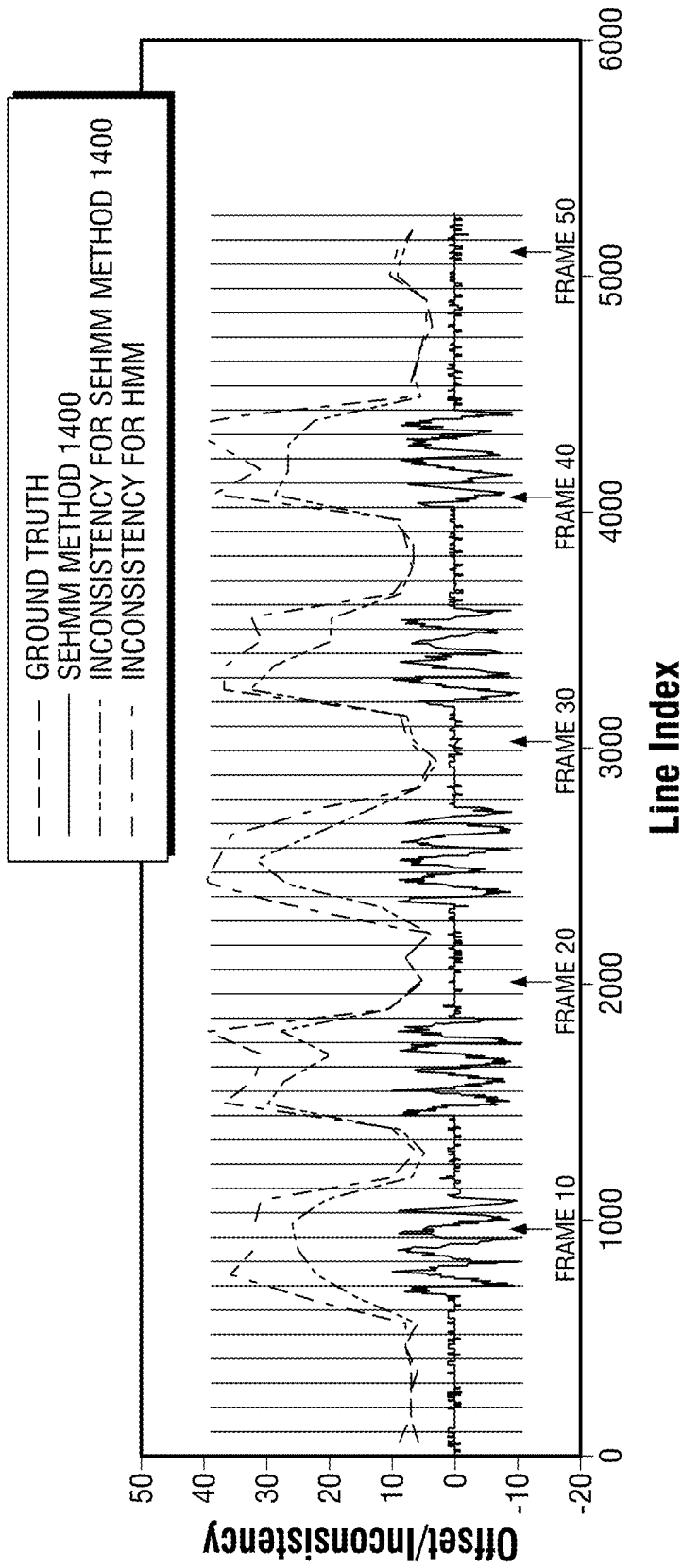
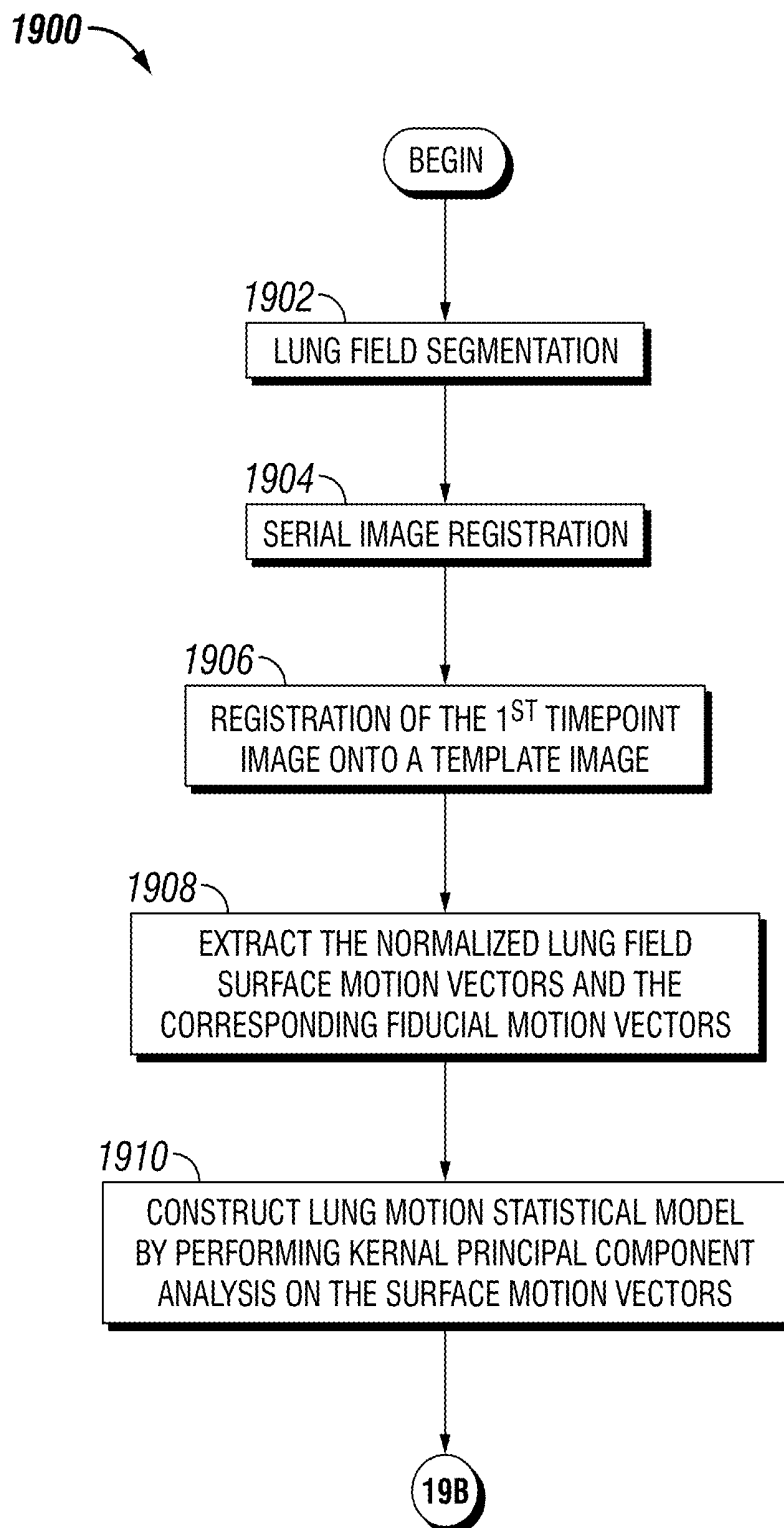
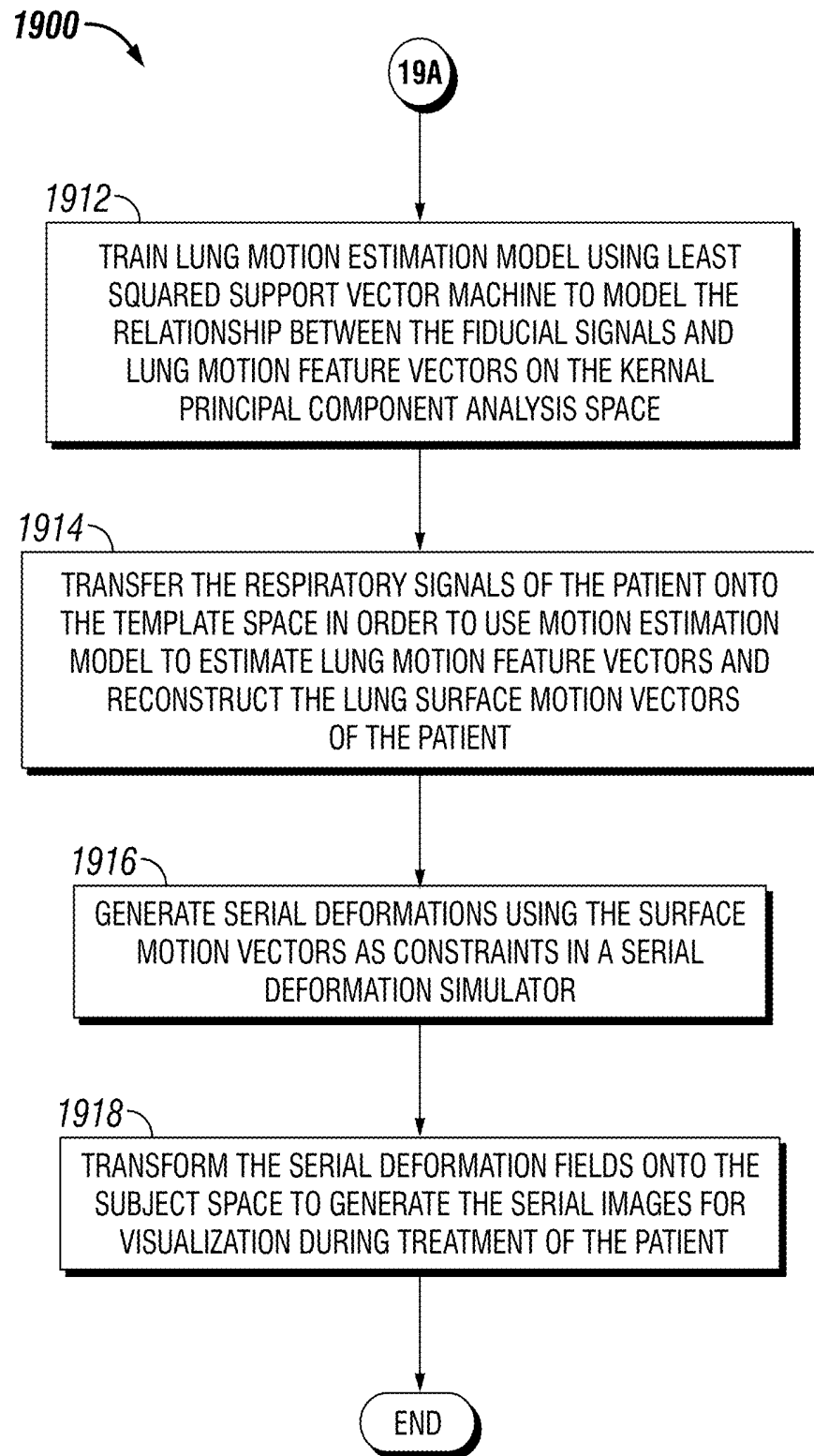


FIG. 18



**FIG. 19A**



**FIG. 19B**

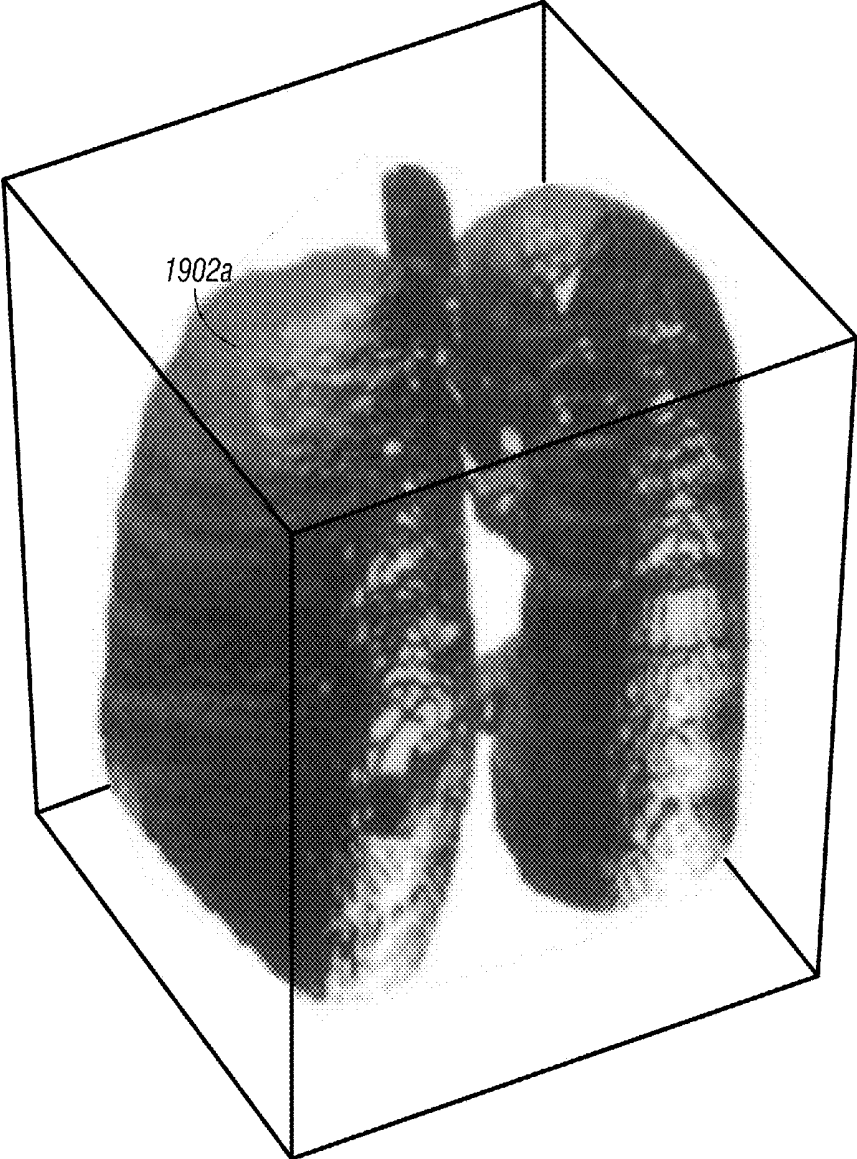


FIG. 20



*FIG. 21*

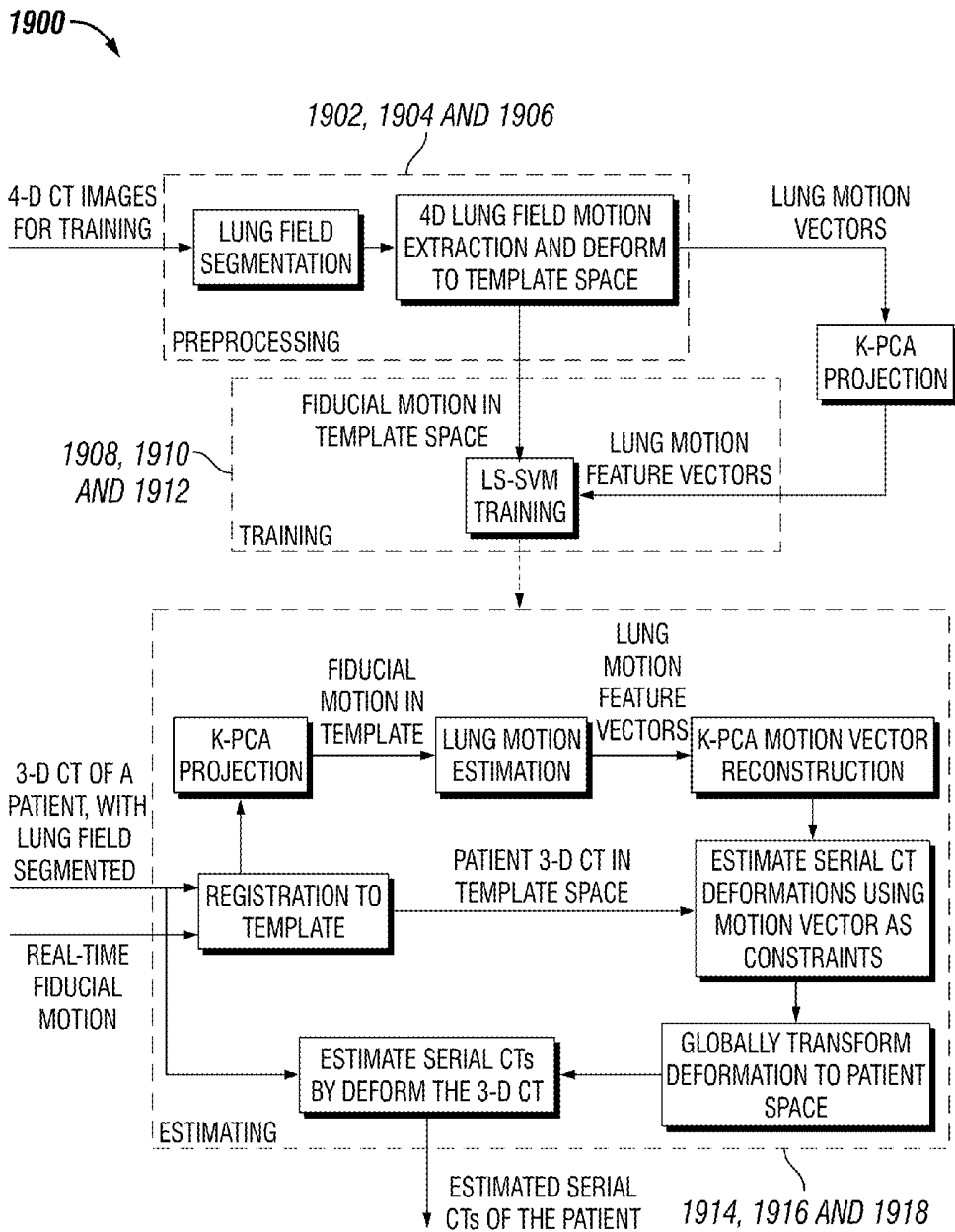
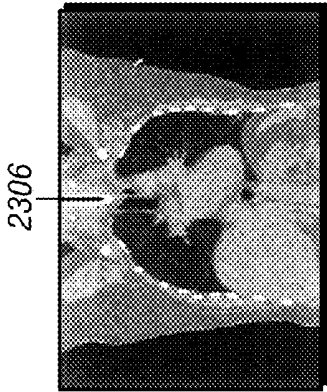
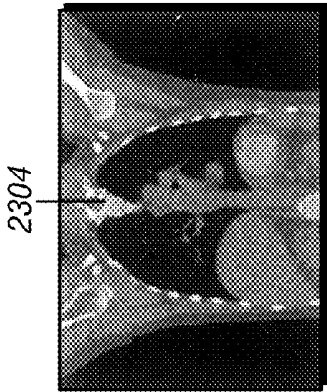


FIG. 22



**FIG. 23A**



**FIG. 23B**

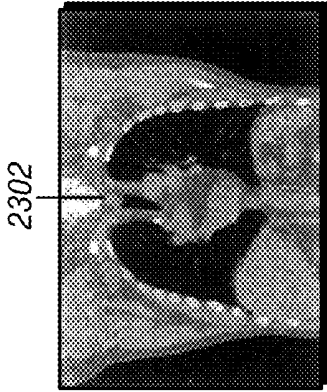


**FIG. 23C**

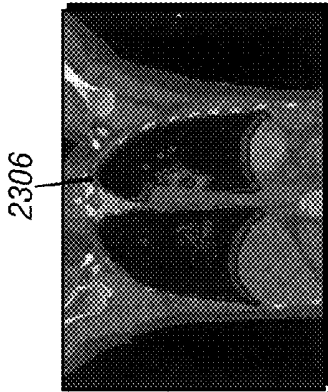


**FIG. 24A**



**FIG. 24B**

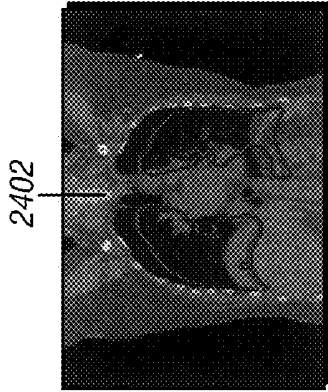


**FIG. 24C**

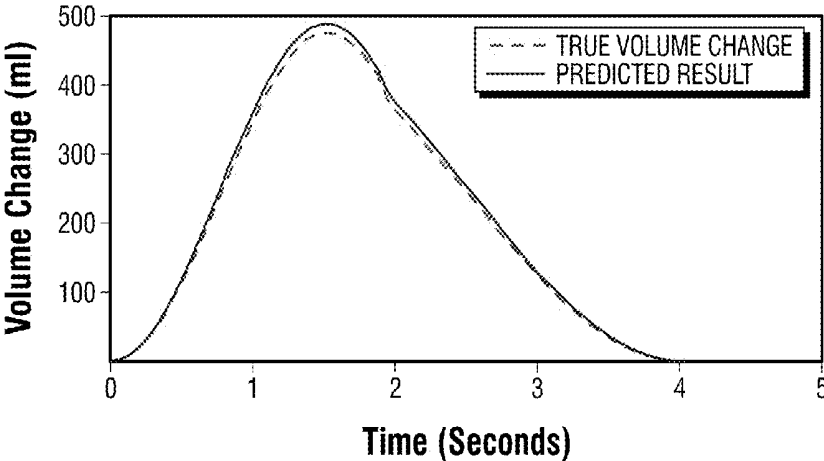


FIG. 25A

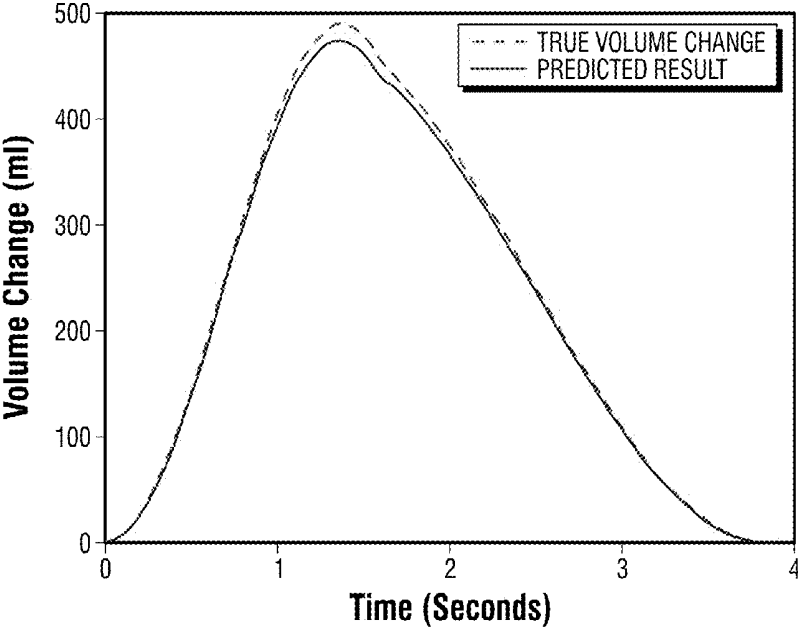


FIG. 25B

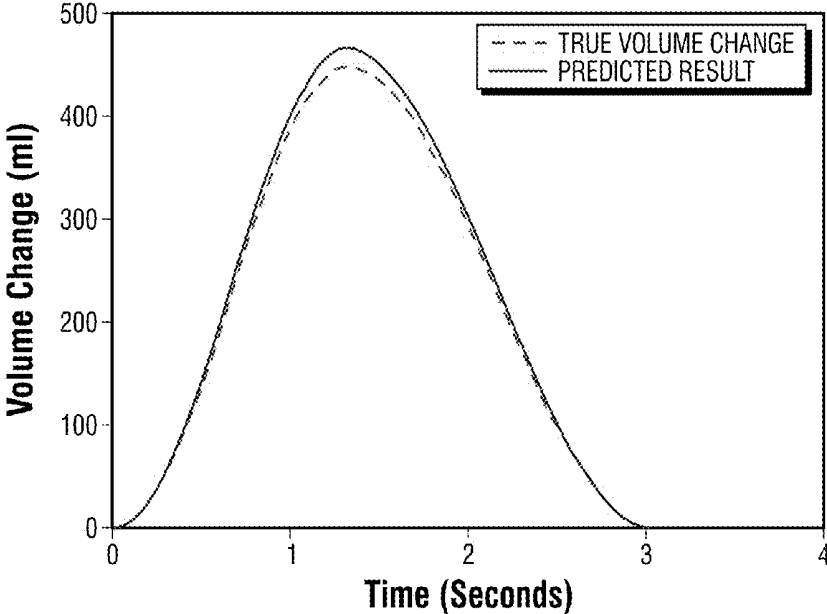


FIG. 25C

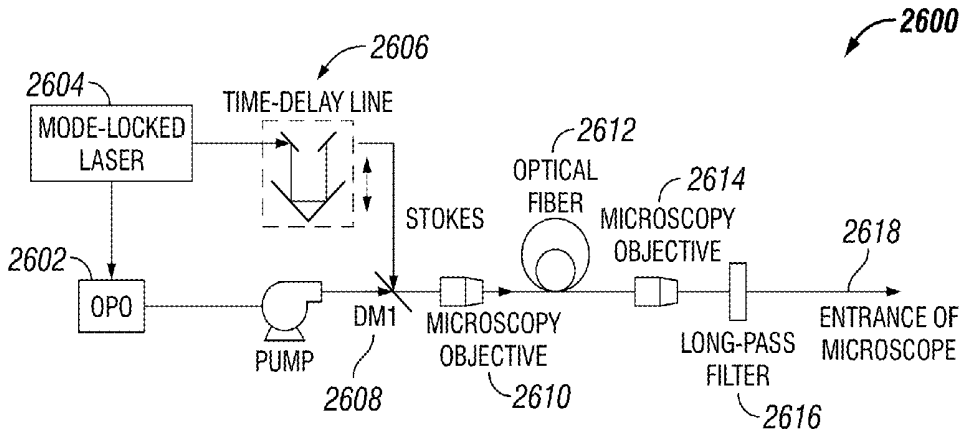


FIG. 26A

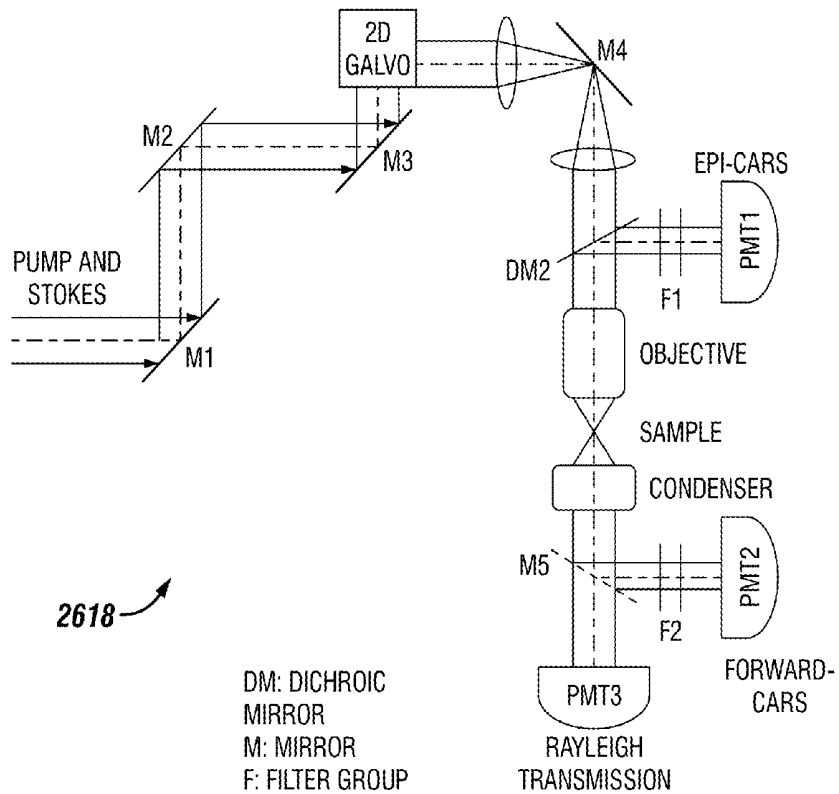


FIG. 26B

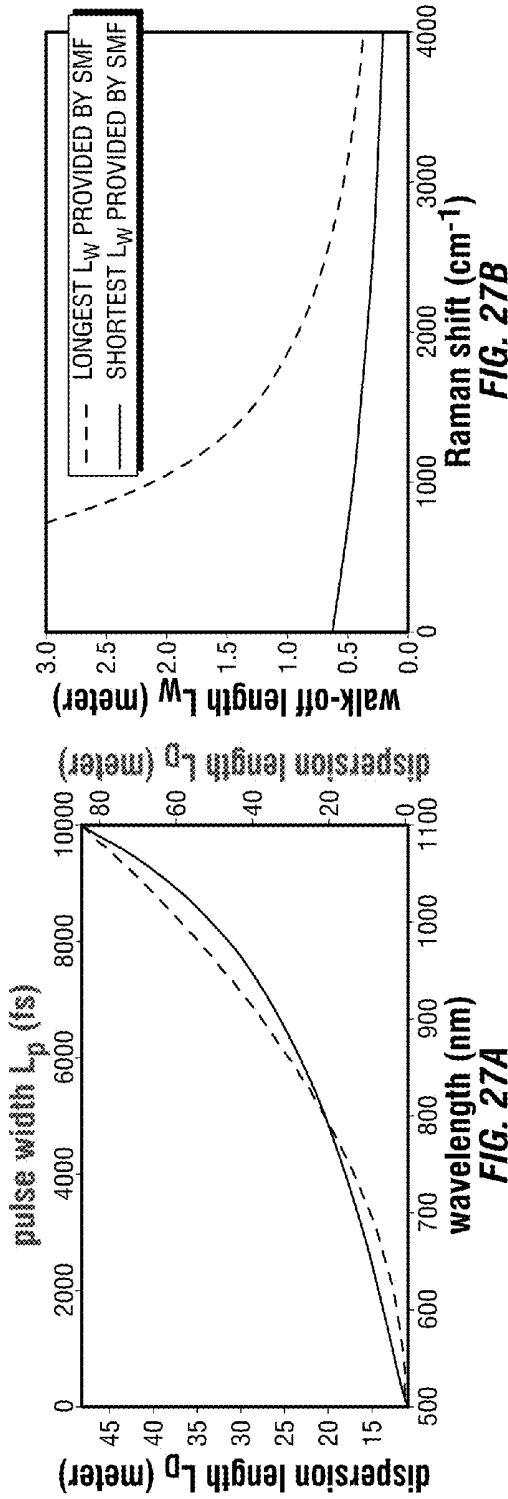


FIG. 27A

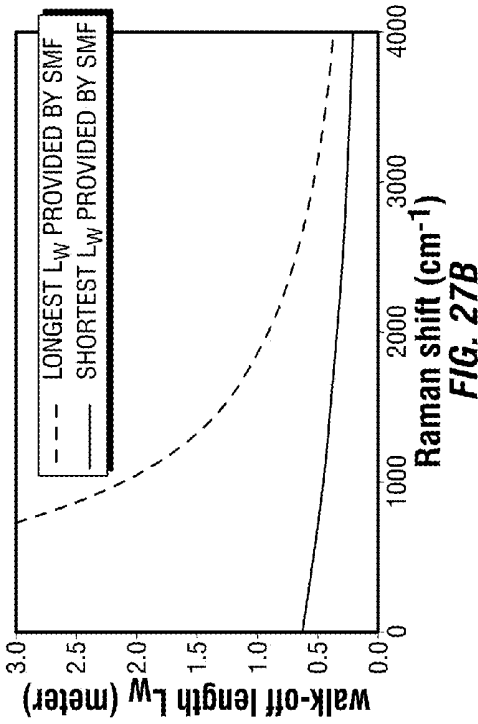


FIG. 27B

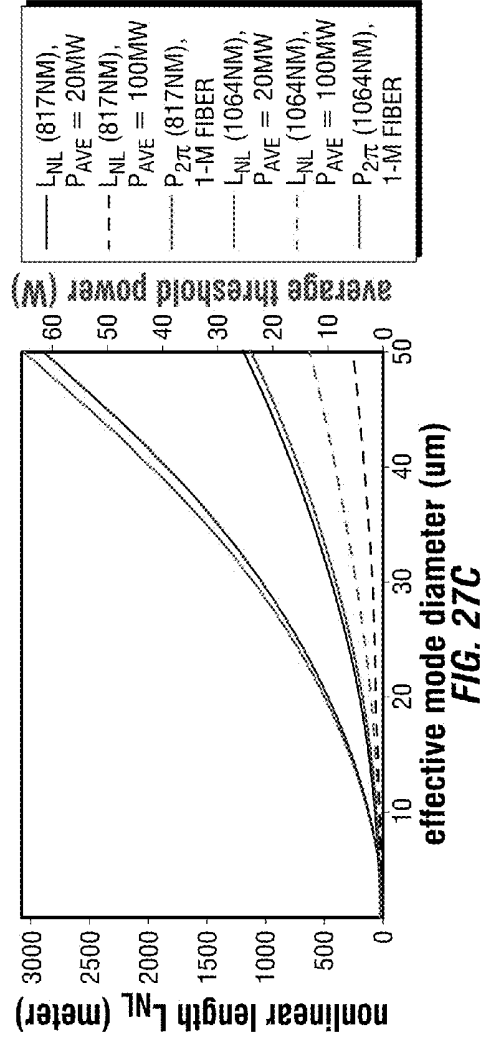


FIG. 27C

—	$L_{NL}$ (817NM),
—	$P_{AVE} = 20\text{MW}$
- - -	$L_{NL}$ (817NM),
- - -	$P_{AVE} = 100\text{MW}$
⋯	$P_{2\pi}$ (817NM),
⋯	1-M FIBER
⋯	$L_{NL}$ (1064NM),
⋯	$P_{AVE} = 20\text{MW}$
⋯	$L_{NL}$ (1064NM),
⋯	$P_{AVE} = 100\text{MW}$
⋯	$P_{2\pi}$ (1064NM),
⋯	1-M FIBER

average threshold power (W)

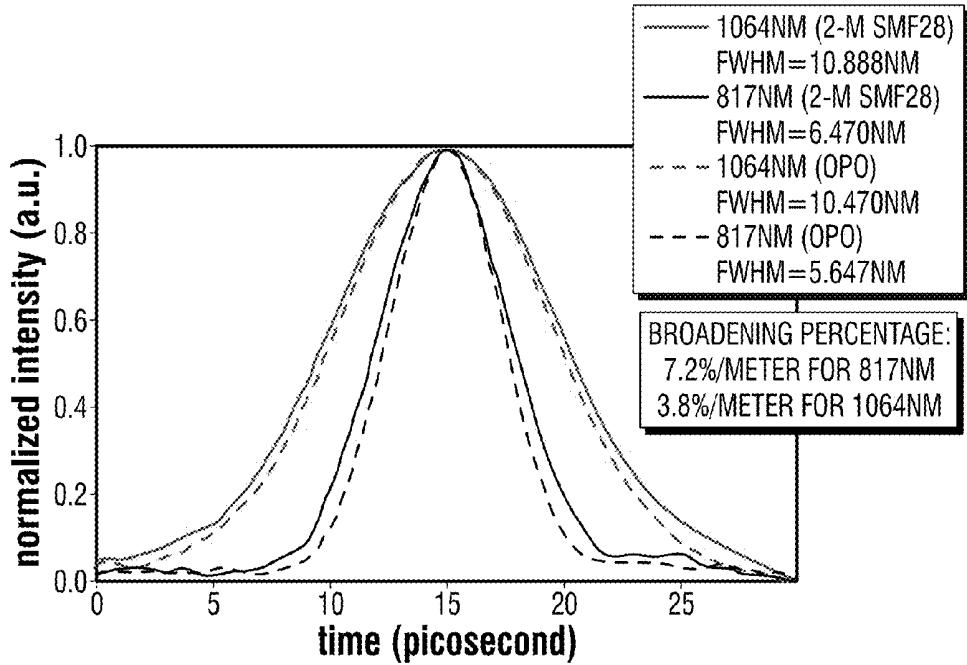


FIG. 28A

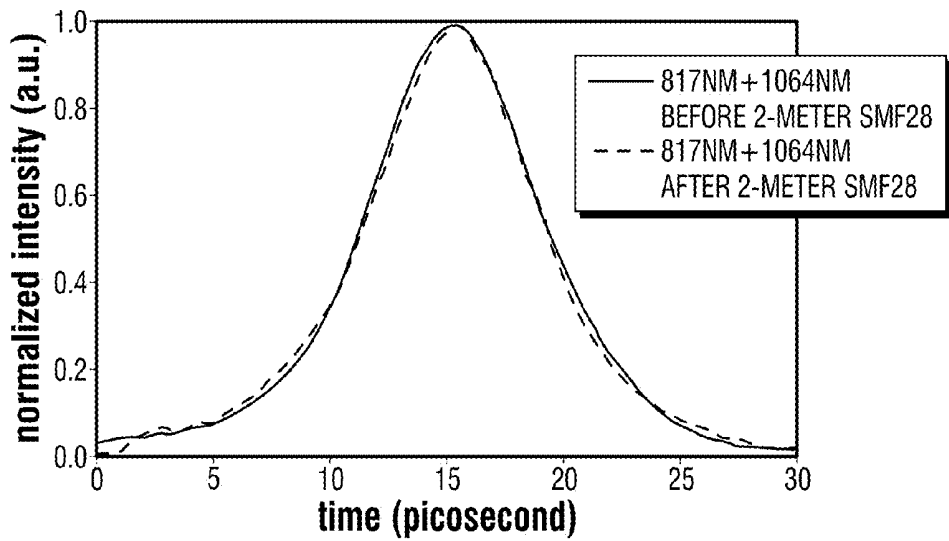
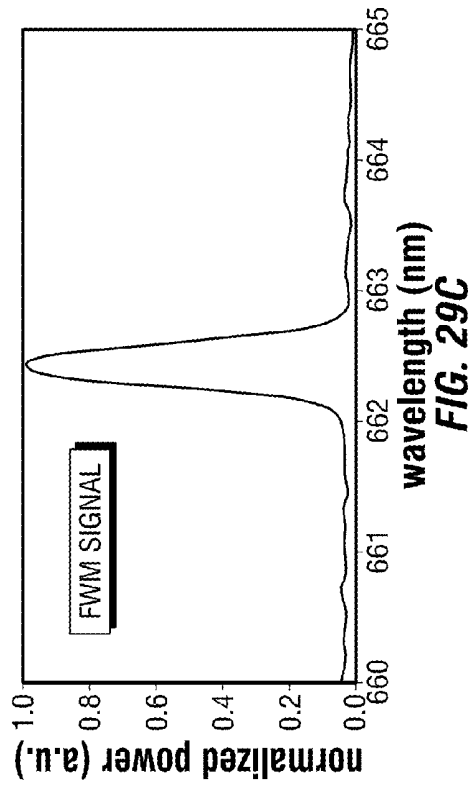
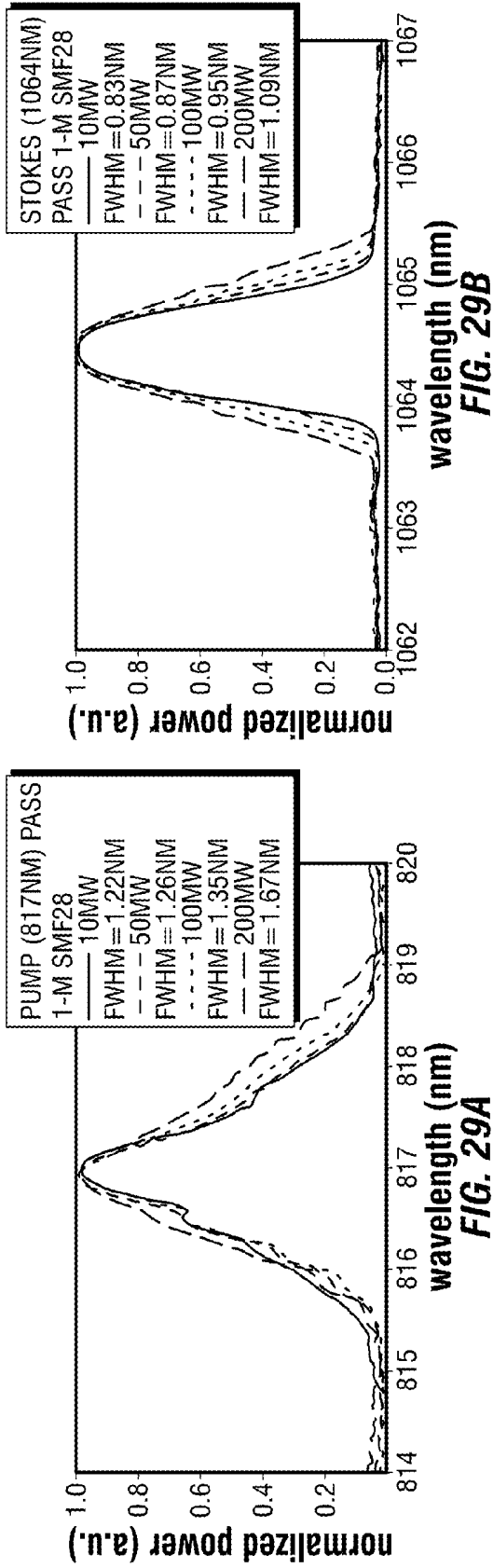
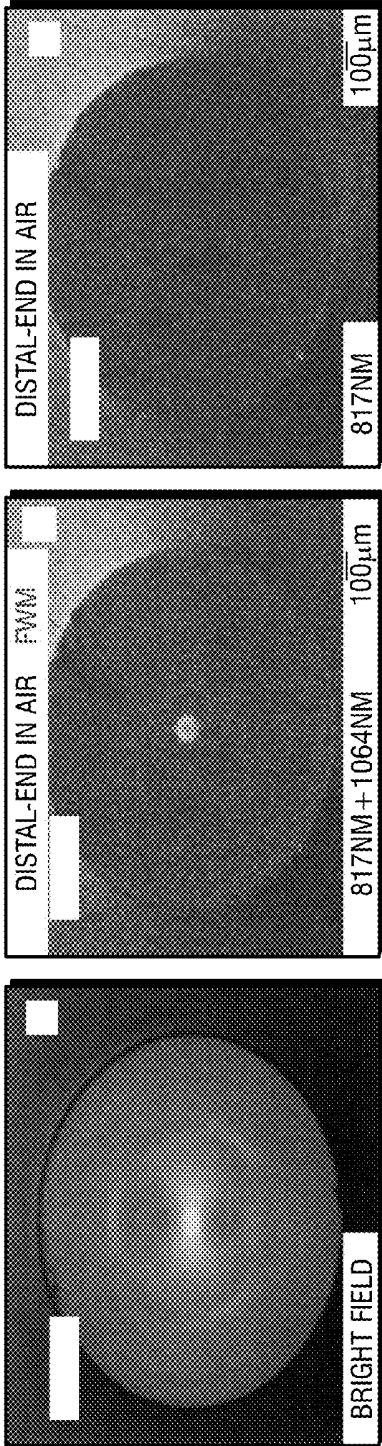


FIG. 28B





**FIG. 30A**

**FIG. 30B**

**FIG. 30C**

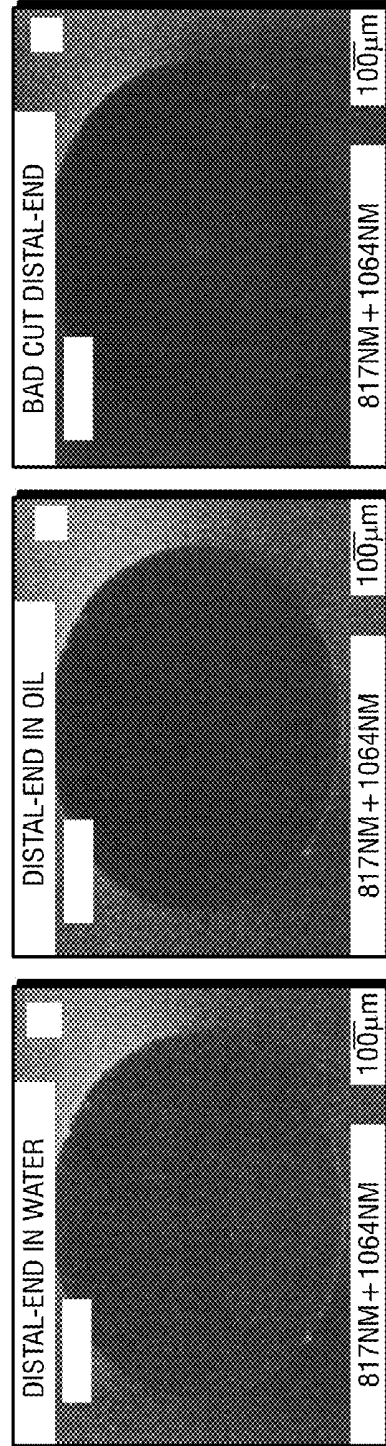


**FIG. 30D**

**FIG. 30E**

**FIG. 30F**

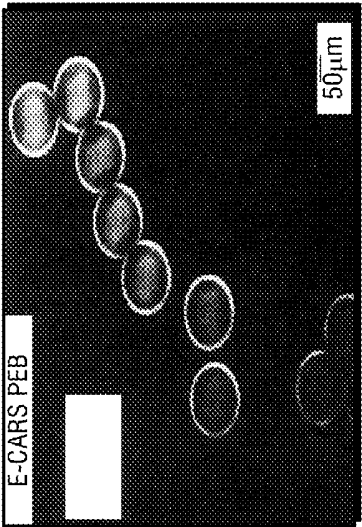


FIG. 31B

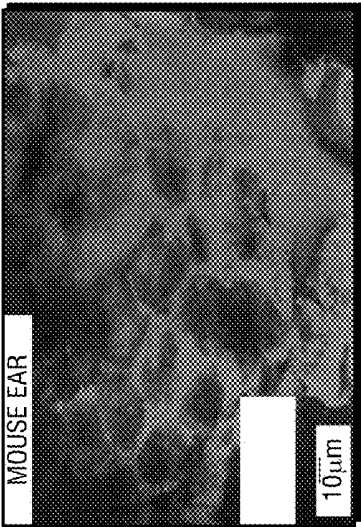


FIG. 31D

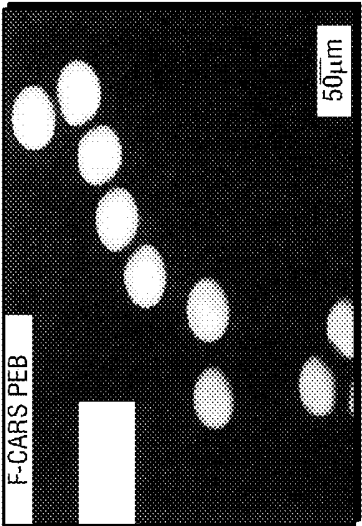


FIG. 31A

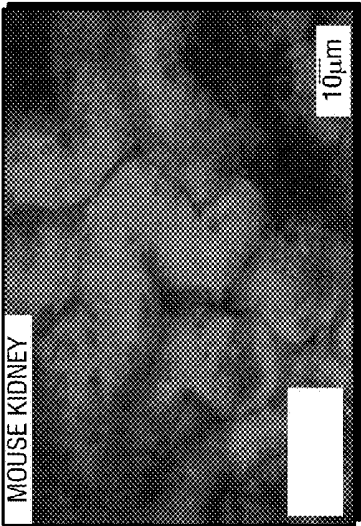


FIG. 31C

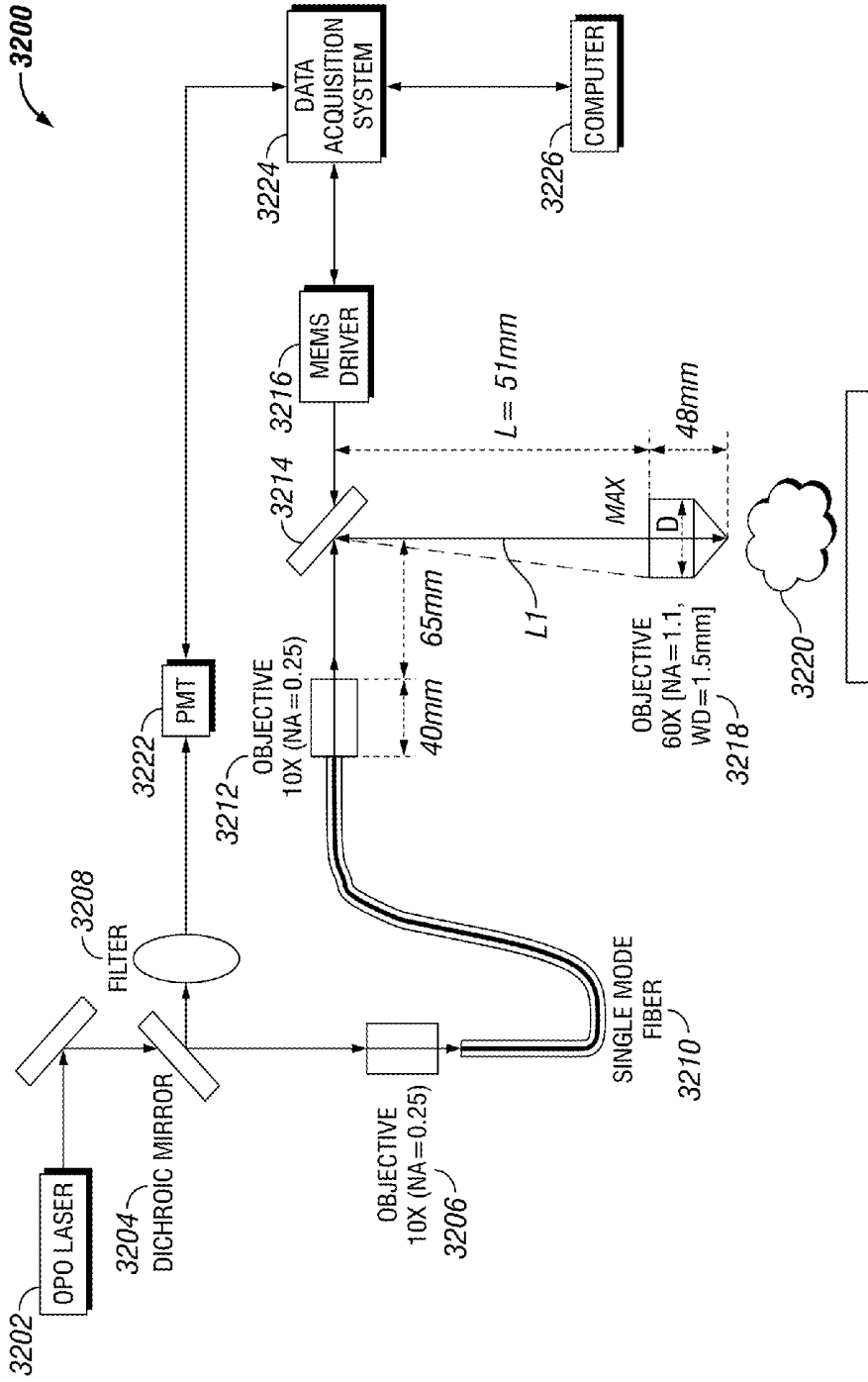
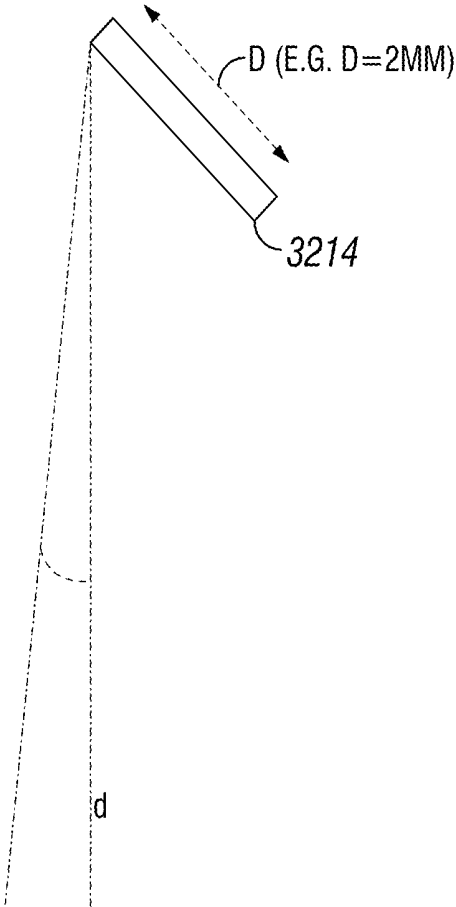


FIG. 32



**FIG. 33**

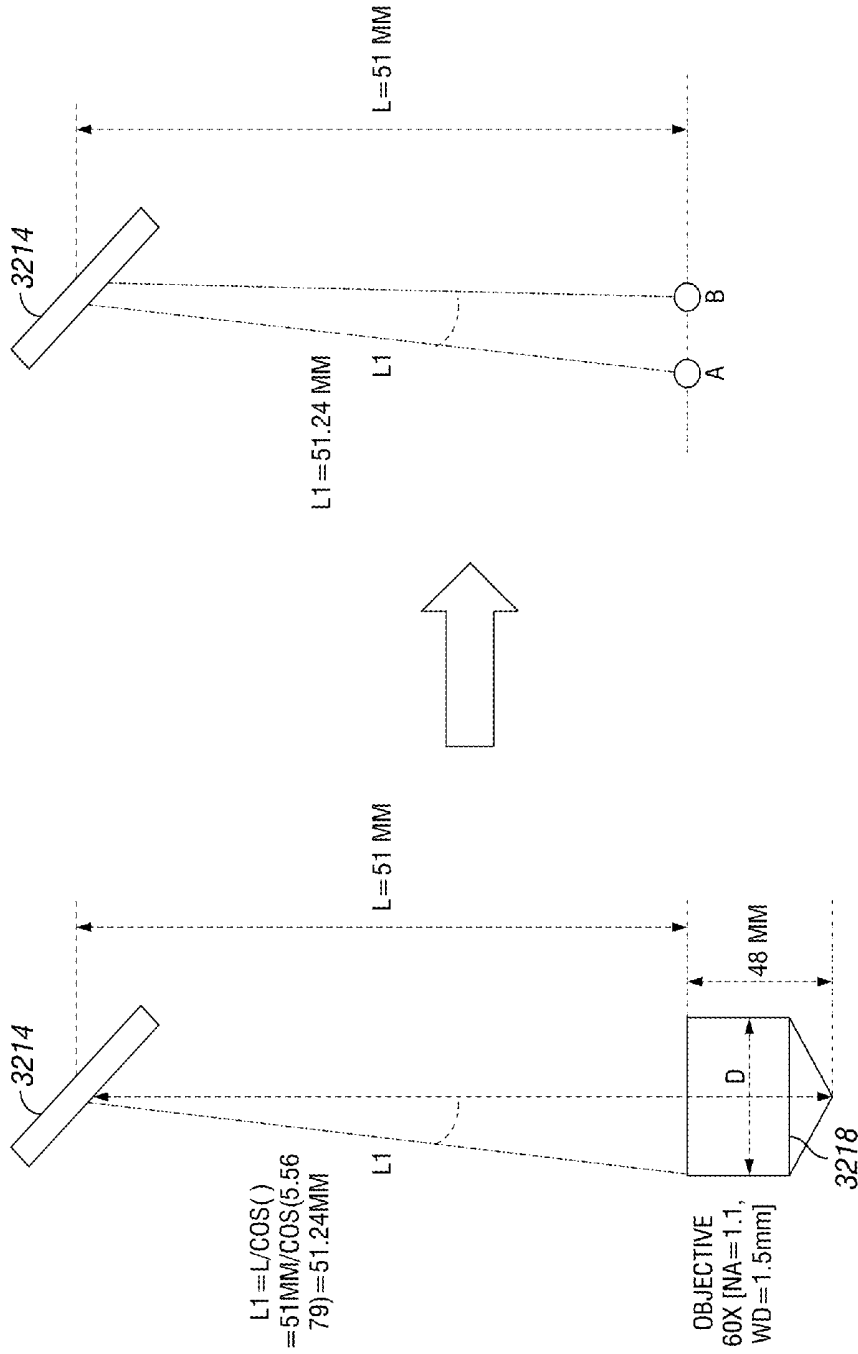


FIG. 34

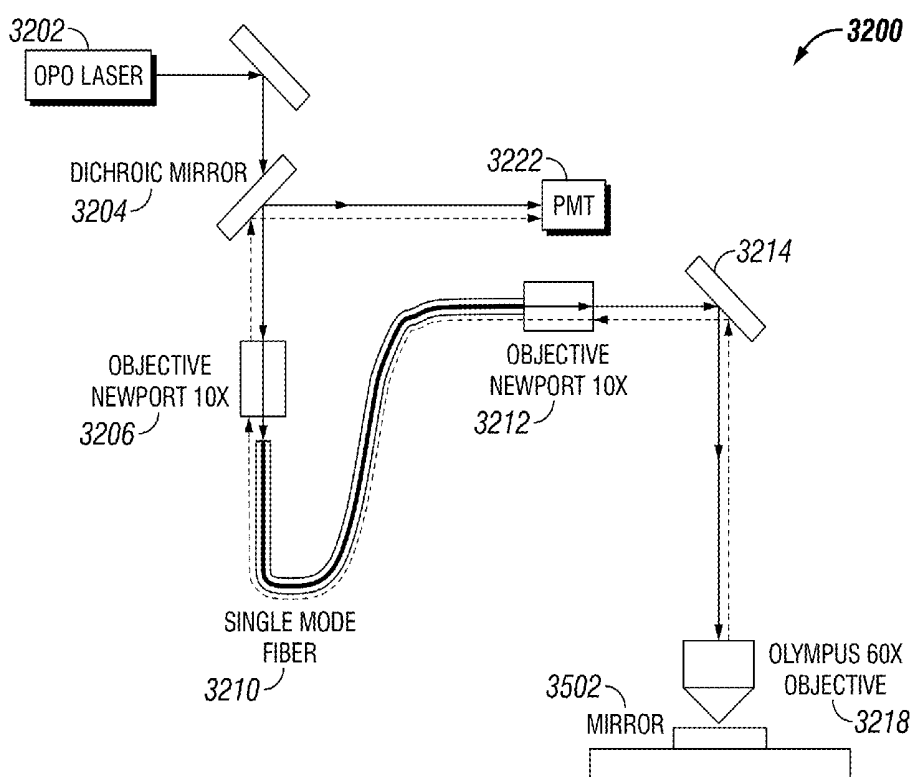
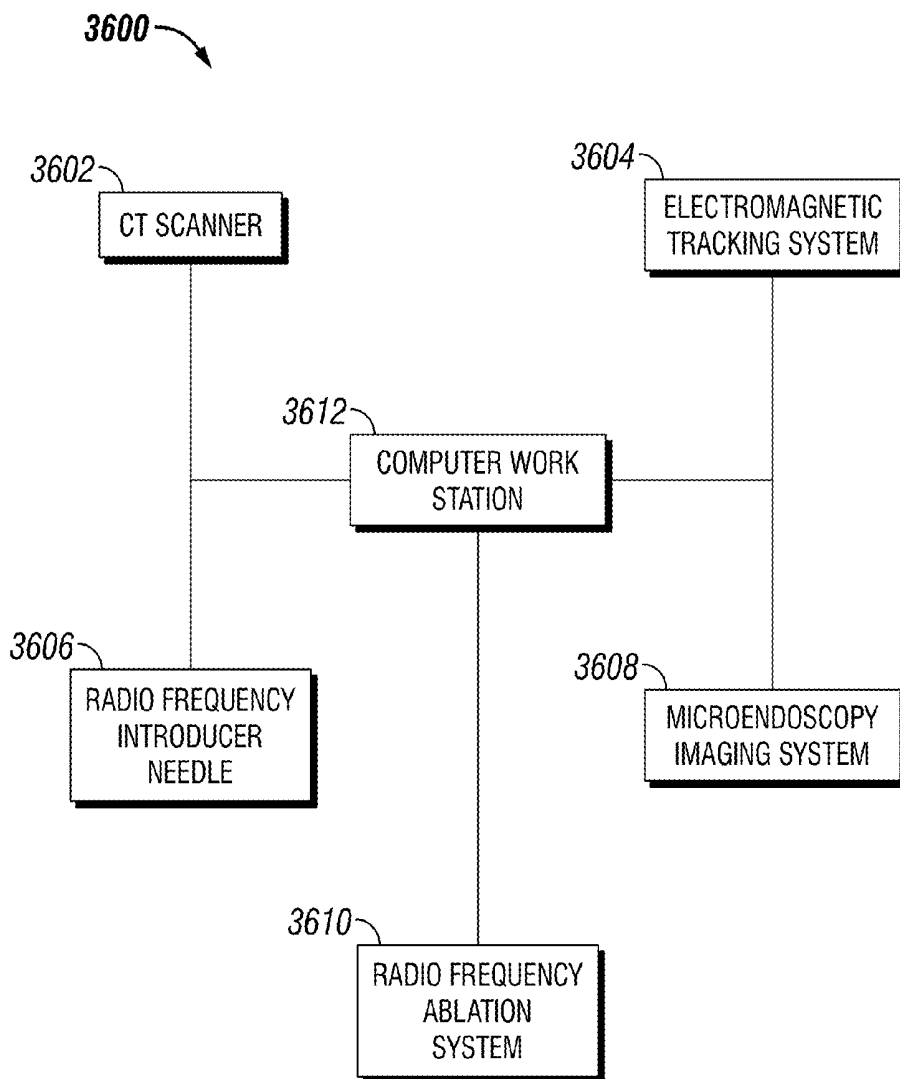


FIG. 35



**FIG. 36**

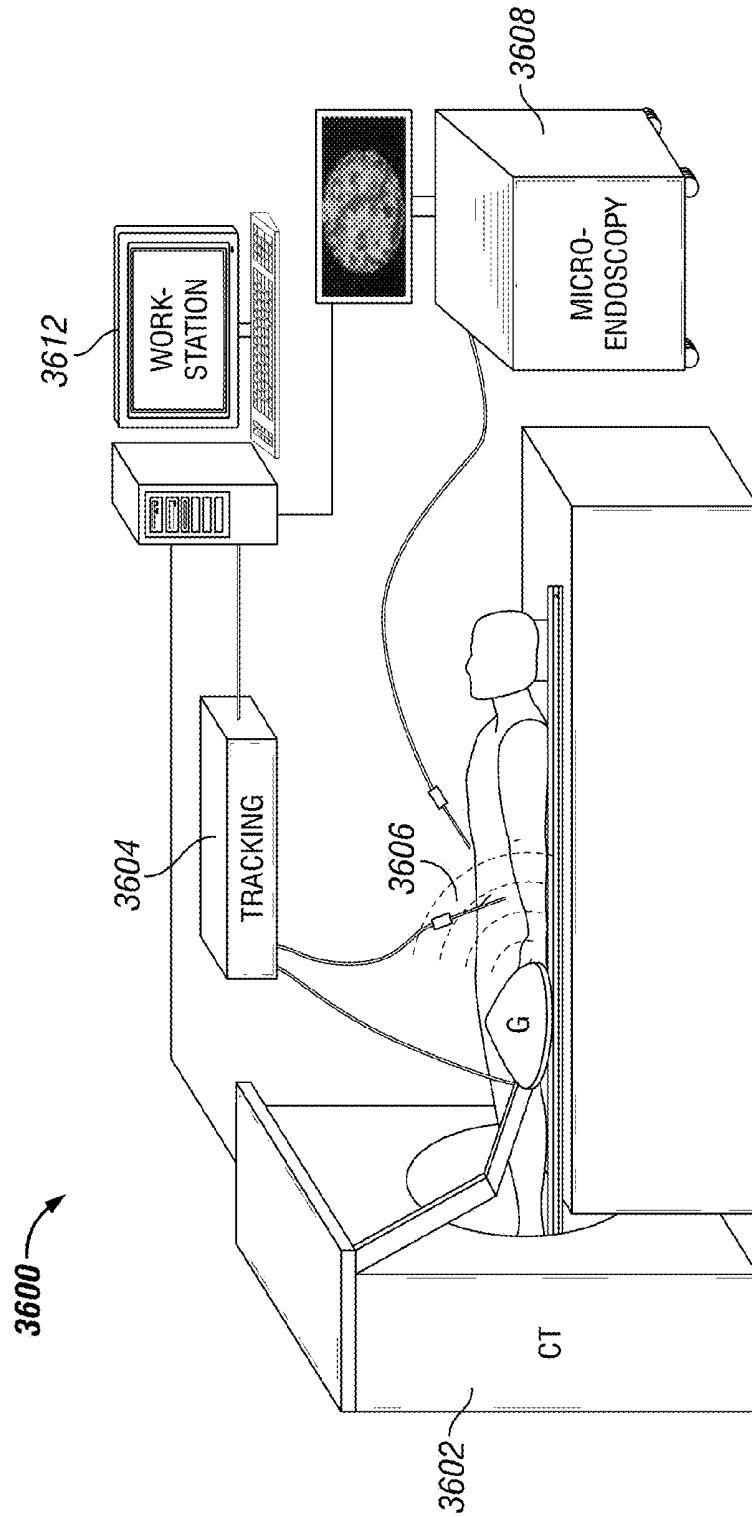


FIG. 37

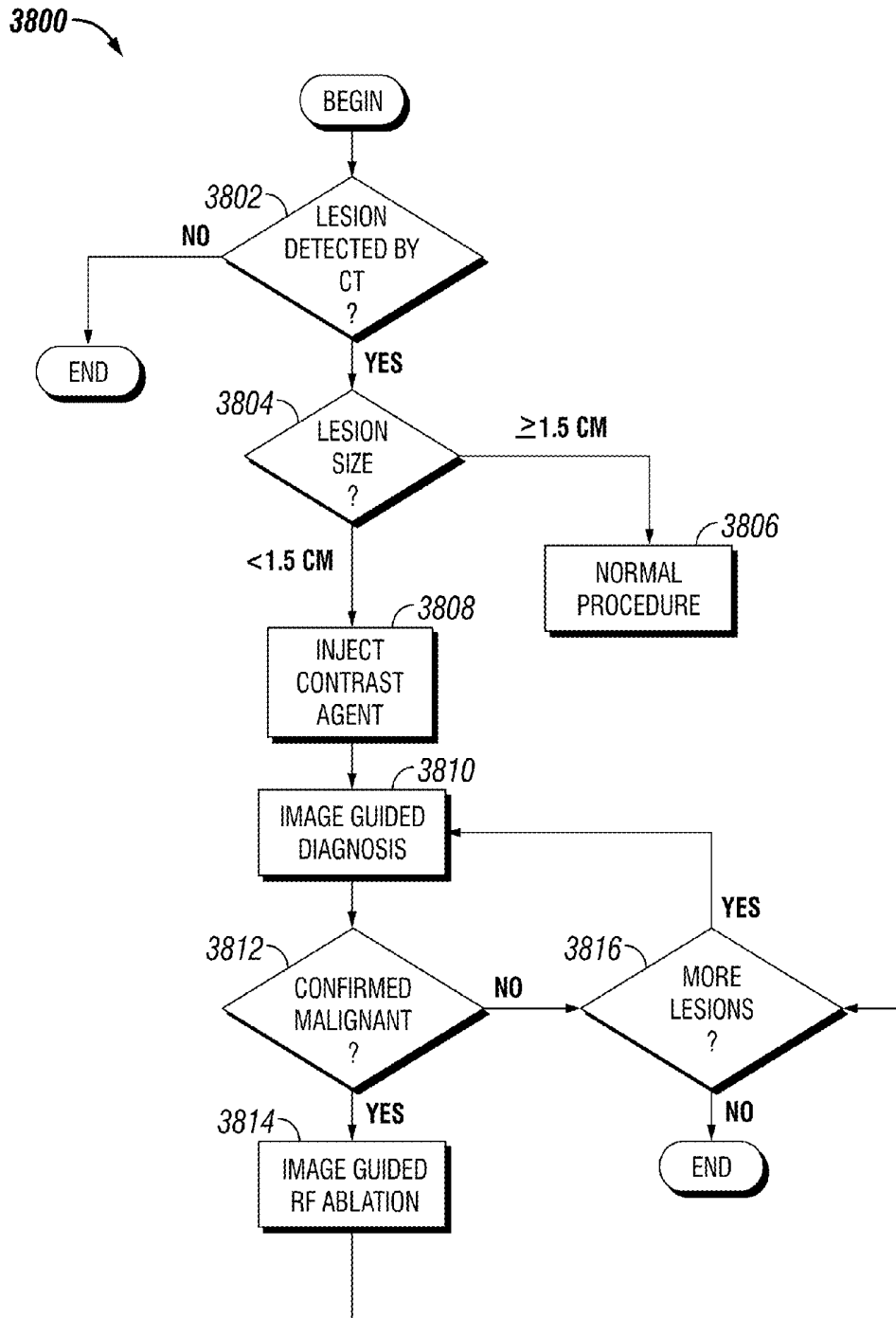
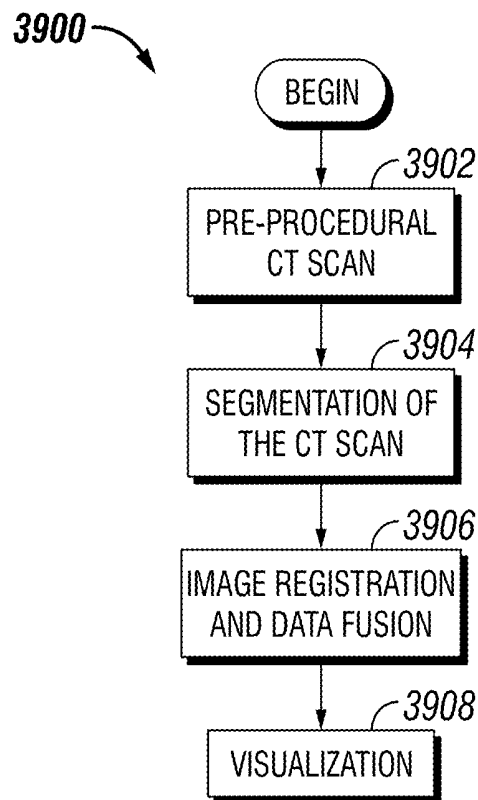


FIG. 38



**FIG. 39**

3902a

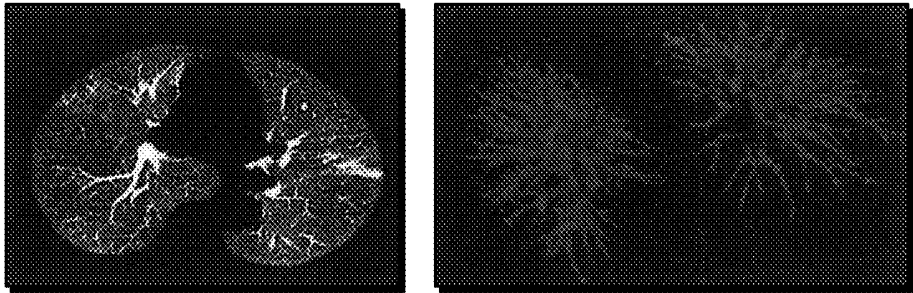


FIG. 39A

3906a

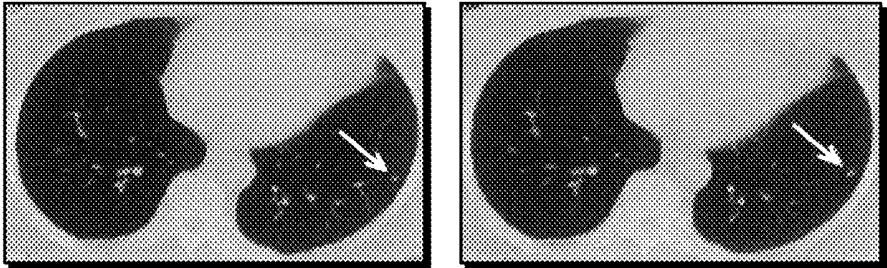


FIG. 39B

3908a

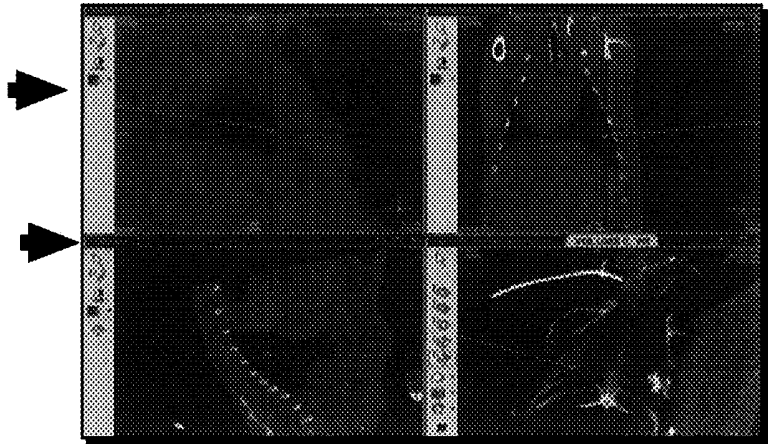


FIG. 39C

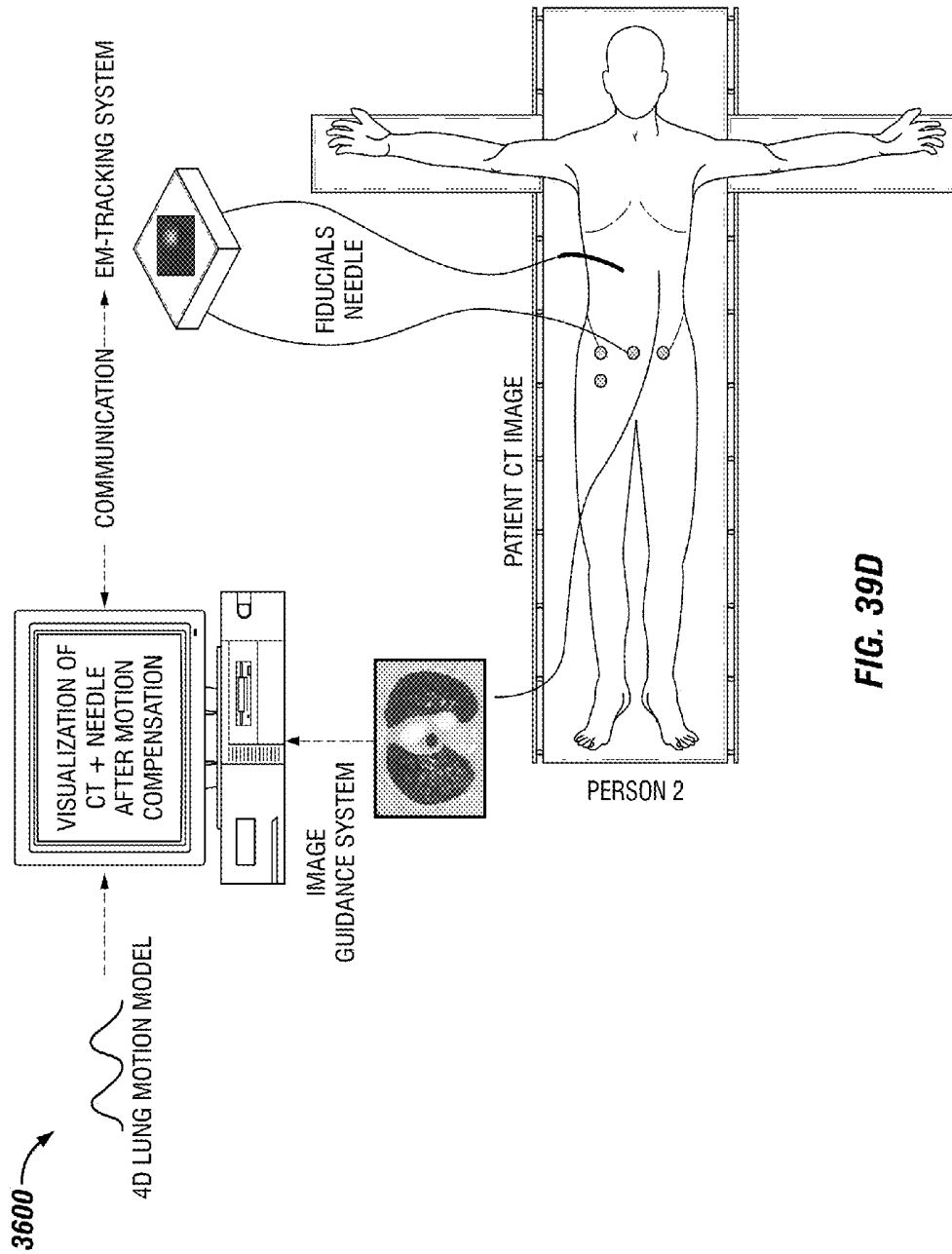


FIG. 39D

4000

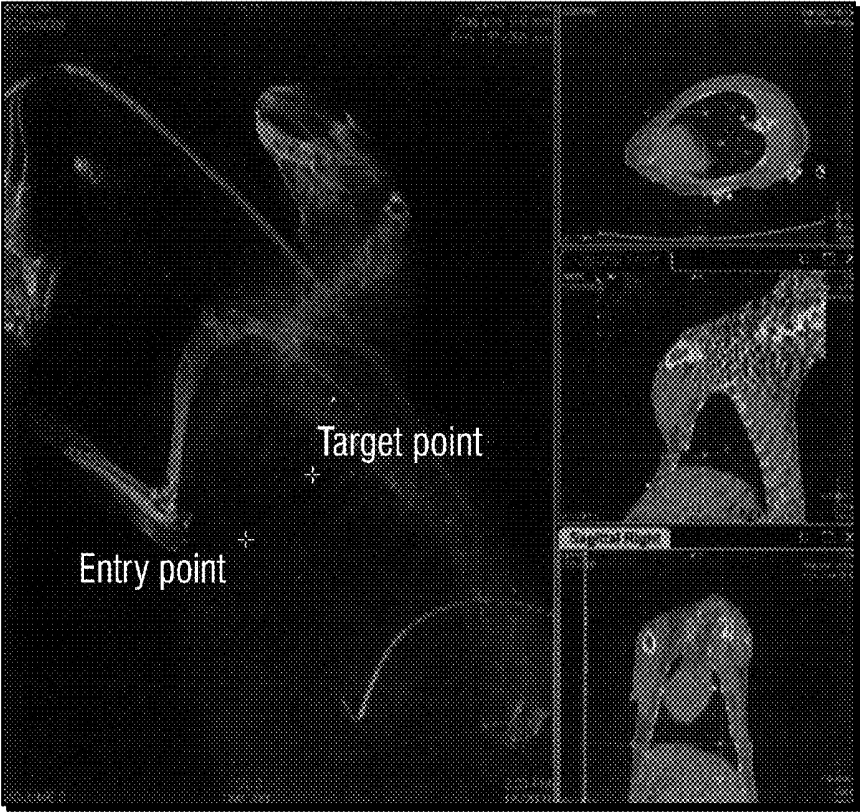


FIG. 40

4100

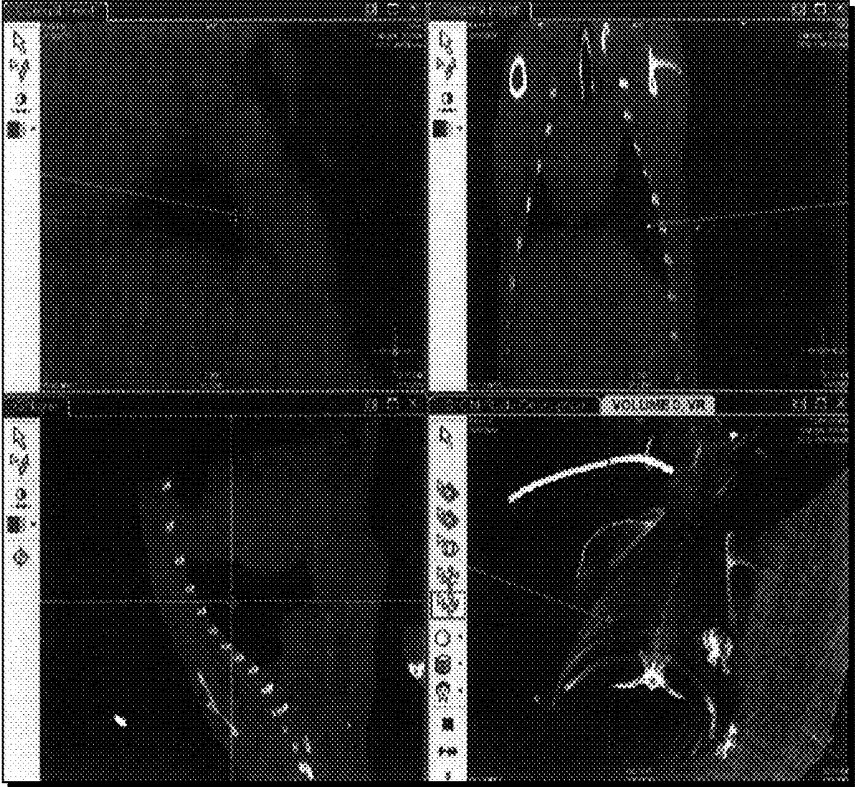


FIG. 41

4200a

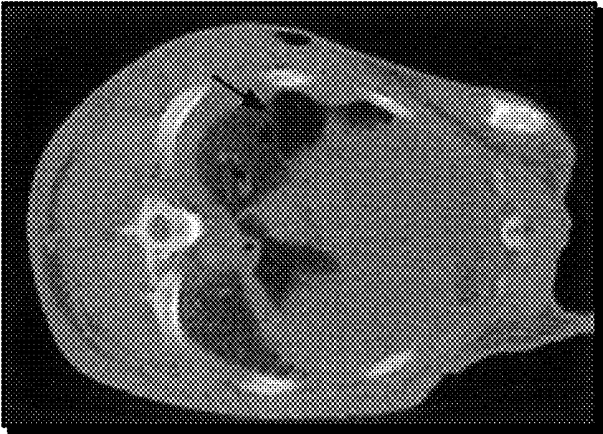


FIG. 42A

4200b

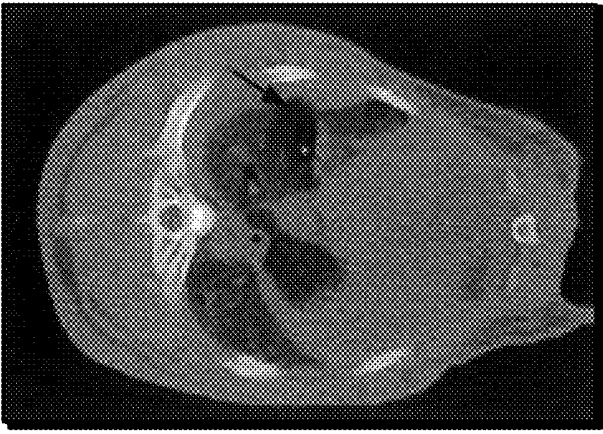


FIG. 42B

4200c

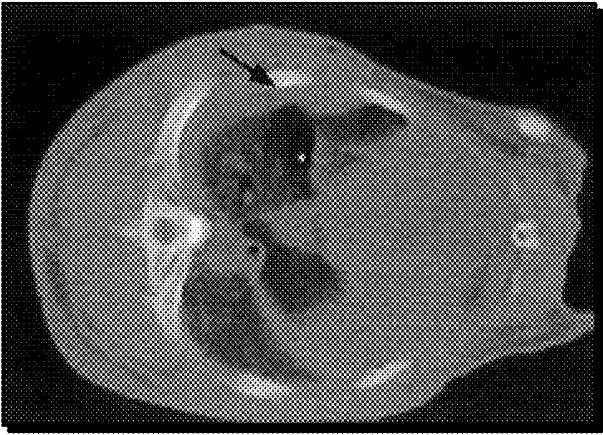


FIG. 42C

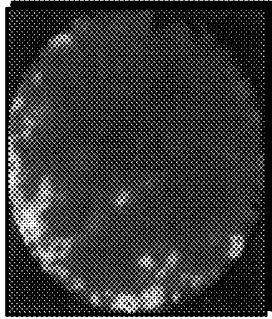


FIG. 43D

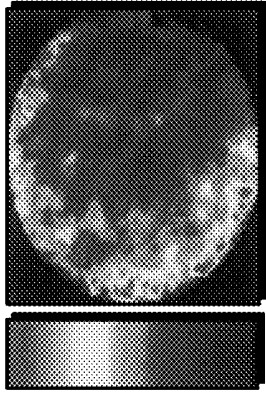


FIG. 43C

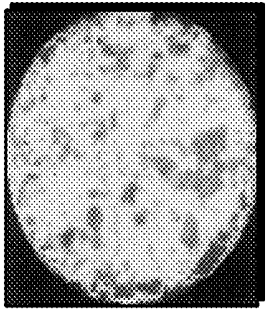


FIG. 43B

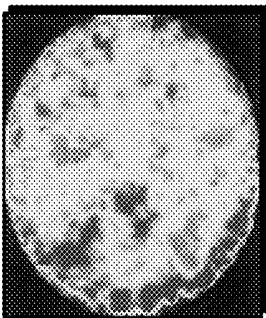


FIG. 43A

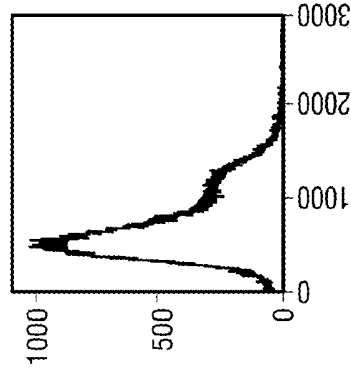


FIG. 44D

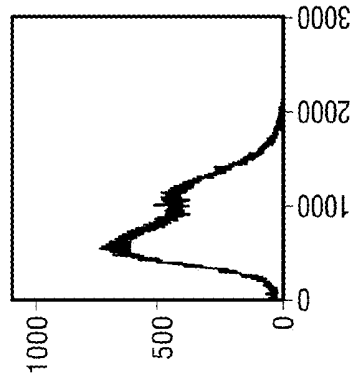


FIG. 44C

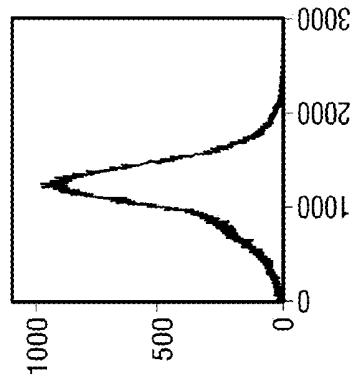


FIG. 44B

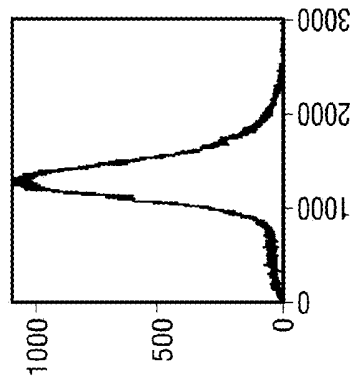
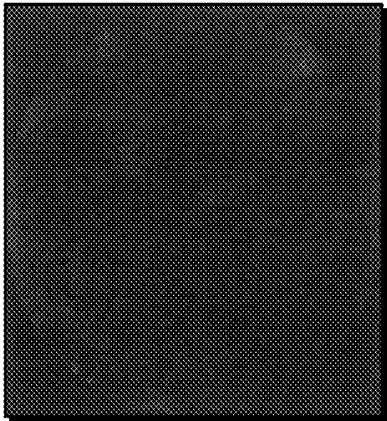
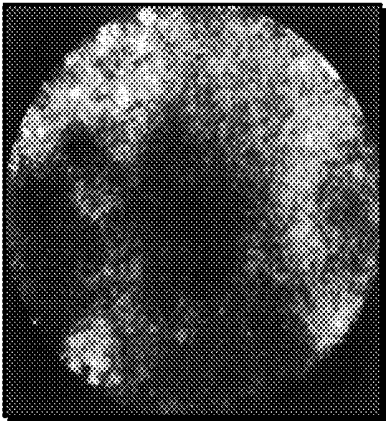


FIG. 44A



*FIG. 45A*



*FIG. 45C*

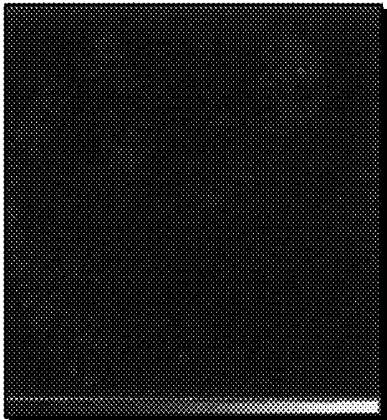


*FIG. 45B*

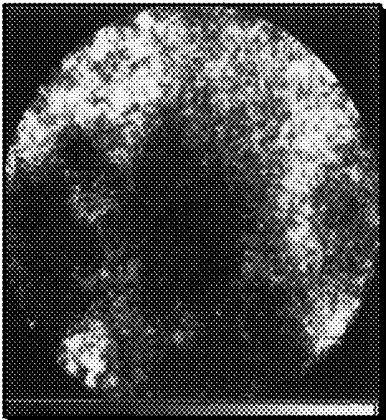


*FIG. 45D*

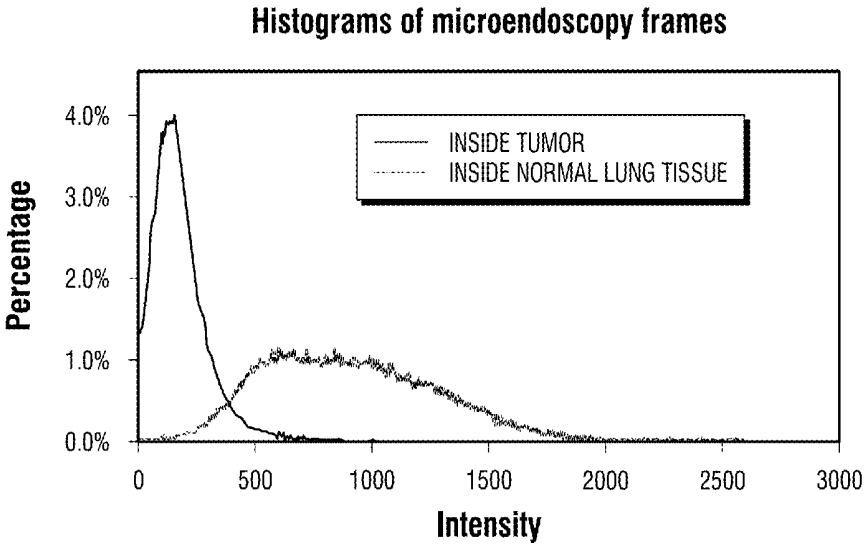


**FIG. 46**

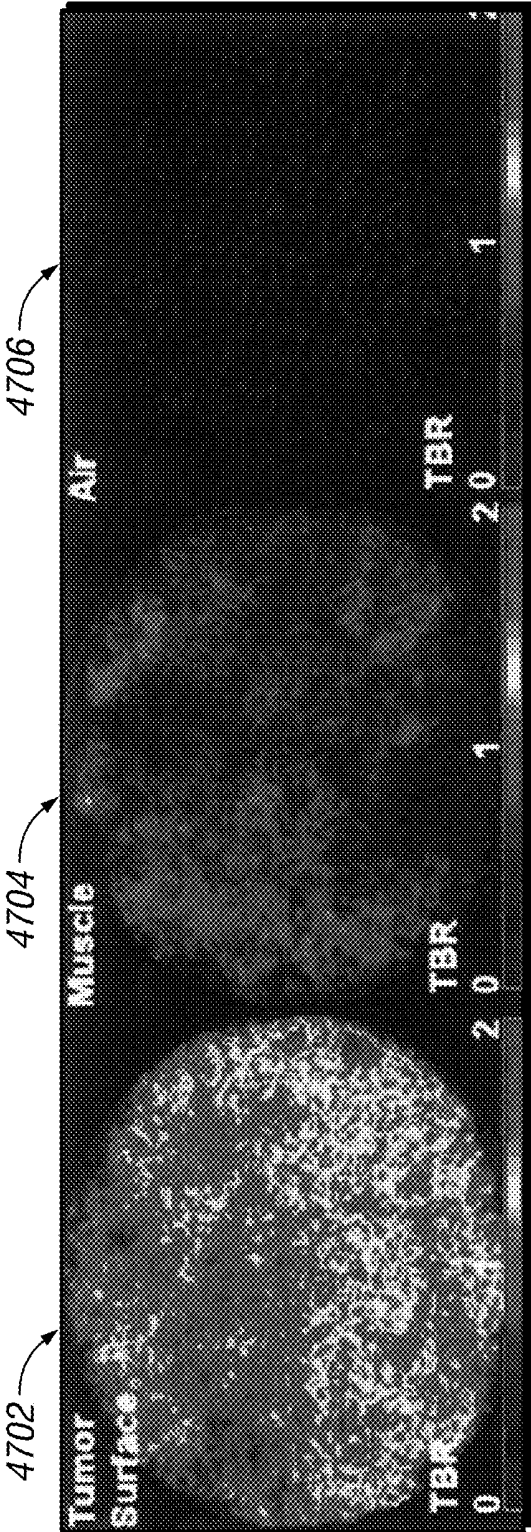


FIG. 47

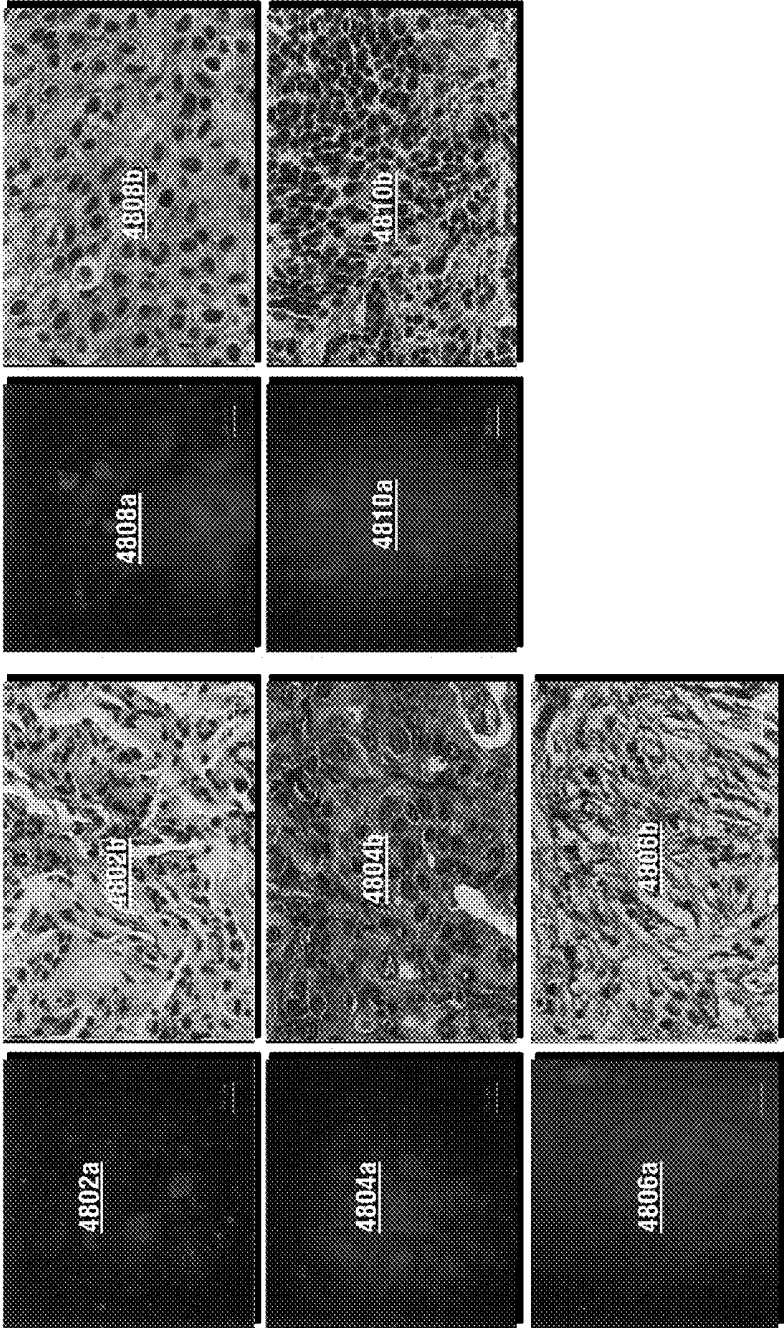
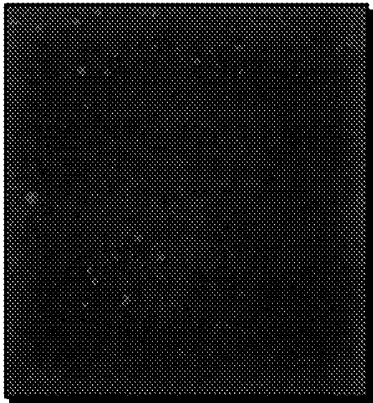


FIG. 48

4902



**FIG. 49A**

4906

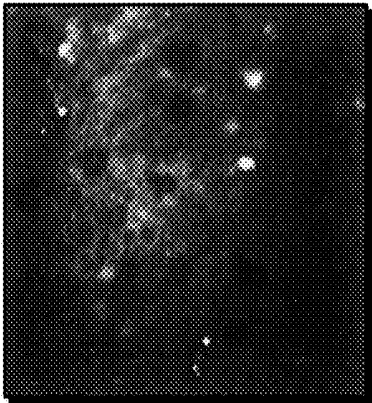


**FIG. 49C**

4904

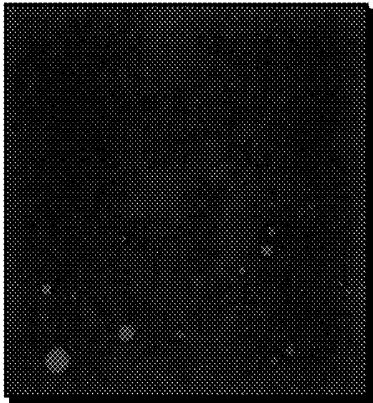


**FIG. 49B**

4908

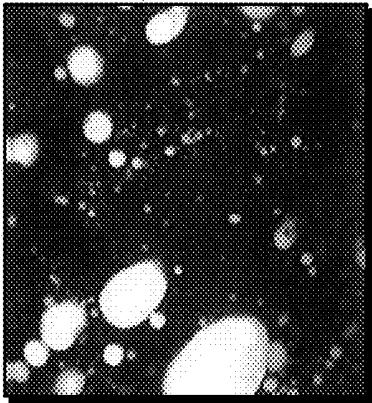


**FIG. 49D**

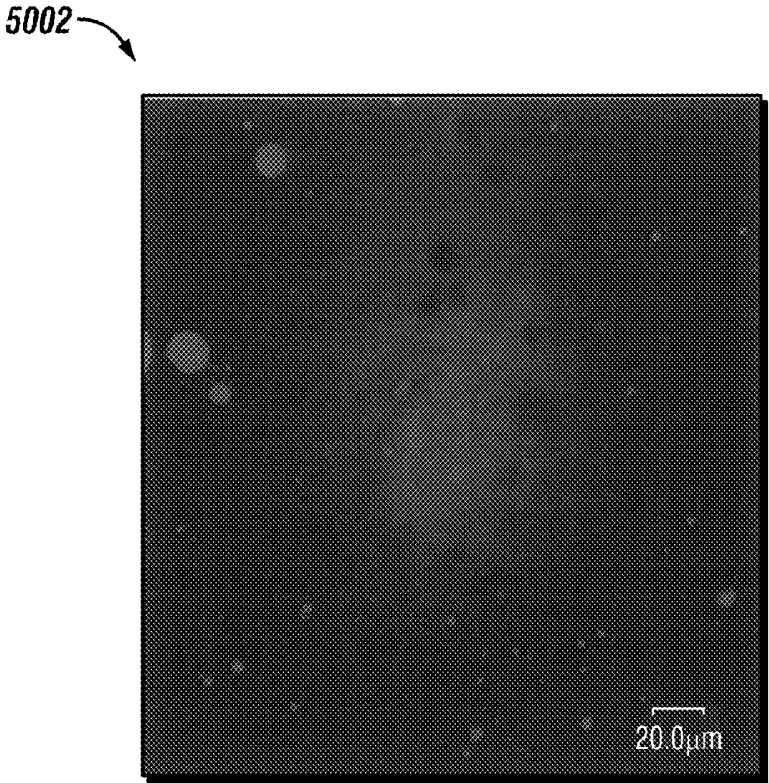


**FIG. 50A**

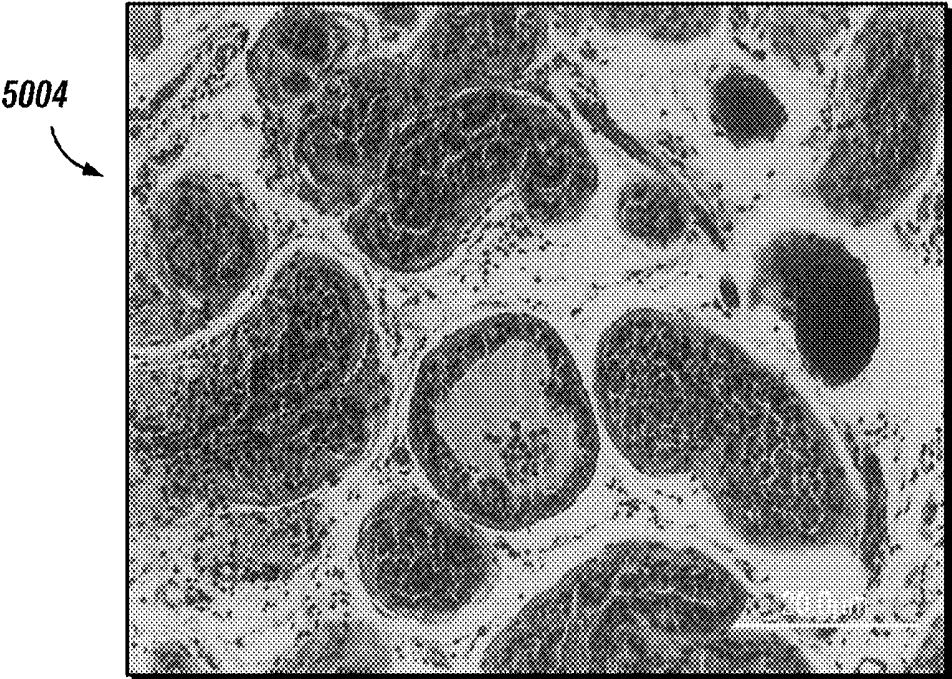


**FIG. 50B**

5006

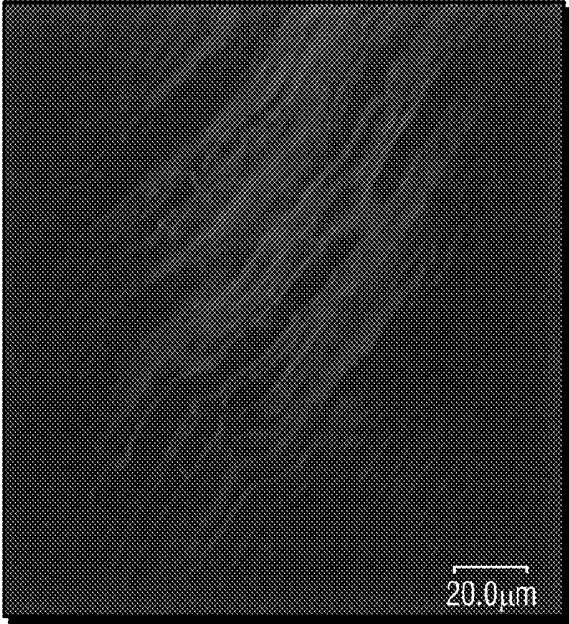


**FIG. 50C**

5008

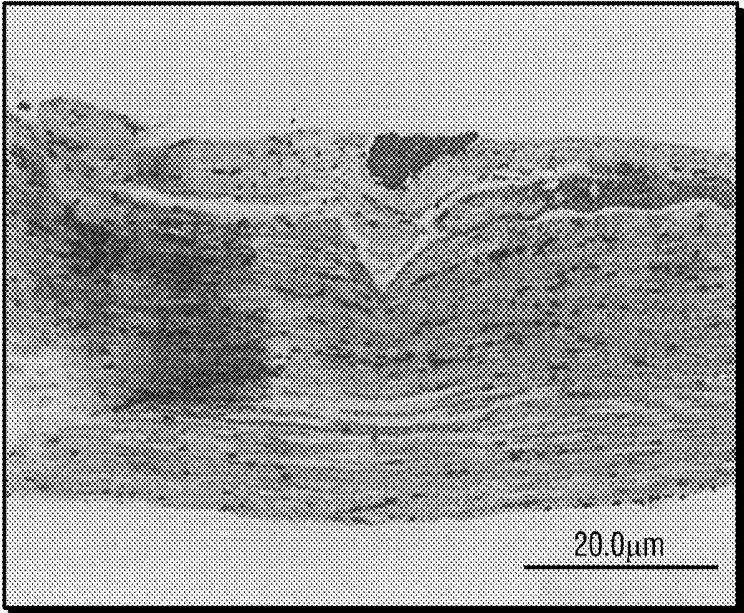


**FIG. 50D**

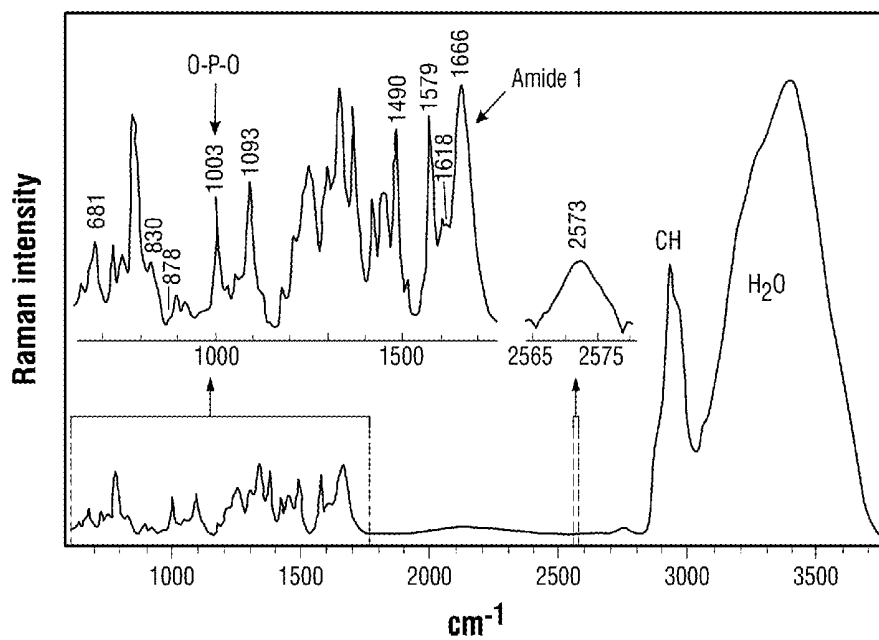


FIG. 51

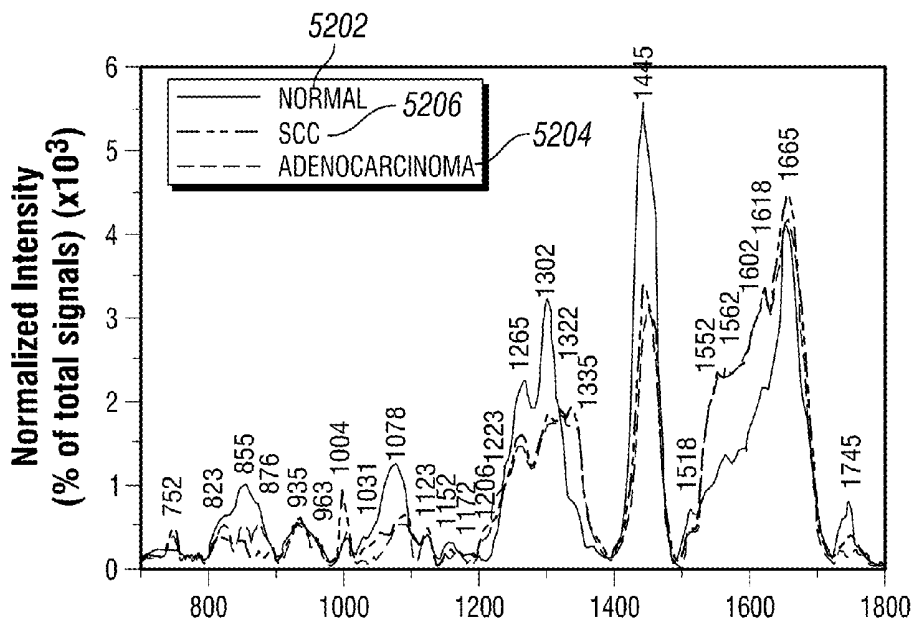


FIG. 52A

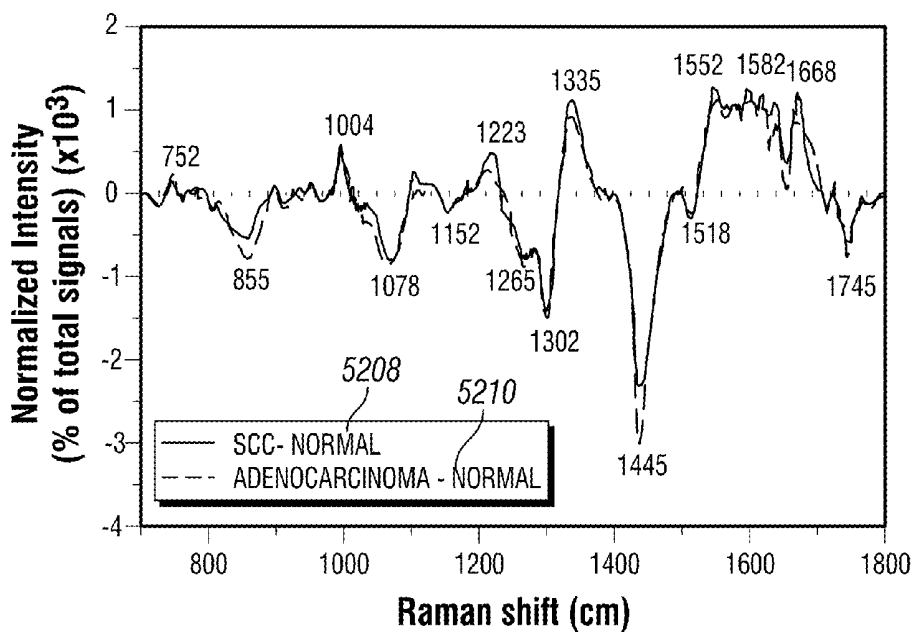
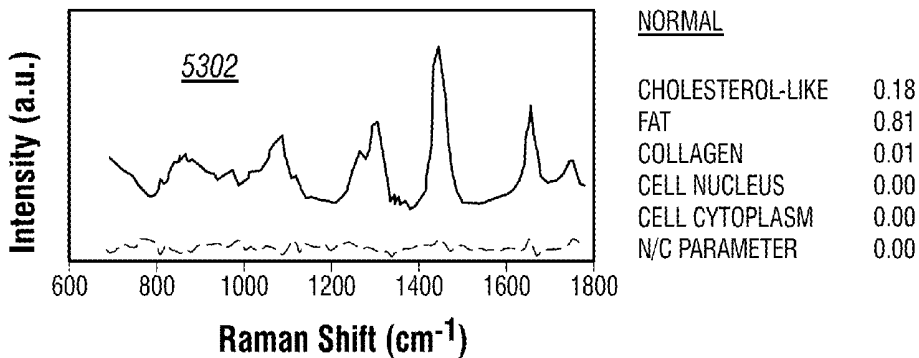
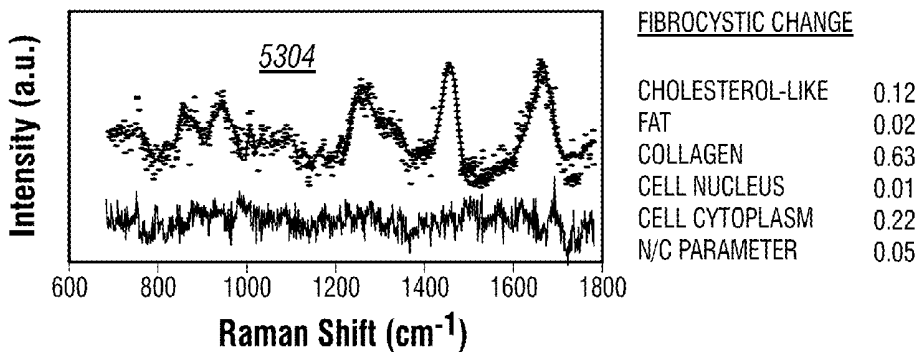


FIG. 52B



**FIG. 53A**



**FIG. 53B**

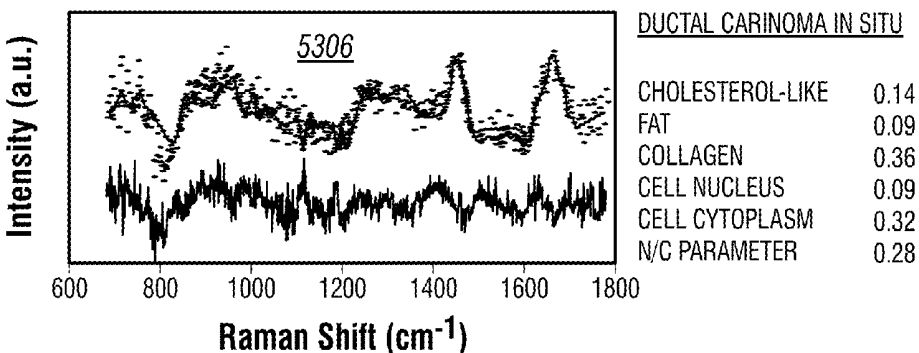


**FIG. 53C**

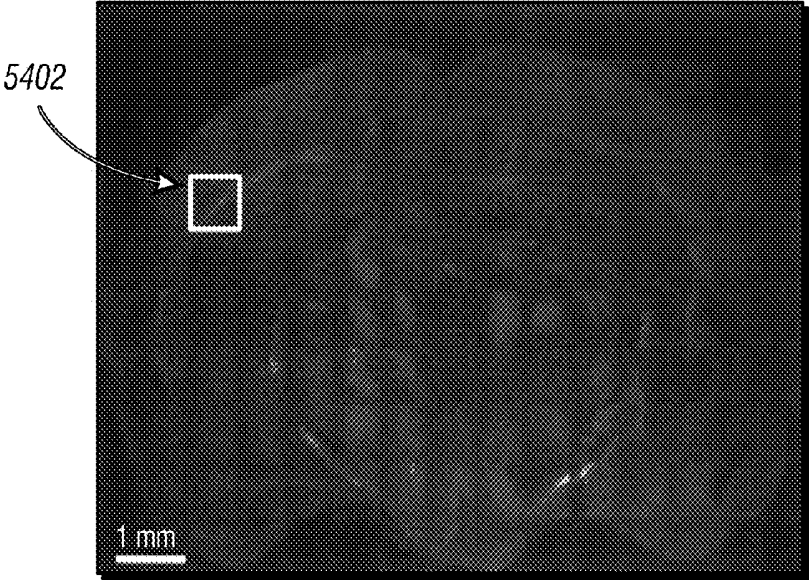


**FIG. 54**

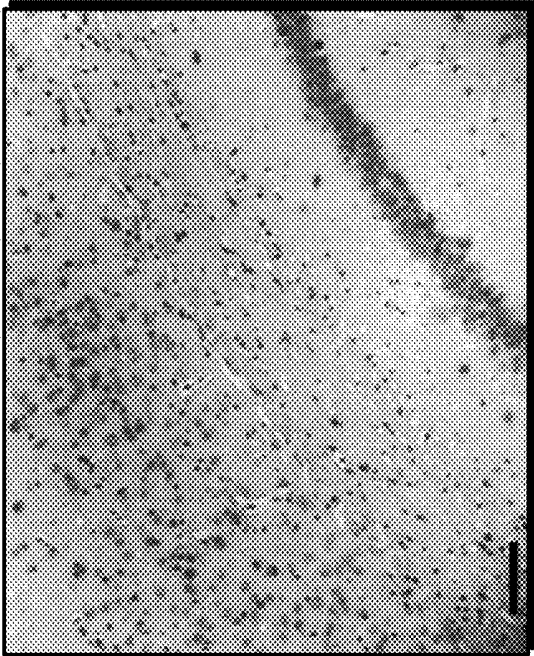


**FIG. 55B**

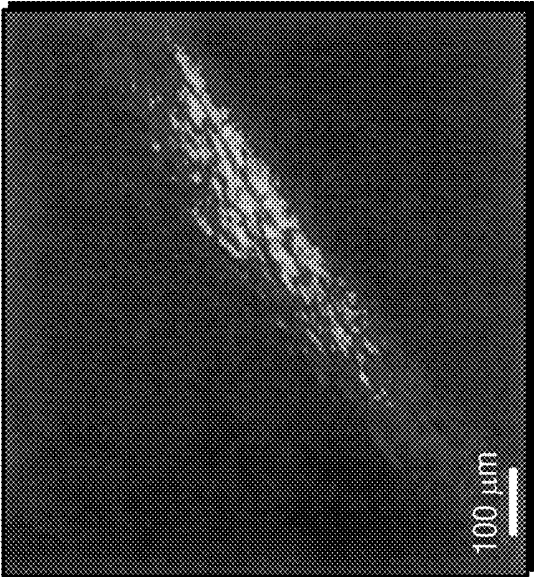


**FIG. 55A**

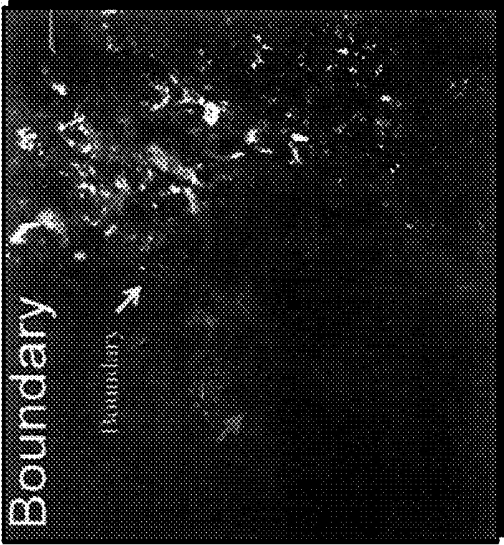


**FIG. 56C**

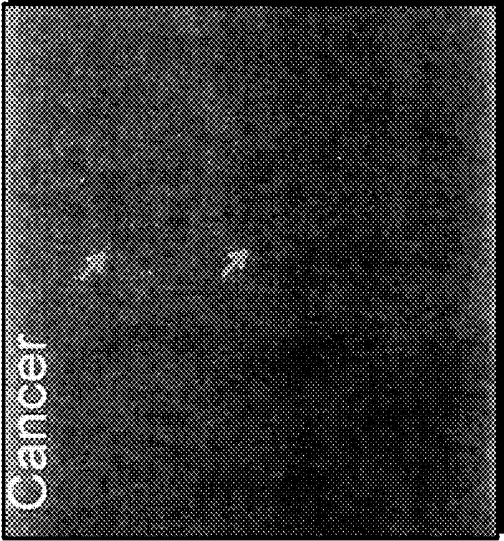


**FIG. 56B**

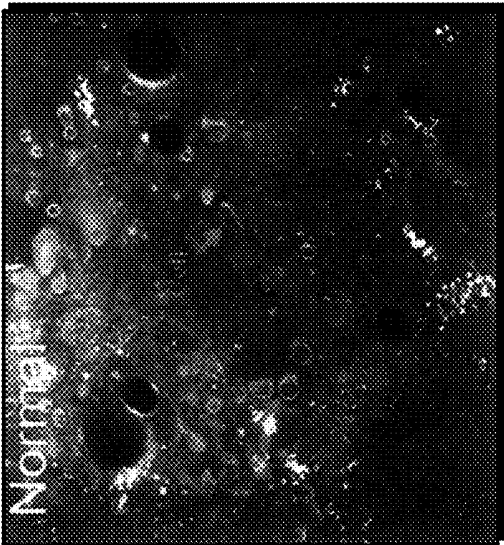


**FIG. 56A**

**DIAGNOSTIC AND TREATMENT METHODS  
USING COHERENT ANTI-STOKES RAMAN  
SCATTERING (CARS)-BASED  
MICROENDOSCOPIC SYSTEM**

1. CROSS-REFERENCE TO RELATED  
APPLICATIONS

**[0001]** This application is a continuation-in-part of U.S. Utility patent application Ser. No. 12/931,142 (Atty. Dkt. No. 37182.120), filed Jan. 25, 2011, and a continuation-in-part of PCT Intl. Patent Application No. PCT/US2011/043792, filed Jul. 12, 2011 (Atty. Dkt. No. 37182.121), each of which claims priority to U.S. Provisional Patent Application Nos. 61/399,182 and 61/399,139, each filed Jul. 8, 2010 and now expired (Atty. Dkt. Nos. 37182.119 and 371892.118, respectively); all of which are specifically incorporated herein in their entirety by express reference thereto.

2. BACKGROUND OF THE INVENTION

**[0002]** This disclosure relates to microendoscopic systems used for diagnosis and treatment of patients.

3. BRIEF DESCRIPTION OF THE DRAWINGS

**[0003]** For promoting an understanding of the principles of the invention, reference will now be made to the embodiments, or examples, illustrated in the drawings and specific language will be used to describe the same. It will nevertheless be understood that no limitation of the scope of the invention is thereby intended. Any alterations and further modifications in the described embodiments, and any further applications of the principles of the invention as described herein are contemplated as would normally occur to one of ordinary skill in the art to which the invention relates.

**[0004]** The following drawings form part of the present specification and are included to demonstrate certain aspects of the present invention. The invention may be better understood by reference to the following description taken in conjunction with the accompanying drawings, in which like reference numerals identify like elements, and in which:

**[0005]** FIG. 1 is an illustration of an exemplary embodiment of a micro-endoscopic system;

**[0006]** FIG. 2 is an illustration of an exemplary embodiment of a micro-endoscopic system;

**[0007]** FIG. 3 is an illustration of an exemplary embodiment of a micro-endoscopic system; FIG. 3A is a schematic illustration of an exemplary embodiment of a wave division multiplexer assembly; FIG. 3B is a schematic illustration of an exemplary embodiment of a wave division multiplexer assembly; FIG. 3C is a schematic illustration of an exemplary embodiment of a fiber probe system;

**[0008]** FIG. 4 is a schematic illustration of an exemplary embodiment of a microendoscopic system;

**[0009]** FIG. 5 is a flowchart of an exemplary embodiment of a method for operating a micro-endoscopic system;

**[0010]** FIG. 6 is a flowchart of an exemplary embodiment of a method for calculating a global registration;

**[0011]** FIG. 7, FIG. 7A, FIG. 7B, FIG. 7C, FIG. 7D, and FIG. 7E include a photograph of a reference image (FIG. 7), and simulated images (FIG. 7A, FIG. 7B, FIG. 7C, FIG. 7D, and FIG. 7E) that are derived from the reference image in FIG. 7;

**[0012]** FIG. 8A, FIG. 8B, FIG. 8C, FIG. 8D, and FIG. 8E are motion-corrected images resulting from the application of

an exemplary experimental embodiment of the method of FIG. 6 to the simulated images of FIG. 7A, FIG. 7B, FIG. 7C, FIG. 7D, and FIG. 7E;

**[0013]** FIG. 9A, FIG. 9B, FIG. 9C, FIG. 9D, and FIG. 9E show the differences between the reference image of FIG. 7A and the motion-corrected images of FIG. 8A, FIG. 8B, FIG. 8C, FIG. 8D, and FIG. 8E;

**[0014]** FIG. 10 is a graphical illustration of the error for the images generated in an exemplary experimental embodiment using the motion-correction method of FIG. 6 versus the error for images generated using a conventional NMI method of motion correction;

**[0015]** FIG. 11, FIG. 11A, FIG. 11B, FIG. 11C, and FIG. 11D include a photograph of a reference image (FIG. 11) in an exemplary experimental embodiment; FIG. 11A, FIG. 11B, FIG. 11C, and FIG. 11D are photographs of exemplary experimental embodiments;

**[0016]** FIG. 12A, FIG. 12B, FIG. 12C, and FIG. 12D are photographs of exemplary experimental embodiments;

**[0017]** FIG. 13 is a flowchart of an exemplary embodiment of a method for calculating a global registration;

**[0018]** FIG. 14 is a flowchart of an exemplary embodiment of a method for calculating a global registration;

**[0019]** FIG. 15A and FIG. 15B are photographs of exemplary experimental embodiments;

**[0020]** FIG. 16, FIG. 16A, FIG. 16B, FIG. 16C, and FIG. 16D include a photograph of a reference image (FIG. 16) in an exemplary experimental embodiment; FIG. 16A, FIG. 16B, FIG. 16C, and FIG. 16D are photographs of exemplary experimental embodiments;

**[0021]** FIG. 17A, FIG. 17B, FIG. 17C and FIG. 17D are graphical illustrations of exemplary experimental embodiments;

**[0022]** FIG. 18 is a graphical illustration of exemplary experimental embodiments;

**[0023]** FIG. 19A and FIG. 19B are flowcharts of an exemplary embodiment of a method for motion correction;

**[0024]** FIG. 20 is an illustration of exemplary experimental embodiments;

**[0025]** FIG. 21 is an illustration of exemplary experimental embodiments;

**[0026]** FIG. 22 is a schematic illustration of an exemplary embodiment of a method for motion correction;

**[0027]** FIG. 23A, FIG. 23B, and FIG. 23C are illustrations of exemplary experimental embodiments;

**[0028]** FIG. 24A, FIG. 24B, and FIG. 24C are illustrations of exemplary experimental embodiments;

**[0029]** FIG. 25A, FIG. 25B, and FIG. 25C are graphical illustrations of exemplary experimental embodiments;

**[0030]** FIG. 26A and FIG. 26B are schematic illustrations of an exemplary embodiment of a CARS microscopy system;

**[0031]** FIG. 27A, FIG. 27B and FIG. 27C are graphical illustrations of an exemplary experimental embodiment of the system of FIG. 26A and FIG. 26B;

**[0032]** FIG. 28A and FIG. 28B are graphical illustrations of an exemplary experimental embodiment of the system of FIG. 26A and FIG. 26B;

**[0033]** FIG. 29A, FIG. 29B, and FIG. 29C illustrate normalized measured pump (817 nm) and Stokes (1064 nm) wave spectra as a function of propagating power in an SMF28 communication fiber;

**[0034]** FIG. 30A, FIG. 30B, FIG. 30C, FIG. 30D, FIG. 30E and FIG. 30F are images of exemplary experimental embodiments of the system of FIG. 26A and FIG. 26B;

[0035] FIG. 31A, FIG. 31B, FIG. 31C, and FIG. 31D are images of exemplary experimental embodiments of the system of FIG. 26A and FIG. 26B;

[0036] FIG. 32 is a schematic illustration of an exemplary embodiment of a CARS microscopy system;

[0037] FIG. 33 is a schematic illustration of an exemplary embodiment of a scanning mirror for the CARS microscopy system of FIG. 32;

[0038] FIG. 34 is a schematic illustration of an exemplary embodiment of a scanning mirror for the CARS microscopy system of FIG. 32;

[0039] FIG. 35 is a schematic illustration of an exemplary experimental embodiment of a CARS microscopy system;

[0040] FIG. 36 is a schematic illustration of an exemplary embodiment of a MIMIG molecular imaging system for treatment and diagnosis of patients;

[0041] FIG. 37 is a schematic illustration of an exemplary embodiment of a MIMIG molecular imaging system for treatment and diagnosis of patients;

[0042] FIG. 38 is a flowchart of an exemplary embodiment of a method of operating the systems of FIG. 36 and FIG. 37;

[0043] FIG. 39 is a flowchart illustration of an exemplary method of operating the systems of FIG. 36 and FIG. 37; FIG. 39A, FIG. 39B and FIG. 39C are illustrations of exemplary user interfaces provided by the method of FIG. 39; FIG. 39D is a schematic illustration of an exemplary embodiment of a respiratory motion correction method;

[0044] FIG. 40 is an illustration of an exemplary embodiment of a user interface during exemplary experimental embodiments of the system and method of FIG. 26A, FIG. 26B, FIG. 27A, and FIG. 27B;

[0045] FIG. 41 is an illustration of an exemplary embodiment of a user interface during exemplary experimental embodiments of the system and method of FIG. 26A, FIG. 26B, FIG. 27A, and FIG. 27B;

[0046] FIG. 42A, FIG. 42B and FIG. 42C are illustrations of exemplary embodiments of user interfaces during exemplary experimental embodiments of the system and methods of FIG. 36, FIG. 37, FIG. 38 and FIG. 39;

[0047] FIG. 43A, FIG. 43B, FIG. 43C and FIG. 43D are illustrations of exemplary embodiments of user interfaces during exemplary experimental embodiments of the system and methods of FIG. 36, FIG. 37, FIG. 38 and FIG. 39;

[0048] FIG. 44A, FIG. 44B, FIG. 44C and FIG. 44D are illustrations of exemplary embodiments of user interfaces during, exemplary experimental embodiments of the system and methods of FIG. 36, FIG. 37, FIG. 38 and FIG. 39;

[0049] FIG. 45A, FIG. 45B, FIG. 45C and FIG. 45D are images of exemplary experimental embodiments of the system and methods of FIG. 36, FIG. 37, FIG. 38 and FIG. 39;

[0050] FIG. 46 is a graphical illustration of exemplary experimental embodiments of the system and methods of FIG. 36, FIG. 37, FIG. 38 and FIG. 39;

[0051] FIG. 47 shows images of exemplary experimental embodiments of the system and methods of FIG. 36, FIG. 37, FIG. 38 and FIG. 39;

[0052] FIG. 48 shows images of exemplary experimental embodiments of the system and methods of FIG. 36, FIG. 37, FIG. 38 and FIG. 39;

[0053] FIG. 49A, FIG. 49B, FIG. 49C and FIG. 49D are images of exemplary experimental embodiments of the system and methods of FIG. 36, FIG. 37, FIG. 38 and FIG. 39;

[0054] FIG. 50A, FIG. 50B, FIG. 50C and FIG. 50D are images of exemplary experimental embodiments of the system and methods of FIG. 36, FIG. 37, FIG. 38 and FIG. 39.

[0055] FIG. 51 is a graphical illustration of exemplary experimental embodiments of the system and methods of FIG. 36, FIG. 37, FIG. 38 and FIG. 39;

[0056] FIG. 52A and FIG. 52B are graphical illustrations of exemplary experimental embodiments of the system and methods of FIG. 36, FIG. 37, FIG. 38 and FIG. 39;

[0057] FIG. 53A, FIG. 53B and FIG. 53C are graphical illustrations of exemplary experimental embodiments of the system and methods of FIG. 36, FIG. 37, FIG. 38 and FIG. 39;

[0058] FIG. 54 is an illustration of exemplary experimental embodiments of the system and methods of FIG. 36, FIG. 37, FIG. 38 and FIG. 39;

[0059] FIG. 55A and FIG. 55B are illustrations of exemplary experimental embodiments of the system and methods of FIG. 36, FIG. 37, FIG. 38 and FIG. 39; and

[0060] FIG. 56A, FIG. 56B and FIG. 56C are illustrations of exemplary experimental embodiments of the system and methods of FIG. 36, FIG. 37, FIG. 38 and FIG. 39.

#### 4. DESCRIPTION OF ILLUSTRATIVE EMBODIMENTS

[0061] In the drawings and description that follows, like parts are marked throughout the specification and drawings with the same reference numerals, respectively. The drawings are not necessarily to scale. Certain features of the invention may be shown exaggerated in scale or in somewhat schematic form and some details of conventional elements may not be shown in the interest of clarity and conciseness. The present invention is susceptible to embodiments of different forms. Specific embodiments are described in detail and are shown in the drawings, with the understanding that the present disclosure is to be considered an exemplification of the principles of the invention, and is not intended to limit the invention to that illustrated and described herein. It is to be fully recognized that the different teachings of the embodiments discussed below may be employed separately or in any suitable combination to produce desired results. The various characteristics mentioned above, as well as other features and characteristics described in more detail below, will be readily apparent to those skilled in the art upon reading the following detailed description of the embodiments, and by referring to the accompanying drawings.

[0062] As a nonlinear optical imaging technique, coherent anti-Stokes Raman scattering (“CARS”) imaging has been demonstrated as a powerful tool for label-free optical imaging. This technique offers many advantages including (a) chemically selective contrasts based on Raman vibrational activity, (b) high sensitivity and rapid acquisition rates due to the coherent nature of the CARS process, (c) and sub-wavelength spatial resolution. Because of its highly directional, coherent properties, the CARS signal is several orders of magnitude stronger than the conventional Raman signal; therefore, CARS offers ultrafast imaging capability in video rate in vivo. In addition, the CARS signal is generated only at the laser focus, enabling point-by-point three-dimensional imaging for three-dimensional (3D) sectioning without a confocal aperture. As a result, CARS microscopy has been successfully applied to imaging viruses, cells, tissues, and live animals, using signals from CH<sub>2</sub>-abundant structures. CARS utilizes two laser beams. A pump beam at frequency  $\omega_p$  and a Stokes beam at frequency  $\omega_s$  (where  $\omega_s < \omega_p$ ) tightly focus

onto the sample, resulting in an emission signal at the anti-Stokes frequency ( $\omega_{CARS}=2\omega_P-\omega_S$ ). For spectroscopic or multiplex CARS applications, a femtosecond (“fs”) laser is often used as the Stokes wave by taking advantage of its broad spectral band to cover the spectral range of interest. For narrowband CARS imaging applications, picosecond (“ps”) lasers are typically used due to the reduction of the non-resonant CARS background, the excitation efficiency and the spectral resolution.

**[0063]** Single-mode fibers (“SMF”) and single-mode photonic crystal fibers (“PCF”) have been successfully demonstrated for use in the CARS imaging system. However, in order to satisfy the single-mode condition, the core diameter of the step-index SMF is typically limited to  $\sim 5 \mu\text{m}$ . Relatively small-sized core can make SMF susceptible to generating nonlinear effects, e.g., self-phase modulation (“SPM”), which may reshape the spectra of laser pulses. Although the core diameter of PCF is larger than SMF (e.g.,  $\sim 16 \mu\text{m}$  for large mode area PCF), the numerical aperture (“NA”) of PCF is usually small (e.g.,  $\sim 0.06$  for large mode area PCF) and, thus, results in difficulty and instability of laser coupling as well as small coupling efficiencies ( $<30\%$ ). This, in order to address these issues, in the present exemplary embodiments, multimode fibers (“MMF”) may be used for delivery of ultrafast pulses for CARS imaging. Compared to SMFs and PCFs, step-index MMFs have larger core diameters, larger NA, and larger coupling efficiency. In spite of these advantages, the delivery of two ultrafast pulses in the multimode fiber for CARS imaging has not been investigated.

**[0064]** Furthermore, in the exemplary embodiments, we may use standard commercial MMF, e.g., Corning SMF28 fibers, to deliver ps excitation lasers for CARS imaging. Furthermore, in several exemplary experimental embodiments, we experimentally analyzed issues associated with the fiber delivery, such as, for example, dispersion length, walk-off length, nonlinear length, average threshold power for self-phase modulations, and four-wave mixing (“FWM”). The exemplary experimental embodiments demonstrated that FWM signals are generated in MMF, but they can be filtered out by a long-pass filter for CARS imaging. Finally, we further demonstrated in exemplary experimental embodiments, that MMF can be used for delivery of ps excitation lasers without any degradation of CARS image quality.

**[0065]** Referring initially to FIG. 1, a microendoscopic system **100** includes a mode-locked laser **102** having an output that is operably coupled to an optical parametric oscillator (“OPO”) **104**. The output of the OPO **104** is operably coupled to an input of a dichroic mirror **106**, an output of the dichroic mirror **106** is operably coupled to an input of an optical filter **108**, and an input/output of the dichroic mirror is operably coupled to coupling lens **110**. The output of the optical filter **108** is operably coupled to an input of a photomultiplier tube (“PMT”) **110**. The coupling lens **110** is also operably coupled to an end of an optical fiber **112** and the other end of the optical fiber is operably coupled to a collimating lens set **114**. The collimating lens set **114** is also operably coupled to a two-dimensional (2-D) scanning mirror **116** and the 2-D scanning mirror is also operably coupled to an objective lens set **118** that may be positioned proximate a sample. The 2-D scanning mirror is further operably coupled to a control system **120** for controlling and monitoring the operation of the 2-D scanning mirror. A data acquisition system **122** is operably coupled to the PMT **110** and the control system **120** for monitoring and controlling the operation of the PMT and the

control system. A computer **124** is operably coupled to the data acquisition system **122** for monitoring and controlling the operation of the data acquisition system.

**[0066]** In an exemplary embodiment, during the operation of the system **100**, the system is operated to provide CARS microscopy, which provides for the imaging of chemical and biological samples by using molecular vibrations as a contrast mechanism. In particular, as will be recognized by persons having ordinary skill in the art, CARS microscopy uses at least two laser fields, a pump electromagnetic field with a center frequency at  $\omega_P$  and a Stokes electromagnetic field with a center frequency at  $\omega_S$ . The pump and Stokes fields interact with a sample and generate a coherent anti-Stokes field having a frequency of  $\omega_{AS}=2\omega_P-\omega_S$  in the phase matched direction. When the Raman shift of  $\omega_P-\omega_S$  is tuned to be resonant at a given vibrational mode, an enhanced CARS signal is observed at the anti-Stokes frequency,  $\omega_{AS}$ . Unlike fluorescence microscopy, CARS microscopy does not require the use of fluorophores (which may undergo photobleaching), since the imaging relies on vibrational contrast of biological and chemical materials. Further, the coherent nature of CARS microscopy offers significantly higher sensitivity than spontaneous Raman microscopy. This permits the use of lower average excitation powers (which is more tolerable for biological samples). The fact that  $\omega_{AS}>\omega_P, \omega_S$  allows the signal to be detected in the presence of background fluorescence.

**[0067]** In particular, in an exemplary embodiment, during the operation of the system **100**, the mode-locked laser **102** and the OPO **104** are operated in a well-known manner to generate a pump electromagnetic field with a center frequency at  $\omega_P$  and a Stokes electromagnetic field with a center frequency at  $\omega_S$ . The pump electromagnetic field and the Stokes electromagnetic field are then conveyed, in turn, through the dichroic mirror **106**, through the coupling lens **110**, the optical fiber **112** and the collimating lens set **114**. The pump electromagnetic field and the Stokes electromagnetic field are then bounced off the reflective surface of the 2-D scanning mirror **116**, and then conveyed through the objective lens set **118** onto a sample **120**. The CARS signal, having center frequency  $\omega_{AS}$ , reflected off of the sample **120** is then conveyed back through the objective lens set **118**, reflected off of the reflective surface of the 2-D scanning mirror **116**, conveyed through, in turn, the collimating lens set **114**, the optical fiber **112**, and the coupling lens **110**, reflected off of the reflective surface of the dichroic mirror **106**, and conveyed through the optical filter **108** and processed by the PMT **110** to generate a signal for processing by the data acquisition system **122** to thereby determine the molecular composition of the sample **120**.

**[0068]** In an exemplary embodiment, during the operation of the system **100**, the control system **120** controls and monitors the operation of the 2-D scanning mirror **116** such that the signals transmitted by the object lens set **118**, namely the pump electromagnetic field with the center frequency at  $\omega_P$  and the Stokes electromagnetic field with a center frequency at  $\omega_S$ , scan the surface of the sample **120** using, for example, a raster scan pattern. In an exemplary embodiment, the optical fiber **112** is provided as an assembly that includes the collimating lens set **114**, the 2-D scanning mirror **116** and the objective lens set **118**. In this manner, the optical fiber **112**, the collimating lens set **114**, the 2-D scanning mirror **116** and the objective lens set **118** as a separate and self-contained assembly in the form of a fiber probe system **126**. In an exemplary

embodiment, the optical fiber **112** has a low transmission loss characteristic in a broad wavelength range that may, for example, include a pump electromagnetic field with an infrared center frequency, a Stokes electromagnetic field with an infrared center frequency, and a CARS signal within the visible spectrum. In an exemplary embodiment, the optical fiber may be a SMF for conveying the pump electromagnetic field and the Stokes electromagnetic field and may be a SMF or a MMF for collection and conveyances of the CARS signal. In an exemplary embodiment, the optical fiber may be a MMF for collection and conveyances of the CARS signal in order maximize the efficiency of the collection of the CARS signal. In an exemplary embodiment, the 2-D scanning mirror **118** may, for example, be implemented using a piezoelectric and/or a micro-electro-mechanical system (“MEMS”). In an exemplary embodiment, the fiber probe system **126** may be packaged within a hypodermic needle.

**[0069]** In an exemplary embodiment, an optical isolator may be operably coupled between the collimating lens set **114** and the reflective surface of the 2-D scanning mirror **116**.

**[0070]** Referring now to FIG. 2, an exemplary embodiment of a micro-endoscopic system **200** is substantially identical in design and operation to the system **100** except as noted below. In an exemplary embodiment, the system **200** includes a conventional optical time delay **202** that is coupled to the output of the mode locked laser **122** for providing a time-delayed signal to a reflective surface of a dichroic mirror **204** that is operably coupled to the OP **104** and a reflective surface of the dichroic mirror **106**.

**[0071]** In an exemplary embodiment, during the operation of the system **200** an output signal from the mode locked laser **122** is time delayed by operation of the time delay **202**. The time delayed output signal from the time delay **202** is then combined with the output signals of the OPO **104** by operation of the dichroic mirror **204**. In an exemplary embodiment, during the operation of the system **200**, the mode locked laser **102** generates the Stokes electromagnetic field and the OPO **104** generates the pump electromagnetic field. In an exemplary embodiment, during the operation of the system **200**, the time delay **202** delays the Stokes electromagnetic field and then the dichroic mirror **204** combines the delayed Stokes electromagnetic field with the pump electromagnetic field such that the signals overlap with one another in space and time. The design and operation of the system **200** is otherwise substantially identical to the design and operation of the system **100**.

**[0072]** Referring now to FIG. 3, an exemplary embodiment of a micro-endoscopic system **300** is substantially identical in design and operation to the system **200** except as noted below. In an exemplary embodiment, the system **300** includes a wavelength division multiplexer **302** in place of the dichroic mirrors, **106** and **204**. In this manner, electromagnetic signals may be routed during operation of the system **300**.

**[0073]** In an exemplary embodiment, as illustrated in FIG. 3A, the wavelength division multiplexer **302** may include a plurality of multiplexers, **302a** and **302b**, that are cascaded to one another.

**[0074]** In an exemplary embodiment, as illustrated in FIG. 3B, the wave division multiplexer **302** may include a plurality of multiplexers, **302a** and **302c**, that are cascaded to one another.

**[0075]** In this manner, the system **300** provides a laser system **304** that includes the mode locked laser **102**, the OPO **104** and the time delay **202**. In this manner, the system **300**

provides a detection system **306** that includes the filter **108**, the PMT **110** and the multiplexer **302**. The design and operation of the system **300** is otherwise substantially identical to the design and operation of the system **200**.

**[0076]** Referring to FIG. 3C, in an exemplary embodiment, the system **300** includes a fiber probe system **310** that includes an optical fiber **310a** that is operably coupled, at one end, to the coupling lens **110** and operably coupled, at another end, to an end of a gradient index (“GRIN”) collimating lens **310b**. Another end of the GRIN lens **310b** is operably coupled to a reflective surface of a 2-axis scanning MEMS mirror **310c**. The reflective surface of the MEMS mirror **310c** is further operably coupled to a focusing lens **310d** oriented at a 90-degree angle relative to the axis of the GRIN lens **310b**. The MEMS mirror **310c** is further operably coupled to the control system **120** by one or more signal pathways **310e** for controlling a 2-axis actuator **310f** operably coupled to the reflective surface of the MEMS mirror. In an exemplary embodiment, the actuator **310f** displaces the mirror **310c** such that the mirror scans a 2-D region. In an exemplary embodiment, the actuator **310f** displaces the mirror **310c** such that the mirror provides a raster scan.

**[0077]** In an exemplary embodiment, the fiber probe system **310** is contained within an outer tubular housing **310g** that defines an opening at one end for the fiber **310a** and signal pathways **310e** and an opening at another end that is transverse to the axis of the housing for permitting electromagnetic energy reflected off of the reflective surface of the MEMS mirror **310c** to pass out of and into the housing. An end of a tubular support **310h** is coupled to the other transverse opening of the housing **310g** and another end of the tubular support houses and supports the focusing lens **310d**.

**[0078]** In an exemplary embodiment, the fiber probe system **310** further includes an inner housing **310i** and a further inner tubular support **310j** for providing support to the fiber **310a** and the GRIN lens **310b**.

**[0079]** In an exemplary embodiment, the optical fiber **112** and/or the fiber **310a** comprise a double clad photonic crystal fiber having: 1) single-mode operation for the excitation laser beams (i.e., the pump beam, the signal beam, and the Stokes beams); and 2) multimode operation for the collected signal (i.e., the CARS signal). In several experimental embodiments, we demonstrated that: a) the multimode operation for the collected signal was highly efficient; and b) low nonlinearity provided low signal distortion induced by the fiber. These were unexpected results.

**[0080]** In an exemplary embodiment, the system **300** may include a side-view probe and/or a front-view probe configuration.

**[0081]** In an exemplary embodiment, one or more of the systems **100**, **200** and **300** may be operated to identify cancer, and other, cells in patients in a multimodality image-guided intervention for cancer diagnosis using a computer tomography (“CT”) scan or magnetic resonance imaging—(“MRI”) guided system to target a tumor. In an exemplary embodiment, one or more of the systems **100**, **200** and **300** may then be operated to provide microendoscopy by inserting the fiber probe system **126** within the same cannula. With real-time optical imaging, the operator can directly determine the malignance of the tumor or perform fine-needle aspiration biopsy (“FNAB”) for further diagnosis. During this operation, stable microendoscopy image series are needed to quantify the tissue properties, but they are often affected by respiratory and heart systole motion even when the interventional

probe is held steadily. Thus, the present exemplary embodiments provide a microendoscopy motion correction (“MMC”) method using normalized mutual information (“NMI”)-based registration and a nonlinear system to model the longitudinal global transformations. Furthermore, in an exemplary embodiment, the MMC method includes the use of a cubature Kalman filter to solve the underlying longitudinal transformations, which yields more stable and robust motion estimation. After global motion correction, longitudinal deformations among the image sequences are then calculated to further refine the local tissue motion. In addition, the exemplary embodiments of the MMC method may be used in any microendoscopy image processing system to correct for microendoscopy motion and/or in any image processing system to correct for motion. Furthermore, the exemplary embodiments of the MMC method may be used in any image-processing system to correct for motion. Finally, exemplary experimental results showed that compared to global and deformable image registrations, MMC method yields more accurate alignment results for both simulated and real data than conventional motion-correction methods.

**[0082]** Referring now to FIG. 4, a minimally-invasive, multimodality image-guided (“MIMIG”) system 400 includes a fiber optic probe 402 that is operably coupled to an image data collection system (“IDCS”) 404. The IDCS 404 is also operably coupled to a motion-correction system 406 for implementing the MMC.

**[0083]** In an exemplary embodiment, the fiber optic probe 402 may be a conventional fiber optic probe that may, for example, be adapted to pass through a needle cannula 408 that is positioned proximate a tumor 410. In an exemplary embodiment, the fiber optic probe 402 may also include, or substitute, one or more aspects of the fiber probe system 126 of the systems 100, 200 and 300.

**[0084]** In an exemplary embodiment, the IDCS 400 may be a conventional IDCS. In an exemplary embodiment, the IDCS 400 may also include, or substitute, one or more aspects of the systems 100, 200 and 300.

**[0085]** In an exemplary embodiment, as illustrated in FIG. 5, the motion correction system 406 implements a MMC method 500 in which, in 502, the motion correction system obtains an image sequence  $I = \{I_1, I_2, \dots, I_N\}$  where  $N$  is the number of image frames, from the IDCS 404. In 504, the motion correction system 406 then calculates the global registration for the image data. In an exemplary embodiment, the global registration for the image data may be calculated in 504 in a conventional manner by, for example, calculating the global longitudinal transformations by maximizing the NMI. In 506, the motion-correction system 406 then applies the global registration to the image data. In 508, the motion-correction system 406 then calculates the deformable registration for the image data. In an exemplary embodiment, the deformable registration for the image data may be calculated in 508 in a conventional manner. In 510, the motion-correction system 406 then applies the deformable registration to the image data.

**[0086]** Referring now to FIG. 6, in an exemplary embodiment, in 504, the motion correction system 406 implements a method 600 for calculating the global registration for the image data in which the motion correction system iteratively minimizes an energy function  $E_g(M)$  to determine the value of  $M$  corresponding to minimum energy of the energy function, where  $M$  corresponds to the actual transformation, or serial alignment parameters, to be estimated:

$$E_g(M) = \frac{1}{N-1} \sum_{t=1}^{N-1} [-NMI(H_t \circ I_t, I_{t+1}) + \alpha \|H_t - f(M_t)\|^2], \quad (1)$$

**[0087]** where:

**[0088]** NMI refers to the normalized mutual information;  
**[0089]**  $H = \{H_1, H_2, \dots, H_{N-1}\}$  denotes the transformations, which may include either or both rigid and affine transformations, and may consist of serial translation, rotation, and scaling on actual images;

**[0090]**  $H_t \circ I_t$  is the globally transformed image  $I_t$  onto image  $I_{t+1}$ ;

**[0091]**  $\alpha$  is a weighting factor;

**[0092]**  $M_t$  is the actual transformation;

**[0093]**  $u_t$  is the system input;

$$\begin{cases} M_t = f(M_{t-1}, u_t) + n_t \\ H_t = g(M_t) + w_t \end{cases} \quad (2)$$

$M_t$  is the actual transformation or state of the system;

**[0094]**  $f(\bullet)$  is the nonlinear system function and does not need an explicit form when a cubature Kalman filter (“CKF”) is used;

**[0095]**  $u_t$  is the system input;

**[0096]**  $n_t$  and  $w_t$  are independent;

**[0097]**  $g(\bullet)$  is the system output function and is assumed to be an identity transformation; and

**[0098]**  $u_t$  is the input signal and is assumed to be zero.

**[0099]** The first term in equation (1) ensures that the NMI between consequence images are maximized while the second term in equation (1) provides that the longitudinal transformations are subject to a nonlinear model.  $H$  is the observation or output of the nonlinear system and  $M$  is the actual transformation or system states. The method 600 estimates  $M$ , given the images sequences  $I$ , and the measurable transformations,  $H$ .

**[0100]** In particular, in 602, given a current value for  $M$  the energy function  $E_g(M)$  is minimized, by constraining  $H$  to be similar to  $M$  by the motion correction system 406 to provide an estimate of  $H$  that minimizes the energy function  $E_g(M)$ . In 604,  $M$  is optimized by the motion correction system 406 by applying CKF to  $H$ . In 606, the motion correction system 406 determines if the numerical solution for estimating  $M$  is converging. If the numerical solution for estimating  $M$  is converging, then the method ends and the resulting value for  $M$ , which will typically be a matrix transformation, is used in 506 of the method 500.

**[0101]** In an alternative embodiment, in the method 600, augmented Kalman filtering (“AUKF”) may be used in addition to, or instead of, CKF in 604.

**[0102]** In an exemplary embodiment, in 508, the motion correction system 406 calculates the deformable registration for the image data by calculating the transformation vector  $v_t$ , from the image at timepoint  $t$  to the next timepoint,  $t+1$ , by minimizing the following energy function  $E_d(v)$ :

$$E_d(v) = \frac{1}{N-1} \sum_{t=1}^{N-1} \int_{\Omega} \|H_{t+1}[H_t(x) + v_t(x)] - I_t(x)\|^2 + \beta \|\nabla v_t(x)\|^2, \quad (3)$$

**[0103]** where  $\beta$  is the weight of the smoothness constraint.

**[0104]** In an exemplary embodiment, a fast 2-D implementation of the deformable registration may be used. In an exemplary experimental embodiment, it was found that NMI is more robust for global registration since NMI reflects more global image features. In an exemplary embodiment, further local refinement using deformable registration may be provided using image intensity information since 1) image intensity reflects relatively local image features, and 2) the deformable registration refinement is constrained by the result of global registration and the smoothness constraint. As a result, both accuracy and robustness can be obtained.

**[0105]** In several exemplary experimental embodiments, the performance of the method 600 was evaluated. In a first exemplary experimental embodiment of the method 600, the dataset consisted of microendoscopy image sequences generated by applying simulated serial translation, rotation, and scaling on actual images captured during an image-guided intervention procedure using a Cellvizio 660 system with added Gaussian noise to the images. In a second exemplary experimental embodiment of the method 600, the dataset consisted of microendoscopy image sequences acquired in an image-guided intervention on a lung-cancer rabbit model.

**[0106]** In the first exemplary experimental embodiment of the method 600, ten simulated microendoscopy sequences, using real microendoscopy frames collected from the rabbit experiments, were used. The longitudinal transformations were simulated using sine and cosine signals,

$$p_i(t) = a_i \sin(b_i t + \phi_i) + c_i, \quad (4)$$

**[0107]** where  $t=1, \dots, N-1$ ,  $i=1, \dots, 4$

**[0108]**  $a_i, b_i$ , and  $c_i$  are the amplitude, frequency and shifting of the transformation signals, respectively; and  $p_1, p_2, p_3, p_4$  represent the translations in x- and y-directions, rotation, and scaling.

**[0109]** In the first exemplary experimental embodiment of the method 600, the typical amplitude for translation was set to 10 pixels, rotation angles were  $[-20, +20]$  degrees and frequency was between 0.5 and 1. The scaling range was between 0.98 and 1.02.

**[0110]** In the first exemplary experimental embodiment of the method 600, image sequences were generated by first transferring the reference images using the simulated transformations and then adding spatially correlated Gaussian noises. Because only global longitudinal transformations were simulated, we compared the results of the method 600 with conventional NMI-based motion correction for global registration.

**[0111]** As illustrated in FIG. 7, FIG. 7A, FIG. 7B, FIG. 7C, FIG. 7D, and FIG. 7E, in the first exemplary experimental embodiment of the method 600, a reference image 700 was used to generate a series of simulated images, 700a-700e. As illustrated in FIG. 8A, FIG. 8B, FIG. 8C, FIG. 8D, and FIG. 8E, the method 600 was then implemented to correct for motion in the simulated images, 700a-700e, to thereby generate motion corrected images, 800a-800e.

**[0112]** In order to characterize the results of the first exemplary experimental embodiment of the method 600, as illustrated in FIG. 9A, FIG. 9B, FIG. 9C, FIG. 9D, and FIG. 9E, the difference, 900a-900e, between the reference image 700 and each of the motion corrected images, 800a-800e, respectively, was generated. As demonstrated by the difference images, 900a-900e, the difference between the reference

image 700 and the motion corrected images, 800a-800e, is virtually zero. This was an unexpected result.

**[0113]** Furthermore, in order to further characterize the results of the first exemplary experimental embodiment of the method 600, as illustrated in FIG. 10, the results of the first exemplary experimental embodiment of the method 600 were compared with an embodiment of a conventional NMI-based method of motion correction for global registration applied to simulated images. In particular, the amount of error between the results of the first exemplary experimental embodiment of the method 600 and the reference image 700 and the amount of error between the results of the conventional NMI-based method and the reference image 700 were compared. As illustrated in FIG. 10, the amount of error was significantly less for the first exemplary embodiment of the method 600 versus the conventional NMI-based method of motion correction for global registration. This was an unexpected result.

**[0114]** Furthermore, in order to further characterize the results of the first exemplary experimental embodiment of the method 600, as illustrated in FIG. 10, the results of the first exemplary experimental embodiment of the method 600 were compared with an embodiment of a conventional NMI-based method of motion correction for global registration applied to the simulated images. In particular, as illustrated below in Table 1, the average errors of the longitudinal transformations between the reference image 700 and the alignment results obtained using the method 600 and the conventional NMI method were determined and demonstrated that the method 600 provided significantly better results.

TABLE 1

AVERAGE ERRORS AND STANDARD DEVIATION FOR THE TEN SIMULATED IMAGE SEQUENCE		
	Motion Correction Method	
	NMI-Based Global Registration	Method 600
Average Error ( $\mu\text{m}$ )	2.2	1.3
Standard Deviation	0.3	0.1

**[0115]** Furthermore, the comparative results in Table 1 above demonstrated that the method 600 yields a significantly more accurate estimation of the longitudinal transformations in motion correction of image sequences. The exemplary comparative experimental results above demonstrated that the method 600 provides more accurate motion correction than that provided by conventional motion correction methods such as NMI-based motion correction for global registration. A conventional paired t-test of the exemplary experimental results detailed above also showed that such accuracy improvement is statistically significant ( $p < 0.05$ ). The improved results provided by the method 600 in the first exemplary experimental embodiment detailed above were unexpected.

**[0116]** In the second exemplary experimental embodiment of the method 600, microendoscopy videos were collected from lung-cancer rabbit model experiments during image-guided intervention. After cutting the microendoscopy videos into different clips based on image similarities, the method 600, the conventional NMI-based motion correction method for global registration, and the conventional NMI motion correction method for global registration plus a conventional deformable registration were applied to 30 microendoscopic video clips. For each video clip, an image with the smallest

difference to its neighboring frames was selected as the reference image, and all the other images were aligned with this reference image. The results obtained from the application of the method 600, the conventional NMI-based motion correction method, and the conventional NMI-based motion correction method plus a conventional deformable registration to the 30 microendoscopy video clips were then compared using a conventional NMI metric as a proxy for accuracy in the global registration provided by the respective motion correction methods. As illustrated below in Table 2, the method 600 provided significantly improved results versus both of the conventional motion correction methods.

TABLE 2

AVERAGE NMI VALUES IN EACH VIDEO Motion Correction Method				
	(a) NMI-Based Global Registration	(b) NMI-Based Global Reg. + Deformable Registration	(c) Method 600	Improvement Between (b) and (c) (%)
Average NMI	0.58	0.63	0.70	12.7%
Standard Deviation	0.07	0.08	0.08	

[0117] In a third exemplary experimental embodiment of the method 600, referring now to FIG. 11, FIG. 11A, FIG. 11B, FIG. 11C, FIG. 11D, FIG. 12A, FIG. 12B, FIG. 12C, and FIG. 12D, for further validation of the performance of the method, 30 microendoscopy video clips were collected from eight rabbit experiments. After cutting the whole microendoscopy videos into different video clips, an image with the least difference to its neighboring images was selected as the reference frame 1100 for each video clip, and a current frame 1100a was then aligned with this reference frame using the method 600 and the conventional NMI-based motion correction method for global registration. The third exemplary experimental embodiment of the method 600 provided a motion correction frame 1100b provided using the conventional NMI-based global registration method and motion corrected images, 1100c and 1100d, for the method 600. Note that motion corrected image 1100c was generated by the method 600 after one iteration, and the motion corrected image 1100d was generated by the method 600 after two iterations.

[0118] In the third exemplary experimental embodiment of the method 600, in order to further validate and compare the results of the method 600 with the results for the conventional NMI-based motion correction global registration method, difference images, 1200a, 1200b, 1200c and 1200d, were generated which illustrate: the difference between the image 1100a and the reference image 1100, the difference between the image 1100b obtained using the conventional NMI-based motion correction global registration method and the reference image 1100, the difference between the image 1100c obtained using the method 600 and the reference image 1100, and the difference between the image 1100d and the reference image 1100. A visual examination of the difference images clearly indicates that the method 600 was far superior to the conventional NMI-based motion correction global registration method. Furthermore, as a further validation of the exemplary experimental results, conventional NMI metrics were also calculated for the motion corrected images obtained

using the method 600 and the conventional NMI-based motion correction global registration method. The results of these NMI metric calculations indicated that the accuracy of image alignment was better for the method 600 versus the NMI-based motion correction global registration method for all the 30 image sequences studied. The average improvement provided by the method 600, versus the conventional NMI-based motion correction global correction method, was 6.6% and the largest one being 12.46%. All of the improved results provided by the method 600 were unexpected results.

[0119] In an exemplary embodiment, in 504, the motion correction system 406 calculates the global registration for the image data using a conventional hidden Markov model (“HMM”) method for motion correction. Basically, the conventional HMM method assumes that the motion of the current line to the next line in a scanned image remains the same or is most likely not changing. A standard exponential model, or distribution, is typically used to describe this assumption. Essentially, this assumption is only realistic when the patient is still or relatively still, the relative position for the scanning beam and patient’s region of interest stays constant, but this situation is not very common because a patient’s motion may be disordered and random and may include sudden changes of speed all of the time during the procedure. Thus while HMM may work effectively for the resting stage, it might fail and give a wrong estimation during a rapid movement stage.

[0120] Thus, as illustrated in FIG. 13, in an exemplary embodiment, in 504, the motion correction system 406 calculates the global registration for the image data using an extended version of HMM by incorporating an estimated speed into the state transition model for more accurate estimation to provide a speed embedded HMM (“SEHMM”) method 1300. In particular, in 1302, initial motion estimation is achieved by using a line-by-line searching method. Then, in 1304, a grouping algorithm is used to divide the whole imaging period into resting and running stages for speed estimation. Finally, in 1306, SEHMM is then adopted for motion correction.

[0121] In an exemplary embodiment, as illustrated in FIG. 14, in 1306, the motion correction system 406 implements a SEHMM method 1400 for motion correction.

[0122] As described above, in general, the systems 100, 200 and 300 capture a series of images by passing a focus of laser excitation repeatedly over region of a sample 120 and collecting the resulting photons via a photon multiplier 110. Although the motion of the sample 120 is in 3D, Z-axis motion shift is typically less than 1 μm for a scanning speed of 2 ms/line, much lower than the X (medial-lateral direction along the raster scan line) and Y (rostral-caudal direction across the raster scan line) directions. Therefore, the primary task of the method 1400 is to estimate the motion in X and Y directions. Due to the motion of the sample 120 during the raster scan progression, the relative motion can be written as:

$$\begin{cases} X_i^{rk} = X_i^k + \delta_x^k \\ Y_i^{rk} = Y_i^k + \delta_y^k \end{cases} \quad (5)$$

[0123] where  $X_i^k(t) = \{t/(\tau/N)\} \cdot N$  and  $X_i^{rk}(t) = [t/(\tau/N)]$  are the actual location of an object point;

[0124]  $(\delta_x^k, \delta_y^k)$  is its offset due to motion;

[0125]  $N \times N$  is the size of each frame;

[0126]  $[\cdot]$  represents the integer operation;

[0127]  $\{\cdot\}$  denotes the fractional operation; and

[0128]  $\tau$  is the scanning time for a frame.

[0129] In an exemplary embodiment, the laser output of the systems **100**, **200** and **300** moves in a zigzag pattern in X-direction and a step-function pattern in Y-direction. Thus, the goal of the method **1400** is to estimate the offsets  $(\delta_x^k, \delta_y^k)$  from the serial images. Equation (5) assumes that each line has the same relative displacement, so we can choose a line-by-line motion correction algorithm to solve this problem. The reason is that the shifts for all the pixels within a line do not get beyond one-pixel in the Y-direction and are very tiny in X direction. Although pixel-by-pixel correction can yield more accurate results, one has to trade off between speed and the gain in accuracy.

[0130] The SEHMM method **1400** is an extension of the conventional HMM method by using a motion prediction model with HMM to better estimate the state transition probability. In particular, denoting the displacement state for line  $k$  as  $(\delta_x^k, \delta_y^k)$ , it is necessary to define the state observation probability  $\pi_k^{\delta_x, \delta_y}$  and the state transition probability  $T[(\delta_x^{k-1}, \delta_y^{k-1}) \rightarrow (\delta_x^k, \delta_y^k)]$ . During the operation of the SEHMM method **1400**, the transition probability of the displacement state is estimated based on the estimated moving speed. Thus, the SEHMM method **1400** can match motion more accurately not only during the resting stage but also during the moving stage.

[0131] The transition probability is defined as:

$$T(\delta_x^{k-1}, \delta_y^{k-1}) \rightarrow (\delta_x^k, \delta_y^k) = \frac{1}{2\pi\lambda} e^{-r/\lambda}, \quad (6)$$

[0132] where  $r$  is defined as:

$$r = \sqrt{(\delta_x^k - (\delta_x^{k-1} + v_x^{k-1,k} \tau_{line}))^2 + (\delta_y^k - (\delta_y^{k-1} + v_y^{k-1,k} \tau_{line}))^2}, \quad (7)$$

[0133] where  $v_x^{k-1,k}$  and  $v_y^{k-1,k}$  are the estimated speed of the motion from line  $k-1$  to  $k$  for X- and Y-directions, respectively; and

[0134]  $\tau_{line}$  is the scanning time for a line.

[0135] By using Eq. (7), if the moving speed is estimated at line  $k-1$ , the offset at line  $k$  can be estimated. Therefore, in the SEHMM method **1400**, we no longer assume that the state transition probability is the highest when the sample **120** does not move. On the contrary, this probability gets its peak at a linearly estimated offset value. Since the goal for motion correction is to estimate  $\delta_x^k, \delta_y^k$  for each line  $k$  from a given reference frame  $R$  and the current image  $I$ , we implement it by maximizing a posteriori,

$$P = \frac{P(\delta_x^k, \delta_y^k | I^k, R) = P(I^k | R, X^k, Y^k) \cdot P(\delta_x^k, \delta_y^k | \delta_x^{k-1}, \delta_y^{k-1})}{\sum_{\delta_x, \delta_y} P(\delta_x^{k-1}, \delta_y^{k-1}) \rightarrow (\delta_x^k, \delta_y^k)}. \quad (8)$$

[0136] Expressing  $P$  as a logarithm probability, one gets,

$$\ln(P) = \ln(\pi_k^{\delta_x, \delta_y}) + \ln(T). \quad (9)$$

[0137] The first term in Eq. (9) is the state observation probability  $\pi_k^{\delta_x, \delta_y}$  and reflects the goodness of matching between a line in the current frame  $I$  and the corresponding line in the reference frame  $R$ . Denoting the intensity of the  $i$ th pixel in the  $k$ th line of the current frame as  $I_i^k$  and that of the

corresponding pixel in the reference frame as  $(x_i^k, y_i^k)$ , the observation probability can be modeled as a discrete Poisson distribution explicitly,

[0138]  $\pi_{k,i}^{\delta_x, \delta_y} = (\gamma R)^{I_i^k} \cdot e^{-\gamma R} / (\gamma!)^I$ , where  $\gamma$  is the calibration factor of the photon number, which is an inherent factor in an imaging system. Taking the logarithm transformation of  $\pi_{k,i}^{\delta_x, \delta_y}$  we get,

$$\ln(\pi_{k,i}^{\delta_x, \delta_y}) = \gamma I \ln(\gamma) + \gamma I \ln(R) - \ln((\gamma!)^I) - \gamma R, \quad (10)$$

[0139] where  $\gamma$  and  $I_i^k$  are independent of the changing offsets, and  $R$  is indeed a function of the offsets. Thus equation (10) can be simplified as,

$$\ln(\pi_{k,i}^{\delta_x, \delta_y}) \propto \gamma(I \ln(R) - R). \quad (11)$$

[0140] Then, the observation probabilities for all the pixels within line  $k$  can be calculated by,

$$\ln(\pi_k^{\delta_x, \delta_y}) = \sum_{i=1}^N \ln(\pi_{k,i}^{\delta_x, \delta_y}). \quad (12)$$

[0141] Thus, in an exemplary embodiment, the method **1400**, in **1402**, defines the state observation probability  $\pi_k^{\delta_x, \delta_y}$  and the state transition probability  $T[(\delta_x^{k-1}, \delta_y^{k-1}) \rightarrow (\delta_x^k, \delta_y^k)]$ .

[0142] Once the state observation probability and the state transition probability are defined in **1402**, the best displacement signal can be calculated by maximizing Eq. (9), by following two iterative steps:

[0143] First, in **1404**, the value of  $\lambda$  that leads to the highest probability for Eq. (9) is determined. In an exemplary embodiment, the value of  $\lambda$  that leads to the highest probability for Eq. (9) may be determined by systematically scanning values of  $\lambda$  in a prescribed range. In an exemplary embodiment, the values of  $\lambda$  may be scanned uniformly in log space to get constant percentage sampling. For each value of  $\lambda$ , the method **1400** may be implemented to find the most optimal offset sequence and calculate its total probability. In an exemplary embodiment, the value of  $\lambda$  chosen in **1402** is the one with the most probable offset sequence.

[0144] Then, in **1406**, the most likely sequence of the hidden states, offsets, may be determined using a Viterbi algorithm. In an exemplary embodiment, this can be accomplished in two steps. First, determine the most probable offset sequence for every state at time, line,  $k$  from any of the states at time, line,  $k-1$  by marching forward through the time domain. Then, in **1408**, a backtrack along the path of the most probable offset sequence to record the results of optimal offset sequence. In an exemplary embodiment, a line-by-line search is first used to estimate the initial offset, and the speed of the motion can be estimated by applying smoothness filter temporally on the estimated offsets before implementing the SEHMM method **1400**.

[0145] In order to illustrate how the SEHMM method **1400** works, referring now to FIG. **15A** and FIG. **15B**, exemplary state transition probabilities for HMM and SEHMM models, **1500a** and **1500b**, respectively, are illustrated. The center of each distribution plot is set to  $(\delta_x^{k-1}, \delta_y^{k-1})$ , and it can be seen that the peak of the state transition probability **1500a** is right in the middle for the HMM model while the peak for the SEHMM state transition probability **1500b** is shifted as a result of the motion estimation provided by operation of the method **1400**. A shifting of the peak of the probability func-

tion indicates that a motion is assumed from one line to another. This compensation for adding the estimated speed value from the current offset to the following offset can remarkably improve the estimation accuracy because it satisfies the prediction requirement in all the time points but not only in the still time points.

[0146] In an exemplary experimental embodiment of the SEHMM method **1400**, in order to validate the method, as illustrated in FIG. 16, FIG. 16A, FIG. 16B, FIG. 16C, and FIG. 16D, simulated serial images were used to quantitatively validate the SEHMM method by comparing the SEHMM method with a conventional HMM method. Temporal displacements were first generated to transfer a real 2-D image, **1600**, to produce longitudinal image sequences, **1600a-1600d**. The displacement signal, for generating the images, **1600a-1600d**, was generated on a pixel-by-pixel basis using a first differential equation with a characteristic time constant driven by a combination of the random and deterministic processes to simulate the effect of acquiring laser-scanning data from a moving sample:

$$\begin{cases} \bar{\phi}_x^{t+1} = \left(1 - \frac{1}{\tau}\right)\bar{\phi}_x^t + \frac{1}{\tau}(\xi_{\sigma_x}^t + \bar{D}_x^t) \\ \bar{\phi}_y^{t+1} = \left(1 - \frac{1}{\tau}\right)\bar{\phi}_y^t + \frac{1}{\tau}(\xi_{\sigma_y}^t + \bar{D}_y^t), \end{cases} \quad (13)$$

[0147] where  $\bar{\phi}_x^t$  and  $\bar{\phi}_y^t$  denote the simulated offsets for X- and Y-directions, respectively; and

[0148]  $t$  expresses the time-point;

[0149]  $t=(k-1)N+i$ ;

[0150]  $\tau$  is set to 500;

[0151]  $\sigma_x$  and  $\sigma_y$  ( $\sigma_x=4, \sigma_y=40$ ) are the standard deviations

of the Gaussian random variables  $\vec{\xi}_{\sigma_x}$  and  $\vec{\xi}_{\sigma_y}$ ; and

[0152]  $\bar{D}_x^t$  and  $\bar{D}_y^t$  are the step functions at the time.  $t$

[0153] In the exemplary experimental embodiment of the SEHMM method **1400**, Poisson noise was added on a pixel-by-pixel basis to simulate the photon-counting statistic because the values during scanning are Poisson distributed in terms of photon numbers but not in units of pixel intensity.  $\sigma_x$ ,  $\sigma_y$ , and  $\tau$  control the amplitudes of temporal dynamic displacements.

[0154] In the exemplary experimental embodiment of the SEHMM method **1400**, two simulated data sets, T1 and T2, were generated with these default parameters. In addition, the values of  $\sigma_x$ ,  $\sigma_y$ , and  $\tau$  were changed and the other parameters remained constant. Two more datasets, T3 and T4, were simulated by setting  $\sigma_x=10$ ,  $\sigma_y=30$  and  $\tau=200$ . The number of frames for T1, T2, T3, and T4 were 65, 82, 56 and 51, respectively. The image size was 129×129, and the resolution was 0.39  $\mu\text{m}/\text{pixel}$ .

[0155] In the exemplary experimental embodiments of the SEHMM method **1400**, the exemplary experimental results for the conventional HMM method were denoted as  $(\delta_x^k, \delta_y^k)$  and the exemplary experimental results for the SEHMM method were denoted as  $(\hat{\delta}_x^k, \hat{\delta}_y^k)$  the simulated offsets were denoted as  $(\phi_x^t, \phi_y^t)$ , and the exhaustive search results denoted as  $(\hat{\delta}_x^k, \hat{\delta}_y^k)$ , and we compared the motion correction accuracy provided by the different methods. Because all of methods tested were line-by-line motion correction methods and the ground truth was stored in pixel resolution, we took the mean value of all ground truth offsets within each line and then rounded the mean value to the nearest integral, i.e.,  $\phi_x^t$ ,

$\phi_y^t \rightarrow \phi_x^k, \phi_y^k$ . The differences between these two were also compared, which indicated the accuracy of the line-by-line based methods. We used the following five performance measures: average distance (“AD”), average distance for Y-direction (“ADY”), average distance for X-direction (“ADX”), standard deviation for Y-direction (“SDY”) and standard deviation for X-direction (“SDX”), to evaluate the performance of the different methods.

[0156] FIG. 17A, FIG. 17B, FIG. 17C, and FIG. 17D illustrate the comparison results between the four line-by-line results and the ground truth for data sets, T1, T2, T3, and T4, respectively. The dark blue bars show differences between the rounded line-by-line ground truth and the simulated pixel-by-pixel ground truth, and other bars show the results of the three methods, namely the exhaustive method, the HMM method, and the SEHMM method **1400**. It can be seen that for the performance measures used, the SEHMM method **1400** yielded the smallest errors (some with slightly larger SDX).

[0157] In the exemplary experimental embodiments of the SEHMM method **1400**, we also focused on the Y-direction because the offsets in this direction have relatively large movement than in X-direction. FIG. 18 illustrates the results for the simulated dataset T4. In FIG. 18, the line-by-line rounded ground truth, the results of the SEHMM method **1400**, and the results of the conventional HMM method are shown. Furthermore, the inconsistencies between the results of the SEHMM method **1400**, and the results of the conventional HMM methods are also shown. The inconsistency was calculated as the number of lines within a frame for which the results of SEHMM method **1400** and the conventional HMM method were different from the ground truth. As illustrated in FIG. 18, during resting stage, such inconsistency is small, and both the SEHMM method **1400** and the conventional HMM method yielded good results, about 10 lines were different, but during the movement stage, the SEHMM method **1400** reduces the inconsistency as compared with the results of the conventional HMM method. All of these exemplary experimental results were unexpected.

[0158] In another exemplary experimental embodiment of the SEHMM method **1400**, the mean absolute intensity difference was used as the measure to show the performance of the methods. The mean absolute intensity difference across longitudinally corresponding pixels reflects the goodness of matching for the image sequences. Table 3 below shows the comparative results for datasets, T5 and T6, provided by an anonymized group, respectively, using the different methods. The number of frames was **1200** and **200**, image size was 128×128 and 256×256, respectively, and the resolution was 0.39  $\mu\text{m}/\text{pixel}$  for both. The improvement can be seen from the comparison results when we adopt the proposed method.

TABLE 3

AVERAGE OF ABSOLUTE INTENSITY DIFFERENCES FOR REAL DATASETS T5 AND T6				
Data Set	Original Data	Exhaustive Method	HMM	SEHMM
T5	7.05	5.89	5.48	5.03
T6	9.54	7.74	7.15	6.56

[0159] In the other exemplary experimental embodiment of the SEHMM method **1400**, the SEHMM method **1400** again provided superior accuracy versus the conventional HMM method. This was an unexpected result.

[0160] Thus, the exemplary experimental embodiments of the SEHMM method 1400 demonstrated that a SEHMM method for motion correction provided far superior accuracy to conventional motion correction methods for global registration such as HMM. In particular, the SEHMM method 1400 provided a much better estimate of the state transition probability compared to the conventional HMM method that assumed no motion always has the highest probability. Furthermore, the SEHMM method 1400 can model the motion more accurately and operates directly on the motion-distorted image data without any external signal measurement such as the sample movements, heartbeat, respiration, or muscular tension. Using simulated and real images, it was demonstrated that the SEHMM method 1400 was more accurate than the conventional HMM method—using both simulated and real image sequences. This was an unexpected result.

[0161] Thus, in the exemplary experimental embodiments of the SEHMM method 1400, a quantitative validation was performed to compare conventional HMM with the SEHMM method 1400 based on both simulated data and real data. First, simulated image sequences were generated to mimic various real motion situations, and different dynamic amplitudes were applied to make the validation more realistic and reasonable. For real data, the comparative results demonstrated the performance of the SEHMM method 1400. The exemplary experimental embodiments' results showed that the SEHMM method 1400 achieved higher estimation accuracy and image alignment results as compared with conventional HMM, especially in the running stages of the image sequences.

[0162] In an exemplary embodiment, as illustrated in FIG. 19A and FIG. 19B, the motion correction system 406 may be used, for example, to correct for breathing motion in images obtained from lung tissue, by implementing a method 1900 for motion correction. More generally, the teachings of the method 1900 may be used to correct for motion in any type of sample 120 to provide global registration of a sequence of images.

[0163] In 1902, lung field segmentation is performed on a series of images. In an exemplary embodiment, lung field segmentation may be performed using a joint segmentation and registration method to thereby extract the lung field by first removing the background and cavity areas and then performing 3D morphological clean up in the segmented lung field. In an exemplary experimental embodiment, in 1902, as illustrated in FIG. 20, a segmented lung field 1902a was generated.

[0164] In 1904, serial image registration of the images is performed.

[0165] In 1906, registration of the first time point image onto a template image is performed. In an exemplary experimental embodiment, in 1906, as illustrated in FIG. 21, surfaces extracted from a 7<sup>th</sup> image before, in blue, and after, in red, registered to the 1<sup>st</sup> image, shown as the background. It can be seen that the deformable registration tracked respiratory motion well.

[0166] In 1908, the normalized lung field motion vectors and the corresponding fiducial motion vectors are extracted.

[0167] In 1910, a lung motion statistical model is constructed by using a kernel principal component analysis ("K-PCA") on the surface motion vectors.

[0168] In an exemplary embodiment, K-PCA is a nonlinear statistical modeling method that can capture the variations of shapes more accurately than PCA. The basic idea is that PCA

computed in a high-dimensional implicit mapping function  $\phi(v)$ , or the feature space, of the surface motion vector  $v$  can be replaced as a PCA of the kernel matrix. Let  $k$  denote the kernel matrix of  $N$  sample surface motion vectors, i.e.,  $k_{ij}=k(v_i, v_j)$ , K-PCA can be computed in a closed form by finding the first  $M$  eigenvalues  $v_i$ , and eigenvectors  $a_i$  of  $K$ , i.e.,  $KA=AV$ . The corresponding eigenvectors in the feature space can also be computed by multiplying the mapping function values of the samples with  $A$  and preserve the variance of data in the feature space. Therefore, given a surface motion vector  $v$ , it can be projected onto the K-PCA space as,

$$\lambda = A^T(k - \bar{k}), \quad (14)$$

[0169] where  $\bar{k}$  is the mean of kernel vectors, and  $k$  is the kernel vector of  $v$ , i.e.,

[0170]  $k_i = k(v, v_i), i=1, \dots, N$ . Because in K-PCA the feature space is induced implicitly, reconstruction of a new vector  $v$  given a feature  $\lambda$  is not trivial, which can be defined in many ways, and different cost functions will lead to different optimization problems.

[0171] In 1912, a lung motion estimation model is trained using a least squared support vector machine ("LS-SVM") to model the relationship between the fiducial signals lung motion feature vectors on the K-PCA space.

[0172] In an exemplary embodiment, in 1912, the goal of motion estimating is to establish the relationship between the lung field surface motion,  $v$  (represented by  $\lambda$  in the K-PCA space) with the fiducials' motion  $v^{(d)}$ . Therefore, given  $N$  training sample-pairs  $\{(v_i^{(d)}, \lambda_i)\}, i=1, \dots, N$ , the relationship between fiducial  $v_i^{(d)}$  and lung field motion feature vector  $\lambda_i$  needs to be established. In this work, we employ the ridge regression method with the LS-SVM model. Given the time series of the motion vectors  $\lambda_{i,t}, i=1, \dots, N; t=1, \dots, T$  and those of the fiducial motion vectors  $v_{i,t}^{(d)}$ , the goal is to estimate the motion estimation function, i.e.,  $\lambda(t) = \theta(v(t)) + e(t)$ , where  $e$  is a random process with zero mean and  $\text{std } \sigma_e^2$ . Because the elements of  $\lambda(t)$  are independent each other in the K-PCA space, we can use the least squares support vector machines ("LS-SVM") model to estimate each element of  $\lambda(t)$ . Denoting  $\lambda$  as one element of  $\lambda$  at time  $t$ , we can estimate it using:

$$\lambda = w^T \phi(v^{(d)}) + b, \quad (15)$$

[0173] where  $\phi(\cdot)$  denotes a potential mapping function.  $w$  is the weights, and  $b$  is the shifting values. The regularized cost function of the LS-SVM is provided in a conventional manner,

$$\min_{w, b, e} \xi(w, e) = \frac{1}{2} w^T w + \frac{\gamma}{2} \sum_{i=1}^N \|e_i\|^2 \quad (16)$$

s.t.

$$\lambda_i = w^T \phi(v_i^{(d)}) + b + e_i,$$

$$i = 1, \dots, N.$$

[0174]  $\gamma$  is referred to as the regularization constant. This optimization actually corresponds to a ridge regression in feature space. The Lagrangian method is utilized to solve the constrained optimization problem, and hence the new cost function becomes:

$$\zeta(w, b, e; \alpha) = \zeta(w, e) - \sum_{i=1}^N \alpha_i (w^T \phi(v_i^{(d)}) + b + e_i - \lambda_i), \quad (17)$$

**[0175]** with  $\alpha_i$  as the Lagrange multipliers. The conditions for optimality are equivalent to the following linear equation:

$$\begin{bmatrix} 0 & 1_N^T \\ 1_N & \Omega + \gamma^{-1} J_N \end{bmatrix} \begin{bmatrix} b \\ \alpha \end{bmatrix} = \begin{bmatrix} 0 \\ \Lambda \end{bmatrix}, \quad (18)$$

**[0176]** where  $\Lambda = [\lambda_1, \dots, \lambda_N]^T$  is the vector formed by the  $N$  samples of an element of vector  $\lambda_N = [1, \dots, 1]^T \in \mathbb{R}^N$ ,  $\Omega_{i,j} = \Pi(v_{i,t}^{(d)}, v_{j,t}^{(d)}) = \phi(v_{i,t}^{(d)})^T \phi(v_{j,t}^{(d)}) \forall i, j = 1, \dots, N$  with  $\Pi$  as the positive definite kernel function. Notice that because of the kernel trick, the feature mapping  $\phi(\cdot)$  is never defined explicitly, and we only need to define a kernel function  $\Pi(\cdot, \cdot)$  of the fiducial vectors. The typical radial basis function (“RBF”) kernel  $\Pi(v_{i,t}^{(d)}, v_{j,t}^{(d)}) = \exp(-\|v_{i,t}^{(d)} - v_{j,t}^{(d)}\|^2 / \sigma^2)$ , where  $\sigma$  denotes the bandwidth of the kernel. After solving Eq. (18), we get  $\alpha$  and  $b$ , and the element of lung motion feature vector  $\lambda$  can be calculated for given fiducial motion vector  $v^{(d)}$ :

$$\lambda = \sum_{i=1}^N \alpha_i \Pi(v^{(d)}, v_i^{(d)}) + b. \quad (19)$$

**[0177]** Notice that because different elements of the lung motion feature vector are independent, all of the elements at different time points are calculated by this model separately, similar to model the motion according to different lung capacity.

**[0178]** In 1914, respiratory signals of a patient are transferred onto the template space in order to use the motion estimation model to estimate lung motion feature vectors and reconstruct the lung surface motion vectors of the patient.

**[0179]** In 1916, serial deformations are generated using the surface motion vectors as constraints in a serial deformation simulator.

**[0180]** In 1918, the serial deformation fields are transformed onto the subject space to generate the serial images for visualization during treatment of the patient.

**[0181]** Thus, as illustrated in FIG. 22, the method 1900 provides a motion correction method for use with four-dimensional computed tomography (4D-CT) scans of lung tissue that includes the estimation of a lung motion model that may then be used to correct for lung motion on a real time basis during treatment of a patient.

**[0182]** In an exemplary embodiment, the method 1900 includes preprocessing, in 1902, 1904 and 1906, including lung field segmentation, serial image registration for lung motion estimation, and registration of the first time-point image of different subjects onto a template image.

**[0183]** In an exemplary embodiment, the method 1900 includes a training stage, in 1908, 1910, and 1912, in which the normalized lung field surface motion vectors and the corresponding fiducial motion vectors of each subject are extracted, K-PCA is performed on the surface motion vectors to construct the lung motion statistic model and reduce the dimensionality for surface points, and a lung motion estimation model is trained using the least squared support vector

machine (“LS-SVM”) algorithm to model the relationship between fiducial signals and lung motion feature vectors projected on the K-PCA space.

**[0184]** Finally, in an exemplary embodiment, the method 1900 includes an estimation stage, in 1914, 1916 and 1918, in which an intra-procedural 3D CT and real-time tracked fiducial signals of a patient are available. The respiratory signals of the patient can be transferred onto the template space in order to use the motion estimation model to estimate the lung motion feature vectors and reconstruct the lung motion vectors, surface motion vectors, of the patient. Serial deformations are generated by using the surface motion vectors as constraints in a serial deformation simulator. The serial deformation fields are finally transformed onto the subject space to generate the serial CT images for online visualization during intervention.

**[0185]** In an exemplary embodiment of the method 1900, if the baseline image of the patient to be tested is  $I_1^{(p)}$ , we can first register the baseline image onto the template image  $T$  using deformable registration  $\Phi_{T \rightarrow P}: T \rightarrow I_1^{(p)}$ , and  $\Phi_{T \rightarrow P} = \{G, f\}$  consists of both global  $G$  and deformable  $f$  components of the registration. The corresponding lung field surface of the patient  $v_1^{(p)}$  can also be aligned onto the template as  $v_1$ . Similarly, the fiducial movement  $v; d.P$  can be aligned onto the template space, denoted as  $v_t^{(d)}$ . Notice that global transformation  $a$  needs to be applied to the fiducial motion because we are dealing with different spaces. We can then use Eq. (19) to estimate the serial lung motion feature vectors and reconstruct the lung field motion from K-PCA space to the template image space, denoted as  $v_t, t=2, \dots, T$ . A conventional lung field motion vector-constrained deformation simulation method is then applied to generate the serial deformation fields. Finally, the deformations are transformed onto the subject space using  $\Phi_{T \rightarrow P}$ . The values of these deformation vectors are subject to the global transformation  $G$  also.

**[0186]** In several exemplary experimental embodiments of the method 1900, thirty 4D-CT datasets from thirty different patients were processed using the method. In the exemplary experimental embodiments, twelve 3D images were acquired for each patient, and the images were aligned so that the first and the last images were exhale data and the 7<sup>th</sup> data was the inhale data. All of the images had an in-plane resolution of 0.98x0.98 mm and a slice thickness of 1.5 mm. To ensure consistent lung field surface representations, one image was randomly selected as the template, and the lung field surface for the selected template image was constructed first. Then, image segmentation and registration was applied to deform the lung field surface of the template image onto all the other images. In this way, we obtained lung field surface correspondences across different subjects and different time-points to ensure that the surfaces had the same trajectory. Using the same strategy, artificial fiducials were automatically put onto the surface of the chest/belly of each CT image. We used a leave-one-out method to evaluate the proposed algorithm. Each time the baseline images from twenty-eight subjects were registered onto the template image for training the lung motion estimation model. Then, the baseline image of the left-out subject and the fiducial movement signals of the left-out subject were used to estimate the serial CT images.

**[0187]** In the exemplary experimental embodiments of the method 1900, the errors between the estimated lung field surface and the actual surface at each time point as well as the volumes of the lung fields were used to evaluate the accuracy of the estimation. The procedure was iterated 29 times with

one subject left out each time after selecting one image as the template. The following equation was used to calculate the prediction errors for lung field surfaces:

$$\Delta_i = 1/28 \sum \text{dist}(v, \hat{v}), \text{ subject } i \text{ is left out.} \quad (20)$$

[0188] where the distance between two surfaces is defined as the average of distances from all the points in one surface to the other surface. Another quantitative measure is the volume of the lung. Because the lung fields from both estimated CT and the original CT images were available, we simply calculated the lung volumes and compare whether they are quantitatively close.

[0189] In several exemplary experimental embodiments of the method 1900, as illustrated in FIG. 23A, FIG. 23B, and FIG. 23C, exhalation images, 2302, 2304 and 2306, were obtained. In the several exemplary experimental embodiments of the method 1900, as illustrated in FIG. 24A, FIG. 24B, and FIG. 24C, inhalation images, 2402, 2404 and 2406, corresponding to the exhalation images, FIG. 23A, FIG. 23B, and FIG. 23C, respectively, which also illustrated the predicted lung field in blue contours and the actual lung field position was illustrated in red contours.

[0190] In the several exemplary experimental embodiments of the method 1900, as illustrated in FIG. 25A, FIG. 25B, and FIG. 25C, the predicted and actual changes of lung volumes corresponding to the exhalation images, FIG. 23A, FIG. 23B, and FIG. 23C, respectively, were generated which indicated high accuracy between the true volume change during breathing and the predicted results. This was an unexpected result.

[0191] In the several exemplary experimental embodiments of the method 1900, in order to further validate the experimental results, the average lung field estimation errors for 8 experiments were calculated using Eq. (20), and each result was tested on the left-out subject image as detailed below in Table 4. It can be seen below in Table 4 that the average errors over the serial images are between 1.22 mm and 2.18 mm with an average of 1.63 mm. Overall, an acceptable range of errors was obtained for predicting the lung motion. This was an unexpected result.

TABLE 4

AVERAGE ERRORS FOR LUNG MOTION ESTIMATION USING LEAVE-ONE-OUT VALIDATION (UNITS IN MM)												
Time	T2	T3	T4	T5	T6	T7	T8	T9	T10	T11	T12	Mean
Pat. 1	1.20	1.39	1.61	1.64	2.69	3.49	2.75	2.75	2.88	1.94	1.63	2.18
Pat. 2	0.98	1.14	1.31	1.34	2.20	2.85	2.25	2.25	2.36	1.59	1.33	1.78
Pat. 3	1.08	1.25	1.44	1.47	2.42	3.14	2.47	2.48	2.59	1.75	1.46	1.96
Pat. 4	0.83	0.96	1.11	1.13	1.86	2.42	1.90	1.91	1.99	1.34	1.13	1.51
Pat. 5	0.90	1.04	1.20	1.23	2.01	2.62	2.06	2.06	2.16	1.46	1.22	1.63
Pat. 6	0.77	0.89	1.03	1.05	1.73	2.24	1.77	1.77	1.85	1.25	1.05	1.40
Pat. 7	0.67	0.78	0.90	0.92	1.51	1.96	1.54	1.55	1.62	1.09	0.92	1.22
Pat. 8	0.72	0.83	0.96	0.98	1.61	2.09	1.65	1.65	1.73	1.16	0.98	1.31

[0192] The present exemplary embodiments of the method 1900 provide an online 4D-CT image estimation approach to patient-specific respiratory motion compensation. The method 1900 provides a motion estimation model that is trained in the template image using a number of 4D-CTs from different subjects. Then, the motion estimation model can be used to simulate serial CTs if a 3D image and the real-time tracked fiducial signals of a patient are given. Leave-one-out validation results from thirty 4D-CT exemplary experimental

data showed that an average prediction error of the lung field surface is 1.63 mm. All of the exemplary experimental results of the method 1900 were unexpected results.

[0193] In an exemplary embodiment, one or more aspects of the methods 500, 600, 1300, 1400, and 1900 may be used to correction for motion in any sequence of images.

[0194] In an exemplary embodiment, one or more aspects of the methods 500, 600, 1300, 1400, and 1900 may be combined, in whole or in part, with one or more other aspects of the methods 500, 600, 1300, 1400, and 1900.

[0195] Referring now to FIG. 26A and FIG. 26B, an exemplary embodiment of a CARS microscopy system 2600 includes a light source including a broadly-tunable ps OPO 2602 that includes a periodically-poled KTiOPO<sub>4</sub> crystal, commercially available from Levante, APE (Berlin, Germany) The OPO 2602 is pumped by the second harmonic (532 nm) output of a mode-locked Nd:YVO<sub>4</sub> laser 2604, commercially available from High-Q Laser (Hohenems, Austria). The laser 2604 delivers a 7-ps, 76-MHz pulse train at both 532 nm and 1064 nm. The 1064-nm pulse train is used as the Stokes wave. The 5-ps OPO signal is used as the pump wave with a tunable wavelength ranging from 670 nm to 980 nm. The beating frequency between the pump and Stokes beams covers the entire, chemically-important, vibrational-frequency range of 100-3700 cm<sup>-1</sup>. The pump and Stokes beams are overlapped by a time-delay line 2606 and dichroic mirror 2608, in both temporal and spatial domains to satisfy the precondition for producing a CARS signal, and then they are conveyed through an objective lens 2610 into and through an optical fiber 2612, another objective lens 2614 and a long-pass filter 2616.

[0196] In an exemplary experimental embodiment of the system 2600, the narrow-bandwidth pump and Stokes pulses (~3.5 cm<sup>-1</sup>) with durations of 5 ps were able to effectively reduce the non-resonant CARS background, and thus ensured a high signal-to-background ratio as well as a sufficient spectral resolution. This was an unexpected result. Meanwhile, the light source also provided excellent power stability, allowing high-sensitivity ultrafast imaging.

[0197] In the system 2600, the pump and Stokes beams then pass into and through a microscope assembly 2618. In an exemplary embodiment, the microscopy assembly 2618 is modified from a confocal laser scanning microscope (Fluo-View® FV300, Olympus Optical Co. Ltd., Tokyo, Japan). The modified microscopy subsystem has three PMT detection channels, PMT1, PMT2 and PMT3. The PMT detection channels are able to detect backward (Epi) CARS signals, PMT1, forward CARS signals, PMT2, and Rayleigh scatter-

ing transmission signals, PMT3, which was used as a reference.

**[0198]** In an exemplary experimental embodiment of the system **2600**, the pump and Stokes beams were coupled into the fiber **2612** using a 10× (NA=0.25, Newport) microscopy objective **2610** and then collimated using another 10× objective **2614**. In an exemplary experimental embodiment of the system **2600**, a dichroic mirror, DM2, used in the microscope assembly **2618** was 770dxcr, commercially available from Chroma Technology Corp. In an exemplary experimental embodiment of the system **2600**, the bandpass filters, F1 and F2, positioned upstream from PMT1 and PMT2, respectively, were hq660/40m-2p optical filters, commercially available from Chroma Technology Corp. In an exemplary experimental embodiment of the system **2600**, an objective lens **2618a** was used in the microscope assembly that was a 1.2-NA water immersion objective lens (60×, IR UPlanApo, Olympus, Melville, N.J.) was used, yielding a CARS resolution of ~0.4 μm in the lateral plane, and ~0.9 μm in the axial direction.

**[0199]** In an exemplary experimental embodiment of the system **2600**, the optical fiber **2612** was a standard Corning SMF28 communication fiber. The SMF28 communication fiber worked as an MMF below its cutoff wavelength of ~1260 nm, and covered the CARS operating wavelength range (i.e., from 500 nm to 1100 nm). The SMF28 communication fiber had a core diameter of ~9.2 μm and a NA of 0.14. Because the V-parameter of the SMF28 communication fiber was ~4.34 for 817 nm (pump) and ~3.33 for 1064 nm (Stokes), there were approximately 9 core modes for 817 nm and 6 core modes for 1064 nm based on calculated results from an estimation equation ( $N \approx V^2/2$ ). In an exemplary experimental embodiment of the system **2600**, the coupling efficiency was about 72% for the pump (817 nm) and 64% for the Stokes (1064 nm), which were coupled into the SMF28 communication fiber using a 10× objective. In an exemplary experimental embodiment of the system **2600**, the autocorrelator used to measure auto/cross-correlation function curves was an autocorrelator for a Levante Emerald® OPO (A-P-E Angewandte Physik & Elektronik GmbH; Berlin, Germany). In an exemplary experimental embodiment of the system **2600**, the optical spectrometer used to measure the optical spectra was an Agilent 86142B® optical spectrum analyzer (Agilent Technologies, Inc.; Santa Clara, Calif., USA) or an HR4000™ high-resolution spectrometer (Ocean Optics, Inc.; Dunedin, Fla., USA).

**[0200]** In an exemplary experimental embodiment of the system **2600**, we analyzed the fiber design using several parameters: dispersion length  $L_D$  (length over which the duration of a pulse width is broadened by  $\sqrt{2}$ ), walk-off length  $L_W$  (length over which two pulses at two different wavelengths are separated in time by one pulse duration), nonlinear length  $L_{NL}$  (length over which the SPM-induced phase shift of a pulse equals  $2\pi$ ), and average threshold power,  $P_{2\pi}$ , for SPM (power at which the SPM-induced phase shift of a pulse equals  $2\pi$ , and it can be derived from  $L_{NL}$ ). In an exemplary experimental embodiment of the system **2600**, we considered only step-index fibers for simplicity. These parameters were estimated using Equations (21a) to (21d) as follows:

$$L_D = \left( -\frac{2\pi c}{\lambda^2} \right) \left( \frac{t_p^2}{D} \right), \quad (21a)$$

-continued

$$L_W = \frac{t_p}{v_g^{-1}(\lambda_1) - v_g^{-1}(\lambda_2)}, \quad (21b)$$

$$L_{NL} = \frac{\pi D_{eff}^2 \lambda f_{pTP}}{4n_2 P_{ave}}, \quad (21c)$$

$$P_{2\pi} = \frac{\pi \lambda f_{pTP} D_{eff}^2}{4n_2 L}, \quad (21d)$$

**[0201]** where  $t_p$  was the pulse width,  $\beta$  was the dispersion of the fiber waveguide,  $c$  was the speed of light,  $\lambda$  was the central wavelength of the pulse,  $v_g$  was the group velocity of the fiber mode [ $v_g = c/(n - 1.4n/dA)$ ],  $n$  is effective index of fiber modes,  $n_2$  was the nonlinear refractive index of the fiber material [ $n_2 = 2.6 \times 10^{-16} \text{ cm}^2/\text{W}$  for silica,  $P_{ave}$  was the average power of the pulse in the fiber,  $D_{eff}$  was the effective mode diameter, and  $f_p$  was the repetition rate of the laser (76 MHz in our study).

**[0202]** In an exemplary experimental embodiment of the system **2600**, the pump and Stokes wavelengths were tuned to 817 nm and 1064 nm, respectively, resulting in a 2845  $\text{cm}^{-1}$  Stokes shift, which matched with the Stokes shift of the  $\text{CH}_2$  stretch vibration in lipids.

**[0203]** In an exemplary experimental embodiment of the system **2600**, one concern in the design of a fiber delivery system was the broadening of pulse width due to dispersion from the fiber. Pulse broadening leads to a lower effective peak power and would decrease the excitation efficiency of CARS. Although, a pre-chirp unit or a piece of dispersion compensation fiber can be used to compensate for dispersion, the wavelength-dependence of dispersion still makes it complicated to achieve the optimal design of a compensation unit. In CARS imaging systems, the typical wavelength of interest ranges from 500 nm to 1100 nm, covering wavelengths from the anti-Stokes wave to the Stokes wave. The typical pulse width of interest ranges from 10 fs to 10 ps.

**[0204]** FIG. 27A shows calculated  $L_D$  as a function of wavelength (black curve,  $t_p = 5$  ps) and pulse width (red curve,  $\lambda = 817$  nm) in the typical ranges using Equation (21a), respectively.  $D$  was calculated using an equation in the datasheet of the Corning SMF28 Optical Fibers [ $D = S_o/4(\lambda - \lambda_o^4/\lambda^3)$ ], zero dispersion slope  $S_o = 0.086 \text{ ps}/(\text{nm}^2\text{km})$ , zero dispersion wavelength  $\lambda_o = 1310 \text{ nm}$ . Since the equation in the datasheet of the Corning SMF28 Optical Fibers only covered the intramodal chromatic dispersion (material dispersion and waveguide dispersion) of the fiber but not intermodal dispersion, the intermodal dispersion was simulated using a conventional form of Sellmeier's equation and the step-index fiber model. It was noticed that  $L_D$  increased nonlinearly with wavelength or pulse width. At  $t_p = 5$  ps, the shortest  $L_D$  was about 11.2 meters at 500 nm, which was much longer than the physical fiber length needed for a fiber delivery system. Hence, the dispersion issue was negligible in the exemplary experimental embodiment of the system **2600**. Meanwhile,  $L_D$  was about 1 meter for  $t_p = 1.08$  ps at  $\lambda = 817$  nm. This result suggested that the dispersion was not an issue when the pulse width was longer than one picosecond for the SMF28 communication fiber.

**[0205]** In an exemplary experimental embodiment of the system **2600**, to calculate the walk-off length  $L_W$ , a conventional form of Sellmeier's equation was employed to simulate the refractive index of the fiber core and the fiber cladding with 1% index difference.  $L_W$  is defined the extra time delay

needed to add to the pump or the Stokes waves to keep their temporal overlapping and to generate CARS signals. Possible shortest and longest  $L_w$ , induced by the group velocity difference between the pump and the Stokes waves were estimated as well. Because the effective indices of fiber modes is lower than the core index and higher than the cladding index regardless of SMFs or MMFs, the core and cladding index could be used to estimate the largest and smallest effective index of the fiber modes. In addition, because the wavelengths of interest were in the normal dispersion region (group index decreases as wavelength increases), the group velocity  $v_g$  of the fiber mode increased with wavelength. Since the Stokes wavelength is longer than the pump wavelength,  $v_g$  of the Stokes wave was greater than that of the pump wave. Therefore, when  $v_g$  of the Stokes and pump waves reached their own maximum and minimum respectively, the largest group velocity difference would be obtained and would result in the shortest  $L_w$ . Based on our experimental simulations of the system **2600**, when the core and cladding indices were used as the effective indices of the pump wave and Stokes wave separately, we could reach the largest group velocity difference between the pump and Stokes waves for MMFs and thus the shortest  $L_w$ . On the other hand, SMFs possessed the longest  $L_w$  because there was only a fundamental mode in the fiber and no intermodal dispersions. Based on our simulations of the system **2600**, the cladding index was used as the effective index of the fundamental mode to reach the longest  $L_w$ . The shortest and longest  $L_w$  were calculated as a function of Raman shift with respect to the Stokes wave, which was assumed to be 1064 nm with  $\Delta\nu=8$  ps (for comparison to experimental results).

**[0206]** FIG. 27B shows exemplary simulated results of the system **2600** using Equation (21b), where the x-axis Raman shift wave number was limited to  $4000\text{ cm}^{-1}$ . In addition,  $L_w$  was only plotted up to 3 meter to cover practical fiber delivery interest. It was noted that  $L_w$  decreased as Raman shift increased, and SMFs provided a much larger  $L_w$  than MMFs, especially for Raman shifts within  $1200\text{ cm}^{-1}$ . For practical SMFs and MMFs,  $L_w$  fell in the region between the shortest  $L_w$  curve and the longest  $L_w$  curve. Compared to the single  $L_w$  curve of SMFs,  $L_w$  of MMFs existed as an area between the two curves due to cross-calculations of  $L_w$  between different modes. Hence, MMFs had a larger delay adjustment range than SMFs to obtain the optimal temporal overlapping of pump and Stokes waves (i.e., SMFs had an optimal delay adjustment point, while MMF may have an optimal delay adjustment range instead). This effect was confirmed in our experiments with the system **2600** using SMF and MMF. To increase  $L_w$ , laser pulses with larger  $t_p$  can be used since  $L_w$  is linearly proportional to  $t_p$ . Conversely,  $L_w$  will be much shorter when fs laser pulses are used for CARS imaging. Additionally, because the core index (i.e., upper limit of effective index) and the cladding index (i.e., lower limit of effective index) were used as the largest and smallest effective index of fiber modes in our simulations, the shortest  $L_w$  presented in FIG. 27B reached the limiting point for MMF and thus was independent of the number of modes propagating in MMF.

**[0207]** In an exemplary experimental embodiment of the system **2600**, for fiber delivery of ultrafast laser pulses, nonlinear effects (e.g., SPM and FWM) are critical issues, which could either reshape the spectra of laser pulses or generate new laser frequencies. To address these concerns, we estimated SPM induced nonlinear length  $L_{NL}$  and average thresh-

old power  $P_{2\pi}$  that were induced by SPM in this section. The FWM effect was also investigated in our experiments due to the complicity and significance to estimate FWM originated from interactions between different core modes in MMF. In our calculations, we estimated  $L_{NL}$  as a function of the mode diameter using Equation (21c), assuming  $f_p$  was 76 MHz,  $t_p$  was 5 ps when  $\lambda$  was 817 nm and  $t_p$  was 10 ps when  $\lambda$  was 1064 nm. The solid and the dashed curves in FIG. 27C represent different  $L_{NL}$  when  $P_{ave}=20$  mW and  $P_{ave}=100$  mW, respectively. We noted that  $L_{NL}$  increased with the mode diameter quadratically, indicating that the SPM effect would be greatly reduced with the increase of the mode diameter.  $L_{NL}$  for  $P_{ave}=20$  mW was five times larger than that for  $P_{ave}=100$  mW. In exemplary experimental embodiments of the system **2600**, when the mode diameter was  $\sim 9\text{ }\mu\text{m}$ ,  $L_{NL}$  for 817 nm at  $P_{ave}=20$  mW and  $P_{ave}=100$  mW equaled about 45 meters and 9 meters;  $L_{NL}$  for 1064 nm at  $P_{ave}=20$  mW and  $P_{ave}=100$  mW equaled about 100 meters and 20 meters. Additionally, we estimated the average threshold power,  $P_{2\pi}$ , as a function of the mode diameter using Equation (21d), assuming fiber length equaled to 1 meter,  $f_p$  was 76 MHz,  $t_p$  was 5 ps when  $\lambda$  was 817 nm and  $t_p$  was 10 ps when  $\lambda$  was 1064 nm. The exemplary experimental results for the system **2600** are plotted in FIG. 27C. Similar to  $L_{NL}$ , we noted that  $P_{2\pi}$  increased quadratically with the mode diameter. In FIG. 27A, FIG. 27B and FIG. 27C, both  $L_{NL}$  and  $P_{2\pi}$  for 1064 nm are larger than those for 817 nm, which was predicted by Equations (21c) and (21d).

**[0208]** In an exemplary experimental embodiment of the system **2600**, we examined the dispersion-induced broadening of the pulse width using SMF28 communication fiber, whose core diameter was  $9.2\text{ }\mu\text{m}$ , and cladding diameter was  $125\text{ }\mu\text{m}$ . We measured the autocorrelation function curves of the pump (817 nm, 50 mW) and the Stokes (1064 nm, 50 mW) waves at two different conditions: (1) direct output from the OPO or laser and (2) after passing through a 2-meter SMF28 communication fiber. The normalized autocorrelation curves were shown in FIG. 28A. By measuring the FWHM bandwidth of the curves, we calculated the percentage of pulse broadening per meter: 7.2% per meter for 817 nm and 3.8% per meter for 1064 nm. Based on the experimental results shown in FIG. 28A ( $L_D=21.07$  m for 817 nm,  $L_D=41.24$  m for 1064 nm), the calculated percentage of pulse broadening was 6.7% per meter for 817 nm and 3.4% per meter for 1064 nm, which were about 6.9% and 10% smaller than the measured ones. This discrepancy could be caused by the step-index fiber model used in simulations, which utilized weakly-guiding and scalar mode approximations. In addition, the discrepancy could also arise from measurement errors, as well as possible difference between the real fiber parameters and those used in simulations. In spite of this discrepancy, the broadening effect of the pulses was still negligible by using MMFs for the fiber delivery in CARS imaging.

**[0209]** In an exemplary experimental embodiment of the system **2600**, we examined the walk-off length  $LW$  by measuring the cross-correlation function curves before and after passing through a 2-meter SMF28 communication fiber. A strong Gaussian-shape single peak of cross-correlation function curve indicated that the pump (817 nm) and the Stokes (1064 nm) waves achieved a good overlapping in time without any walk-off; otherwise there would be small shoulders. After the two waves passed the 2-meter length of the SMF28 communication fiber, we adjusted the translation stage of the delay line to obtain the strongest Gaussian-shape single peak

again. Then, we calculated the adjustment amount of the translation stage of the delay line. This amount value corresponded to the walk-off induced delay in distance by the SMF28 communication fiber. The normalized cross-correlation intensity curves (before and after passing through a 2-meter SMF28) are shown in FIG. 28B. Adjustment for the 2-meter length of the SMF28 communication fiber was 1.607 mm or 53.56 ps (26.78 ps/meter). Because the measured FWHM pulse width of 817 nm and 1064 nm pulses were 5.647 ps and 10.47 ps, we took the average ( $\sim 8$  ps) of the pulse width to calculate the measured  $L_w$ . Then, the measured  $L_w$  was 0.2987 meters for 8-ps pulse and 2-meter SMF28. Based on our simulated  $L_w$  in FIG. 28B, the simulated shortest  $L_w$  for MMF, which was 0.2578 meters for 2845  $\text{cm}^{-1}$  Raman shift, corresponding to the pump (817 nm) and Stokes (1064 nm) waves. Therefore, our measured  $L_w$  result was longer than the simulated shortest  $L_w$ , which fell in the region between the simulated longest  $L_w$  and the simulated shortest  $L_w$  shown in FIG. 28B.

**[0210]** In an exemplary experimental embodiment of the system 2600, we examined the SPM effect induced by the pump (817 nm) and Stokes (1064 nm) waves propagating in a 1-meter length of the SMF28 communication fiber. Within the power range from 0 to 200 mW used in our experiments, we did not observe the cross-phase modulation (XPM) effect (i.e., no spectral change) when both the pump and Stokes waves propagated in the fiber simultaneously. Hence, we measured the spectrum with either the pump or Stokes wave propagating in the fiber separately. FIG. 29A, FIG. 29B and FIG. 29C illustrate normalized measured pump (817 nm) and Stokes (1064 nm) wave spectra as a function of propagating power in SMF28 communication fiber. We noted that there were some ripples in spectra of pump (817 nm) waves. The ripples in spectra of pump waves originated from the artifact effect of the second-order grating inside the grating-based Agilent OSA, which was confirmed by changing the grating option in the OSA configuration and the technical supporting staff of the Agilent Corp. Another artifact effect of the grating-based Agilent OSA was that when the input  $\lambda$ ,  $< 850$  nm, the OSA display showed both X and 2X, which was described in Agilent OSA application notes, and it is important for FWM measurements. In FIG. 29A, we noted that FWHM bandwidth of pump waves increased with power. At 200 mW, the FWHM bandwidth broadened by  $\sim 36.8\%$ , but it was still far from FIG. 27C phase shifts (peak splitting in central wavelength). The power of 200 mW exceeded the average power (i.e., less than tens of milliwatts) usually applied in CARS microscopy. In FIG. 29B, we noted that FWHM bandwidth of Stokes waves also increased with power. At 200 mW, FWHM bandwidth broadened by  $\sim 31.3\%$ , which was far from FIG. 27C phase shifts as well. The exemplary experimental results illustrated in FIG. 29A, FIG. 29B and FIG. 29C indicated that the 1-meter SMF28 communication fiber can be used to deliver individual pump or Stokes waves without generating serious SPM-induced phase shifts. This was an unexpected result.

**[0211]** In an exemplary experimental embodiment of the system 2600, we examined the FWM effect induced by the pump (817 nm) and Stokes (1064 nm) waves simultaneously propagating in a 1-meter long SMF28 communication fiber. We found weak anti-Stokes generations at 663 nm, which matched the 2845  $\text{cm}^{-1}$  anti-Stokes shift of the  $\text{CH}_2$  stretch vibration. Therefore, it would result in spurious CARS signals and background noise in the imaging system. The zero-

dispersion wavelength of fibers plays an important role in the FWM behavior. For SMF, the FWM phase-matching condition is difficult to be met for the frequency components shifted by more than 3000  $\text{cm}^{-1}$  from zero dispersion wavelength of the fiber. However, for MMF, the FWM phase-matching condition is relaxed by the easiness of satisfying the phase-matching condition with pump, Stokes and anti-Stokes waves, which propagate in different modes. For instance, the anti-Stokes wave at the fiber mode LP21 can be generated by the combination of the pump (LP01), the pump (LP02) and the Stokes (LP1). As a result, more fiber modes exist in the fiber, more diverse mode combinations will exist to satisfy the FWM phase-matching condition, generating stronger FWM signals. Thus, MMF is more likely to satisfy the phase-matching condition to generate the FWM signals than SMF. In our exemplary experimental embodiments of the system 2600, although the anti-Stokes (663 nm,  $-7450 \text{ cm}^{-1}$ ) wavelength was far away from the zero dispersion wavelength of the SMF28 (i.e., 1310 nm), SMF28 communication fiber can still easily satisfy the FWM phase-matching condition because there were approximately 9 fiber modes for 817 nm and 6 fiber modes for 1064 nm existing in SMF28. FIG. 29C shows a typical normalized measured FWM (663 nm) wave spectrum output from a 1-meter long SMF28. In our exemplary experimental embodiments of the system 2600, a clear peak was observed at 663 nm, while no other new peaks occurred when the pump (817 nm) and Stokes (1064 nm) waves propagated in SMF28 simultaneously. We also noted that anti-Stokes signals (663 nm) was quadratically proportional to the input power of the pump (817 nm), and linearly proportional to the power of the Stokes (1064 nm). In an exemplary experimental embodiment of the system 2600, the FWM signal was measured using an optical spectrometer (HR4000™; Ocean Optics, Inc.), which provided better sensitivity than Agilent OSA in the range of visible wavelengths.

**[0212]** In an exemplary experimental embodiment of the system 2600, we verified the FWM effect by, instead of inserting the 1-meter SMF28 communication fiber 2612 before the entrance of the microscopy assembly 2618, we mounted it directly under the 10 $\times$  (NA=0.25, Newport) objective and captured the backward FWM (or non-resonant-CARS) images from the proximal end of the fiber 2612. The epi-CARS channel was used with a bandpass filter (hq660/40m-2p, Chroma Technology Corp., Bellows Falls, Vt., USA). Powers of the pump and the Stokes at the proximal end of MMF were 200 mW and 100 mW, respectively. FIG. 30A, FIG. 30B, FIG. 30C, FIG. 30D, FIG. 30E and FIG. 30F show a bright-field image of the well-cleaved proximal end of a 1-meter SMF28 and five CARS images from the proximal end of the 1-meter SMF28 communication fiber at various conditions, such as pump-plus-Stokes, pump-only, distal end suspended in air or immersed in water/oil, and well-cleaved or bad-cleaved distal end. We observed strong FWM signals emerging from the fiber core when the pump (817 nm) and Stokes (1064 nm) waves were coupled simultaneously into the SMF28 fiber as shown in FIG. 30B. The circular pattern of the FWM signals indicated the mode distribution in the core of the SMF28 communication fiber was not uniform. No FWM signal was detected when only the pump wave (817 nm) was coupled into the SMF28 as shown in FIG. 30C. There were weak FWM signals when the well-cleaved distal end of the SMF28 fiber was immersed in water, as illustrated in FIG. 30D, or oil, as illustrated in FIG. 30E, or when the distal end was bad-cleaved/cut, as illustrated in FIG. 30F.

Collectively, these findings suggested that the FWM signals were mainly generated in the forward direction.

**[0213]** In an exemplary experimental embodiment of the system **2600**, we tested the SMF28 communication fiber to deliver ps lasers for CARS imaging. Emerging from the dichroic mirror (DM1), the pump (817 nm) and Stokes (1064 nm) waves were coupled into a 1-meter long SMF28 communication fiber by a 10× Newport objective. After passing the fiber, the two waves were then collimated by another 20× Newport objective. A 750-nm long-pass filter (FEL0750, Thorlabs, Inc., Newton, N.J., USA) was used to eliminate the FWM (663-nm) signals generated in the SMF28 before the microscopy assembly **2618**. The pump and the Stokes waves were tuned to 40 mW and 20 mW for CARS imaging. We characterized the performance of the setup by imaging calibrated 10 μm polystyrene beads (PEB), which generated strong resonant CARS signals at the aliphatic symmetric CH<sub>2</sub> stretch ( $\Delta\omega=2845\text{ cm}^{-1}$ ). FIG. 31A and FIG. 31B show the forward- and epi-CARS images of 10 μm PEB spin-coated on a glass slide by delivering ps lasers through a 1-meter SMF28 communication fiber. The CARS images were verified by the results of a single pump wave taken at 2845 cm<sup>-1</sup>. In FIG. 31B, the epi-CARS image clearly showed the characteristic ring structure of PEBs due to the relative large size of PEBs compared to the small coherence length of epi-CARS signals. In terms of the CARS image quality, such as contrast and resolution, no clear difference was noticed between using free-space and using a 1-meter SMF28 communication fiber for delivery of the laser.

**[0214]** To further assess the performance of delivering ps lasers through the SMF28 communication fiber, we imaged two types of mouse tissues *ex vivo*. FIG. 31C and FIG. 31D show the epi-CARS images of the mouse kidney and ear, respectively. There were no discernible degradations with regard to the image quality obtained through fiber delivery compared to free-space delivery. In addition, we tested the stability of this SMF28 fiber-delivered CARS system by characterizing fluctuations of the CARS signal while imaging PEBs. The fluctuations of the CARS signal were 1.5% and 4.6% for the short-term (i.e., one hour) and the long-term (i.e., two days), respectively. These results demonstrated that the SMF28 communication fiber can be used to deliver ps lasers for CARS imaging, and a filter can be used to block the FWM signals generated in the fiber. This was an unexpected result.

**[0215]** In an exemplary experimental embodiment of the system **2600**, we found that the dispersion of fibers is not an important issue for the design of a fiber delivery system. The reason is that the dispersion length of the fibers is much longer than the physical length of the fibers used for laser delivery in a CARS imaging system. Because of the group velocity difference between the pump and Stokes waves traveling in the fibers, the delay line needs a certain amount of adjustment to compensate for the walk-off length between the two beams. Based on our analyses on the nonlinear length and the average threshold power for SPM, it suggests that fibers with larger effective mode diameters can be used to decrease SPM-induced phase shifts of the laser pulses. There are FWM signals at the anti-Stokes frequency generated in the SMF28 communication fiber. These signals mainly propagate in the forward direction. A long-pass filter can be used to filter out the FWM signals to eliminate spurious CARS signals and background noise in the system. Thus, according to our exemplary experimental embodiment of the system **2600**, multimode SMF28 communication fibers can be used for delivery of

picosecond excitation lasers in a CARS imaging system without any degradation of the image quality. This was an unexpected result.

**[0216]** In an exemplary embodiment, one or more aspects of the systems **100**, **200**, **300**, and **400** and one or more aspects of the methods **500**, **600**, **1300**, **1400**, and **1900** may be combined, in whole or in part, with one or more other aspects of the system **2600**.

**[0217]** Referring now to FIG. 32, an exemplary embodiment of a CARS microscopy system **3200** includes an OPO laser **3202** (for providing a pump and Stokes beams) that is operably coupled to a dichroic mirror **3204**. The mirror **3204** is also operably coupled to an objective lens **3206** and an optical filter **3208**. In an exemplary embodiment, the optical filter **3208** is a long pass filter.

**[0218]** The objective lens **3206** is also operably coupled to an end of a single mode optical fiber **3210**. The other end of the fiber **3210** is operably coupled to an objective lens **3212**. The object lens **3212** is also operably coupled to a reflective surface of a MEMs mirror **3214** that may be actuated by a MEMs driver **3216**. The reflective surface of the MEMs mirror **3214** is also operably coupled to an objective lens **3218** that may be positioned proximate a tissue sample **3220**.

**[0219]** The optical filter **3208** is also operably coupled to a PMT **3222** that, in turn, is also operably coupled to a data acquisition system **3224**. The data acquisition system **3224** is also operably coupled to a computer **3226**.

**[0220]** In an exemplary embodiment, during operation of the system **3200**, the system operates substantially the same as one or more of the systems **100**, **200**, **300**, **400** and **2600** as described herein.

**[0221]** In an exemplary experimental embodiment of the system **3200**, the length of the lens **3212** was 40 mm, the NA of the lens **3212** was 0.25, the magnification of the lens **3212** was 10×, the distance between the end of the lens **3212** and the reflective surface of the MEMs mirror **3214** was 65 mm, the distance between the reflective surface of the MEMs mirror **3214** and an end of the lens **3218** was 51 mm, the length of the lens **3218** was 48 mm, the NA of the lens **3218** was 1.1, the magnification of the lens **3218** was 60×, the back aperture of the lens **3218** was 4.96 mm, the distance L1 was 51.24 mm, the laser radius before entering the lens **3218** was 2 mm, and the maximum scanning angle  $\Theta_{max}$  of the MEMs mirror **3214** during operation was 2.784 degrees.

**[0222]** In an exemplary experimental embodiment of the system **3200**, as illustrated in FIG. 33, the diffraction angle  $\Theta_d$  of the MEMs mirror **3214** during operation was determined to be 0.0117 degrees. As a result, the number of resolvable scanning angles was calculated as  $2\Theta_{max}/2\Theta_d=5.569$  degrees/0.0234 degrees=237. Thus, the maximum number of scanning steps in 2-D by the MEMs mirror **3214** was determined to be 237, which provided a maximum resolution of 237×237 pixels.

**[0223]** In an exemplary experimental embodiment of the system **3200**, as illustrated in FIG. 34, the linear scanning speed,  $v$ , of the MEMs mirror **3214** was calculated as equal to  $\omega r$ , where  $v$  is the tangential velocity of a point about the axis of rotation of the MEMs mirror,  $\omega$  is the angular speed of the MEMs mirror, and  $r$  is the radius of rotation. As a result of this calculation, it was observed that the operation of the MEMs mirror **3214** may, in an exemplary embodiment, be nonlinear and thus a nonlinear feedback control system may be used to monitor and control the operation of the MEMs mirror. Furthermore, in an exemplary experimental embodiment of the

system **3200**, the minimum linear scan step of the MEMs mirror **3214** was determined to be 0.021 mm.

[0224] In an exemplary experimental embodiment of the system **3200**, the effective NA for the lens **3218** was determined to be 0.4433.

[0225] In an exemplary experimental embodiment of the system **3200**, the resolution of the lens **3218** was determined to be 1124.

[0226] In an exemplary experimental embodiment of the system **3200**, the laser spot size provided by the lens **3218** was determined to be 2248 nm.

[0227] In an exemplary experimental embodiment of the system **3200**, as illustrated in FIG. 35, the signal to noise (“S/N”) of the system was determined by positioning a mirror **3502** immediately below the lens **3218**. In this manner, the strongest backward signal would be obtained, regardless of CARS or other optical modalities, which would provide the best S/N ratio obtainable by the exemplary experimental embodiment. In the exemplary experimental embodiment of the system **3200**, the S/N ratio observed was 3.5.

[0228] Thus, in an exemplary embodiment of the system **3200**, the resolution of the laser beam output of the lens **3218** was 1124 nm, the laser spot size provided by the lens **3218** was 2248 nm, the maximal scan angle  $\Theta_{max}$  of the MEMs mirror **3214** was equal to 2.784 degrees, the number of scanning steps per image was 237, the maximum number of pixels within an image was 237×237, the maximal linear scan speed difference at the back aperture of the lens **3218** was  $\omega \times 240$  pm, and the minimum linear scan step at the back aperture of the lens **3218** was about 21 pm.

[0229] Furthermore, in an exemplary embodiment of the system **3200**, the maximum field of view provided by the lens **3218** is 233×233  $\mu\text{m}^2$ ; speed of scanning of 0.496 second/scan line; full scanned image with 237×237 pixels in about 120 second; maximum scan angle  $\Theta_{max}$  of 2.784 degrees; the objective lens **3218** is an Olympus LUMFL60XW, near infra-red objective lens, FN of 14, NA of 1.1 and WD of 1.5 mm; and number of pixels per image of 237×237.

[0230] In an exemplary embodiment, one or more aspects of the systems **100**, **200**, **300**, **400** and **2600** and one or more aspects of the methods **500**, **600**, **1300**, **1400**, and **1900** may be combined, in whole or in part, with one or more other aspects of the system **3200**.

[0231] Referring now to FIG. 36 and FIG. 37, an exemplary embodiment of a MIMIG molecular imaging system **3600** for patient treatment and diagnosis includes a conventional CT scanner **3602**, an electromagnetic (“EM”) tracking system **3604**, a radiofrequency (“RF”) introducer needle **3606**, a microendoscopy imaging system **3608**, an RF ablation (“RFA”) system **3610**, and a computer workstation **3612** that may be operably coupled to the CT scanner, the EM tracking system, the RF introducer needle, the microendoscopy imaging system, and the RFA system.

[0232] In an exemplary embodiment, the EM tracking system **3604** may be a conventional EM tracking system such as, for example, an electromagnetic tracking system (Aurora® EM Tracking; NDI, Waterloo, ON, Canada).

[0233] In an exemplary embodiment, the RF introducer needle **3606** and the RFA system **3610** may be a conventional RF introducer needle and RFA system such as, for example, a Valleylab Cool-tip™ RFA system (Covidien, Mansfield, Mass., USA).

[0234] In an exemplary embodiment, the microendoscopy imaging system **3608** may be a conventional microendoscopy

system, a conventional CARS microendoscopy system, and/or may include one or more aspects of the systems **100**, **200**, **300**, **2600** and **3200** and/or the methods **500**, **600**, **1300**, **1400**, and **1900**.

[0235] In an exemplary embodiment, the computer workstation **3612** is operably coupled to the CT scanner **3602**, the EM tracking system **3604**, the RF introducer needle **3606**, the microendoscopy imaging system **2608**, and the RFA system **3610** for monitoring and controlling the operation of each.

[0236] In an exemplary embodiment, the system **3600** implements a method **3800** of diagnosing and treating a patient in which, in **3802**, the system determines if a lesion has been detected by the CT scanner **3602**.

[0237] If the system **3600** determines that the CT scanner **3602** has detected a lesion, then, in **3804**, the system determines if the size of the lesion is greater than or equal to 1.5 cm in diameter or less than 1.5 cm in diameter. If the system **3600**, in **3804**, determines that the lesion is greater than or equal to 1.5 cm in diameter, then a normal treatment procedure is performed on the patient.

[0238] Alternatively, if the system **3600**, in **3804**, determines that the lesion is less than 1.5 cm in diameter, then a contrast agent is injected into the patient in a conventional manner **3808**. In an exemplary embodiment, the contrast agent is an IntegriSense™680 (Perkin Elmer, Inc., Boston, Mass., USA) fluorescent contrast agent used to label  $\alpha_v\beta_3$  integrin expressed in malignant cancer cells.

[0239] In an exemplary embodiment, in **3808**, contrast enhancement agents are used to label tumor regions. These contrast enhancement agents include the FDA-approved, indocyanine green (ICG), as well as molecular imaging dyes targeting specific pathways. In an exemplary embodiment, in **3808**, integrin dye can be used to label lung cancer tissue and may be detected using fiber-optic microendoscopy using one or more of the methods of the present exemplary embodiments. In an exemplary embodiment, in **3808**, using other molecular imaging contrast agents for targeting specific molecular pathways, the fiber-optic molecular imaging guided tumor detection and diagnosis methods of the present exemplary embodiments may provide more diagnostic power and could potentially eliminate the need for a biopsy.

[0240] In an exemplary embodiment, the system **3600** then, in **3810** provides an image guided diagnosis, by operating the RF introducer needle **3606** and the microendoscopy imaging system **3608** to provide an image guide diagnosis. In an exemplary embodiment, the system **3608** provides an image guide diagnosis by processing the CARS signals generated by operation of the system to provide specific spectral features of the molecules scanned thereby to identify the lesion as being malignant cancer and/or differentiate the lesion from known healthy tissue as a proxy for malignant cancer. The specific spectral features and spectral differentiator metric associated with a known malignant lesion by itself and/or versus healthy normal tissue may be developed through analyzing empirical clinical data.

[0241] If the microendoscopy imaging system **3608** determines that the lesion is malignant cancer in **3812**, then, in **3814**, the RFA system **3610** is operated to ablate the lesion. Alternatively, if the microendoscopy imaging system **3608** does not determine that the lesion is malignant cancer in **3812**, then, in **3816**, the system **3600** continues in **3810** using image-guided diagnosis.

[0242] In an exemplary embodiment, during operation, as illustrated in FIG. 39A, FIG. 39B, FIG. 39C, and FIG. 39D,

the system **3600** implements a method **3900** of operation in which, in **3902**, the system provides a pre-procedural CT scan **3902a** of the patient.

[0243] In an exemplary embodiment, the system **3600** then, in **3904**, provides segmentation of the pre-procedural CT scans to provide better visualization of anatomical features such as, for example, pulmonary vessels, airways, as well as nodules to aid in surgical planning. In an exemplary embodiment, the segmentation of **3904** may be conventional and/or include one or more aspects of the exemplary embodiments herein.

[0244] In an exemplary embodiment, in **3904**, the system **3600** performs region-growing-based lung field segmentation and vascular-oriented blood vessel segmentation on the CT images. In an exemplary embodiment, the lung field segmentation extracts cavity and lung fields, and the vessel segmentation matches vascular structures from medical images.

[0245] In **3906**, the system **3600** then provides registered CT images **3906a** of the patient and fuses the patient data, which may include CT scans as well as other visual and diagnostic data, into a common and user interactive database.

[0246] In an exemplary embodiment, in **3906**, the system **3600** provides deformable registration of lung parenchyma: A joint segmentation and registration algorithm aligns serial images of the same patient. No particular assumption regarding the temporal pathological changes is used in the longitudinal deformation model. In an exemplary embodiment, the registration of **3906** may be conventional and/or include one or more aspects of the exemplary embodiments herein.

[0247] In **3908**, the system **3600** then provides real time visualization, via one or more user interfaces **3908a**, of the operational steps of the method **3900**. In this manner, the method **3900** provides: a) an image guided pre-procedural image database to facilitate procedure diagnosis and planning; and b) during the treatment process, provides a real-time visualization of the operational steps of the method **3900**. Furthermore, in **3908**, the system **3600** may detect the interventional probe by EM tracking and visualize via CT imaging in real time. Motion compensation models, such as the exemplary embodiments of the motion compensation methods herein, may be used for simulation of real-time CT images during intervention based on the signals from respiratory belting and EM-tracking of fiducial markers. After successfully targeting the lesion, fiber-optic microendoscopic imaging is then used for further confirmation to verify that the probe tip is inside the tumor of interest through microendoscopy and FNAB is then performed to diagnose malignant tumor. RFA treatment can be applied onsite for treatment.

[0248] In an exemplary embodiment, in **3908**, the system **3600** provides an oblique view interface, including automatic alignment between the physicians orientation and standing position and the display of the images, so that physicians can easily steer the interventional probe, including one or more of the needle **3606**, the fiber probe system **126**, and the fiber probe **402**, by referring to the image visualization during intervention.

[0249] In an exemplary embodiment, as illustrated in FIG. **39D**, in one or more of **3902**, **3904**, **3906** and **3908**, the system **3600** may implement a respiratory motion correction method, that may also include one or more aspects of the method **1900**, that utilizes longitudinal 4D-CT from a number of samples to construct the respiratory patterns, and correlates this pattern with the specific CT images and the real time tracking data

from a patient such as fiducials attached on the patient's chest, as well as the respiratory belt signals. CT images during intervention are then estimated based on the correlation model and the real time signals.

[0250] In exemplary experimental embodiments of the system **3600** and methods **3800** and **3900**, lung tumor models were created using females white New Zealand rabbits. The rabbits had weights of  $2.2 \text{ kg} \pm 200 \text{ g}$ . The initial VX2 tumor cell line was provided by the Department of Comparative Medicine at M.D. Anderson Cancer Center (Houston, Tex.). In order to propagate the VX2 tumor cell line, a tumor cell suspension was first inoculated in the limb of one rabbit and a tumor with a diameter of around 20 mm was noticeable after two weeks. From this tumor two cell suspensions were prepared, one for limb inoculation and the other one for lung inoculation. For this procedure, the rabbits were anesthetized with general anesthesia and the hair of the thoracic was shaved completely. The lung inoculation was performed under fluoroscopy guidance. Once a region of the lung of a rabbit was selected, an 18-Ga Chiba needle was introduced into the chest of the rabbit. In order to simulate a peripheral lung tumor, the needle was placed at the base of the right lung of the rabbit and the depth of the needle was continuously assessed with different fluoroscopy views of the C-arm at 0, 45 and 90 degrees. Once the needle was in the desired location and at an adequate depth, the VX2 cell suspension was injected into the rabbit. Five minutes later, new fluoroscopic images of the chest of the rabbit were taken for pneumothorax assessment. No rabbit developed pneumothorax in our experiments. The VX2 tumor size was assessed with weekly CT until a desired size of ~15 mm was attained.

[0251] On the day of the operation of the exemplary experimental embodiments of the system **3600** and methods **3800** and **3900**, the rabbit was anesthetized with general anesthesia and taken to the CT facility. A pre-procedural CT scan with breath holding was performed using the CT scanner **3602**. The CT data was then transferred to the workstation **3612** of the system **3600**. The pre-procedural CT scan was used for image segmentation, tumor identification and surgical planning. After placing five or six active fiducials near the chest of rabbit, the coordinates of the fiducials in the EM-tracking space and the CT image space were registered using affine transformation by the workstation **3612**. During intervention, real-time tracking data, including the location and orientation of the intervention devices, were precisely measured by EM sensors of the EM tracking system **3604** and mapped onto the CT image space in real-time.

[0252] As illustrated in FIG. **40**, during the exemplary experimental embodiments of the system **3600** and methods **3800** and **3900**, using the CT scanner **3602**, a user interface **4000** was provided on the workstation **3612** that indicated a target point was selected as the center of the tumor and the entry point indicated the location for puncturing the needle. For the surgical planning of the method **3800**, the pre-procedural CT volume was segmented using lung volume segmentation, as described herein, and the lung lesions were labeled and visualized in both volumetric and surface meshes. The surgical planning interface **4000** further provided the operator of the workstation **3612** an interactive method for creating a path for the needle insertion. The orthogonal viewer **4000** displayed on the workstation **3612**, including a simultaneous axial, sagittal, and coronal view, provided a clear perspective about the depth and direction of the needle that was used for reaching the tumor. Before puncturing the needle, we con-

firmed the needle tracking accuracy, and location at the point of entry and ensured the line traced between the point of entry, skin, and the target, tumor, was planned according to the orthogonal viewer. A small 3-mm incision was made at the skin level for the needle. Before the puncture, the breathing of the animal was held thereby avoiding any movement from the chest.

[0253] As illustrated in FIG. 40 and FIG. 41, during the exemplary experimental embodiments of the system 3600 and methods 3800 and 3900, user interfaces, 4000 and 4100, were provided on the workstation 3612 that indicated that the needle tip had reached the target tumor. Once the tumor target was reached, we proceeded to needle fixation, preventing movement due to the CT gantry of respiratory movements that might displace the needle from the target location. A post-procedural scan with breath holding was performed to verify the needle location.

[0254] In the exemplary experimental embodiments of the system 3600 and methods 3800 and 3900, in order to evaluate the accuracy of the needle intervention, we calculated the distance between the manually selected needle tip from the confirmation CT and the target point obtained during surgical planning. Since the rabbit might have moved from the pre-procedural to post-procedural scan, a global image registration was performed afterwards.

[0255] In the exemplary experimental embodiments of the system 3600 and methods 3800 and 3900, as illustrated in FIG. 42A; a user interface 4200a provided on the work station 3612 showed a screen cut of the tumor and the arrow pointed to the target point in the pre-procedural CT.

[0256] In the exemplary experimental embodiments of the system 3600 and methods 3800 and 3900, as illustrated in FIG. 42B, a user interface 4200b provided on the workstation 3612 showed the corresponding slice and the arrow pointed to the needle tip in the confirmation CT. In the exemplary experimental embodiments of the system 3600 and methods 3800 and 3900, as illustrated in FIG. 42C, a user interface 4200c provided on the workstation 3612 showed the registered image. After completing these operations, the distance between the target point and the actual needle tip was calculated. The result was then translated as the needle puncture accuracy.

[0257] In the exemplary experimental embodiments of the system 3600 and methods 3800 and 3900, the experiments were conducted on eight rabbits and they were numbered in the experiment time sequence. The first three experiments were performed without breath holding while the later five were breath holding, by removing the ventilator, cases. The distance between the target point in the pre-CT and the needle tip location in the confirmation CT, after global image registration using the conventional FSL FLIRT program, was used as a metric for the accuracy. Table 5 below lists the results. Overall, the average distance without breath holding was 11 mm, and the average error for the later five experiments with breath holding was 3.5 mm, which meant that the lung movement caused by breathing impacted the accuracy of intervention. After using the breath holding procedure, the accuracy of puncturing was improved up to 70%.

TABLE 5

ACCURACY OF INTERVENTION EXPERIMENTS		
Rabbit	Resolution (mm)	Accuracy
1	(0.27, 0.27, 1.20)	12.45
2	(0.26, 0.26, 1.20)	10.68
3	(0.29, 0.29, 1.20)	10.32
4	(0.28, 0.28, 1.20)	2.93
5	(0.23, 0.23, 1.20)	4.90
6	(0.28, 0.28, 1.20)	4.84
7	(0.28, 0.28, 1.20)	1.25
8	(0.25, 0.25, 1.20)	3.67

[0258] In the exemplary experimental embodiments of the system 3600 and methods 3800 and 3900, in order to validate the effectiveness of the microendoscopic procedure, we collected thirty microendoscopic video clips from the six rabbits' lung tumors to test the precision of the system 3600 and methods 3800 and 3900. As illustrated in FIG. 43A, FIG. 43B, FIG. 43C and FIG. 43D, fluorescence microendoscopic images were captured during the rabbit experiments. The motion of the image sequences, FIG. 43A, FIG. 43B, FIG. 43C and FIG. 43D, were corrected and the intensities were color-coded for better visualization. The histograms, FIG. 44A, FIG. 44B, FIG. 44C and FIG. 44D, of the images, FIG. 43A, FIG. 43B, FIG. 43C and FIG. 43D, respectively, within a one-second sliding window at each time point were also generated. The images, FIG. 43A and FIG. 43B, showed molecular imaging results within the tumor and the images, FIG. 43C and FIG. 43D, showed molecular imaging results at the boundary of the tumor. The histograms, FIG. 44A, FIG. 44B, FIG. 44C and FIG. 44D, illustrate the intensity distributions of the images within temporal sliding windows that were different within and outside the tumor and there was a significantly different contrast or distribution difference between images with non-labeled tissue and  $\alpha_r33$ -labeled tissue. The histograms, FIG. 44A, FIG. 44B, FIG. 44C and FIG. 44D, had peak values of non-labeled tissue images at around 500 and peak values of  $\alpha_r33$ -labeled tissue images at around 1500. Thus, the histograms were classified into two different groups with a threshold value of 1000 providing a metric that indicated a malignant tumor. These exemplary experimental results for the system 3600 and methods 3800 and 3900 were unexpected results.

[0259] As demonstrated by the exemplary experimental embodiments of the system 3600 and methods 3800 and 3900, the system and methods provided a convenient, efficient and accurate interventional tool for on-the-spot diagnosis and treatment of malignant tumors. Furthermore, as validated by the exemplary experimental results using a predictive animal model, the system 3600 and methods 3800 and 3900 permitted a FNAB that can be used to diagnose cancer in humans, where the RFA can also be applied for confirmed malignant cancerous cases. In addition, as demonstrated by the exemplary experimental results using a predictive animal model, the system 3600 and methods 3800 and 3900 is particularly effective for lung tumor intervention and molecular imaging diagnosis. After successfully targeting the tumor, the molecular imaging of the system 3600 and methods 3800 and 3900 can be used for onsite diagnosis, which could be followed by RFA treatment. Furthermore, as demonstrated by the exemplary experimental results using a predictive animal model, the system 3600 and methods 3800 and 3900 permit the design and planning of the needle trajectory

for puncture using an orthogonal viewer, with simultaneous axial, sagittal, and coronal view, which provides a clear perspective regarding the depth and the direction of the needle for reaching the tumor.

[0260] Referring now to FIG. 45A, FIG. 45B, FIG. 45C and FIG. 45D, in exemplary experimental embodiments of the system 3600 and methods 3800 and 3900, normal lung tissue and a malignant tumor within the lung tissue were differentiated from one another permitting a highly accurate diagnosis of a malignant lung tumor. In particular, normal lung tissue, FIG. 45A and FIG. 45B, and malignant lung tumor tissue, FIG. 45C and FIG. 45D, were differentiated from one another. Furthermore, histograms (FIG. 46) of the images obtained during exemplary experimental embodiments of the system 3600 and methods 3800 and 3900, showed a clear and distinct difference between the normal lung tissue and the malignant lung tumor tissue. This was an unexpected result.

[0261] Referring now to FIG. 47, in exemplary experimental embodiments of the system 3600 and methods 3800 and 3900, fluorescent microendoscopic images of  $\alpha$ , $\beta$ <sub>3</sub>-expressing cells (TBR>1.5) were obtained that included an image 4702 on the tumor surface, an image 4704 on a muscle, and an image 4706 in air. As demonstrated by the exemplary images in FIG. 47, the images obtained during exemplary experimental embodiments of the system 3600 and methods 3800 and 3900 showed a clear and distinct difference between the malignant tumor, muscle, and air. This was an unexpected result.

[0262] Referring to now to FIG. 48, in exemplary experimental embodiments of the system 3600 and methods 3800 and 3900, a CARS image 4802a of a normal lung cell, a CARS image 4804a of an Adenocarcinoma lung cancer cell, a CARS image 4806a of an organizing pneumonia cell, a CARS image 4808a of a squamous lung cancer cell and a CARS image 4810a of a small cell lung cancer were obtained. The CARS images obtained, 4802a, 4804a, 4806a, 4808a and 4810a, were also compared with photomicroscopic images of the corresponding cells, 4802b, 4804b, 4806b, 4808b and 4810b, to confirm the differentiation of the cells provided by the system 3600 and methods 3800 and 3900. As demonstrated by the exemplary images in FIG. 48, the images obtained during exemplary experimental embodiments of the system 3600 and methods 3800 and 3900, showed clear and distinct differences between and among the various cell types thereby permitting accurate diagnosis. This was an unexpected result.

[0263] Referring to now to FIG. 49A, FIG. 49B, FIG. 49C and FIG. 49D, in exemplary experimental embodiments of the system 3600 and methods 3800 and 3900, a CARS image 4902 of a normal breast tissue, a CARS image 4904 of normal breast tissue, a CARS image 4906 of a breast tumor and a CARS image 4910 of a breast tumor were obtained. As demonstrated by the exemplary images in FIG. 49A, FIG. 49B, FIG. 49C and FIG. 49D, the images obtained during exemplary experimental embodiments of the system 3600 and methods 3800 and 3900, showed clear and distinct differences between and among the various cell types thereby permitting accurate diagnosis of malignant breast cancer. This was an unexpected result.

[0264] Referring to now to FIG. 50A and FIG. 50B, in exemplary experimental embodiments of the system 3600 and methods 3800 and 3900, a CARS image 5002 of a mouse dorsal prostate was obtained and compared with a photomicroscopic image of the corresponding cells 5004. The CARS

images of the mouse dorsal prostate may be differentiated using CARS images. Thus, the exemplary experimental embodiments of the system 3600 and methods 3800 and 3900, demonstrated that prostate cells may be easily differentiated from non-prostate cells during treatment and surgery. This was an unexpected result.

[0265] Referring to now to FIG. 50C and FIG. 50D, in exemplary experimental embodiments of the system 3600 and methods 3800 and 3900, a CARS image 5006 of the myelin sheath of a mouse body nerve was obtained and compared with a photomicroscopic image of the corresponding cells 5008. The CARS images of nerve sheath cells may be differentiated using CARS images since such cells are rich in CH<sub>2</sub> chemical bonds that may be easily recognized using CARS images. Thus, the exemplary experimental embodiments of the system 3600 and methods 3800 and 3900, demonstrated that nerve cells may be easily differentiated from non-nerve cells during treatment and surgery. This was an unexpected result. This will permit surgeons to avoid cutting into nerve cells during surgery, which is particularly prevalent in conventional prostate surgery. Thus, the system 3600 and methods 3800 and 3900 may be used in surgery to minimize damage to nerves.

[0266] In an exemplary embodiment of the system 3600 and methods 3800 and 3900, specific diseases may be identified based upon the unique attributes of the vibrational frequencies of the chemical bonds: 1) the peak positions which provide a unique chemical fingerprint for each molecule; and/or 2) the peak intensities, which provide concentration information. In particular, as illustrated in FIG. 51, in exemplary experimental embodiments of the system 3600 and methods 3800 and 3900, specific diseases such as, for example, the P22 virus were identified. This was an unexpected result.

[0267] In an exemplary embodiment of the system 3600 and methods 3800 and 3900, lung cancer may be differentiated from normal lung tissue based upon the unique attributes of the vibrational frequencies of the chemical bonds: 1) the peak positions, which provide a unique chemical fingerprint for each molecule; and/or 2) the peak intensities, which provide concentration information. In particular, as illustrated in FIG. 52A, in exemplary experimental embodiments of the system 3600 and methods 3800 and 3900, Raman spectra 5202 for normal bronchial tissue, Raman spectra 5204 for malignant adenocarcinoma, and Raman spectra 5206 for skin squamous-cell carcinoma ("SCC") were obtained. Each of the spectra, 5202, 5204 and 5206, were normalized to the integrated area under each spectra to correct for variations in the absolute spectral intensity. Furthermore, as illustrated in FIG. 52B, difference spectra, 5208 and 5210, for the SCC and the adenocarcinoma, respectively, were then obtained by subtracting the spectra 5202 from the spectra 5206 and 5204, respectively. As illustrated in FIG. 52B, the use of the difference spectra, 5208 and 5210, provides a graphical means for differentiating normal lung tissue from cancerous lung tissue. Furthermore, the difference spectra, 5208 and 5210, further provides a graphical means for differentiating different types of lung cancer. This was an unexpected result.

[0268] In an exemplary embodiment of the system 3600 and methods 3800 and 3900, breast cancer may be differentiated from normal breast tissue based upon the unique attributes of the vibrational frequencies of the chemical bonds: 1) the peak positions that provide a unique chemical fingerprint for each molecule; and/or 2) the peak intensities,

which provide concentration information. In particular, as illustrated in FIG. 53A, FIG. 53B and FIG. 53C, in exemplary experimental embodiments of the system 3600 and methods 3800 and 3900, Raman spectra 5302 for normal breast tissue, Raman spectra 5304 for fibrocystic breast tissue, and Raman spectra 5306 for ductal carcinoma breast were obtained. As illustrated in FIG. 53A, FIG. 53B and FIG. 53C, the spectra obtained provides a graphical means for differentiating between different types of breast tissue. This was an unexpected result.

[0269] In an exemplary embodiment of the system 3600 and methods 3800 and 3900, brain tissues may be differentiated from one another during surgery to permit more precise and safer brain surgery. In particular, as illustrated in FIG. 54, different brain tissues may be differentiated from one another during surgery to, for example, distinguish deep white matter tracts 5402 from other brain tissue. This was an unexpected result.

[0270] In an exemplary embodiment of the system 3600 and methods 3800 and 3900, intermediate special resolution images for gross anatomy and high resolution images may be produced from the same imaging acquisition. In particular, as illustrated in FIG. 55A, a single CARS image was obtained from a region of a mouse brain. FIG. 55B illustrates the same region of the mouse brain different brain using an H&E stain. Note that both images, FIG. 55A and FIG. 55B, provided the observable structures, from upper left corner to bottom right corner, of cortex, corpus callosum, oriens layer, and pyramidal layer. This was an unexpected result.

[0271] In an exemplary experimental embodiment of the system 3600 and methods 3800 and 3900, a human lung cancer cell line (A549) was used to induce lung cancer on a mouse xenograph cancer model. As illustrated in FIG. 56A, normal lung tissue from the mouse xenograph cancer model was imaged. As illustrated in FIG. 56B, cancerous lung tissue from the mouse xenograph cancer model was imaged. As illustrated in FIG. 56C, the margin between normal and cancerous lung tissue from the mouse xenograph cancer model was imaged. In the exemplary experimental embodiments, normal and cancerous lung tissues were imaged at  $2845\text{ cm}^{-1}$  wave number, which corresponds to the excitation peak of intrinsic lipid molecules. In the exemplary experimental embodiments, the cancerous lung tissue provides a CARS signal indicating a lower lipid level, which can be used for differential diagnosis. This was an unexpected result.

[0272] In an exemplary embodiment, during operation of the system 3600 and methods 3800 and 3900, intermediate special resolution images for gross anatomy and high resolution images may be produced from the same imaging acquisition. In particular, as illustrated in FIG. 55A, a single CARS image was obtained from a region of a mouse brain. FIG. 55B illustrates the same region of the mouse brain different brain using a hematoxylin and eosin stain ("H&E"). Note that both images, FIG. 55A and FIG. 55B, provide the observable structures, from upper left corner to bottom right corner, of cortex, corpus callosum, oriens layer, and pyramidal layer. This was an unexpected result.

[0273] The present exemplary embodiments provide systems and methods for: 1) Improving the accuracy and efficiency for intervention procedures such as reduced procedure time and number of repetitive scans needed with more accurate localization; 2) improved diagnostic yield for FNAB, with the fiber-optic imaging guided tumor detection technique; 3) on-the-spot diagnosis and treatment care; and 4) a

percutaneous interventional guidance system for on-the-spot and onsite diagnosis and treatment for small cell lung cancer, particularly for peripheral lung cancer at its early stage.

[0274] Furthermore, the exemplary embodiments improve upon the deficiencies associated with convention treatment in which typical lung cancer diagnoses are only reached after four different imaging studies, both non-invasive and much more invasive, such as percutaneous biopsies and subsequent transthoracic CT-guided needle biopsies. These studies typically take place over the course of days or weeks, and are then followed by treatment. By contrast, the present exemplary embodiment, for example, provide a user-friendly, 3D visualization and navigation platform that allows physicians to quickly and accurately guide a needle to the small nodules of potential cancer in patients' lungs. In the exemplary embodiments, once in the nodule, the physician may use molecular imaging to get a viable tissue sample through a FNAB. Then, in the exemplary embodiments, if cancer is detected, the physician may use RFA to treat the cancer immediately on the spot.

[0275] An endoscopic microscopy apparatus has been described that includes an optical fiber; a collimating lens set operably coupled to one end of the optical fiber; a scanning mirror operably coupled to the optical fiber proximate the collimating lens; an objective lens set operably coupled to the optical fiber; a coupling lens operably coupled to another end of the optical fiber; an optical coupling assembly operably coupled to the coupling lens; a data acquisition system operably coupled to the optical coupling assembly; and a source of a plurality of laser beams operably coupled to the optical coupling assembly. In an exemplary embodiment, the apparatus further includes an optical time delay operably coupled between the source of laser beams and the optical coupling assembly adapted to controllably delaying transmission of one of the laser beams. In an exemplary embodiment, the optical coupling assembly comprises one or more wave division multiplexers. In an exemplary embodiment, the optical coupling assembly comprises a plurality of wave division multiplexers. In an exemplary embodiment, the optical coupling assembly comprises a plurality of wave division multiplexers that are cascaded with respect to one another. In an exemplary embodiment, the apparatus further includes a motion correction system operably coupled to the data acquisition system.

[0276] A method of operating an endoscopic microscopy apparatus has been described that includes operating the apparatus to obtain an image sequence; calculating global registration for one or more of the images; applying the global registration to one or more of the images; calculating deformable registration for one or more of the images; and applying the deformable registration to one or more of the images. In an exemplary embodiment, calculating the global registration for one or more of the images comprises calculating the global registration for one or more of the images by iteratively minimizing an energy equation that is a function of NMI. In an exemplary embodiment, the energy function comprises a linear portion and a non-linear portion.

[0277] In an exemplary embodiment, calculating the global registration for one or more of the images by iteratively minimizing an energy equation that is a function of NMI comprises iteratively estimating an actual transformation one or more of the images. In an exemplary embodiment, calculating the global registration for one or more of the images by iteratively minimizing an energy equation that is a function of

NMI comprises iteratively estimating an actual transformation one or more of the images; and optimizing the estimate of the actual transformation. In an exemplary embodiment, calculating the global registration for one or more of the images by iteratively minimizing an energy equation that is a function of NMI comprises iteratively estimating an actual transformation one or more of the images; and optimizing the estimate of the actual transformation using cubature Kalman filtering. In an exemplary embodiment, calculating the global registration for one or more of the images comprises estimating motion within one or more of the images using line by line searching; dividing one or more of the images into resting and movement time periods; and using a speed embedded hidden Markov model for motion correction of one or more of the images.

[0278] In an exemplary embodiment, calculating the global registration for one or more of the images comprises using a speed embedded hidden Markov model for motion correction of one or more of the images. In an exemplary embodiment, using a speed embedded hidden Markov model for motion correction of one or more of the images comprises defining a state observation probability and a state transition probability. In an exemplary embodiment, using a speed embedded hidden Markov model for motion correction of one or more of the images comprises defining a state observation probability and a state transition probability; and maximizing a value of a function of the state observation probability and the state transition probability. In an exemplary embodiment, using a speed embedded hidden Markov model for motion correction of one or more of the images comprises defining a state observation probability and a state transition probability; maximizing a value of a function of the state observation probability and the state transition probability; and determining a most likely sequence of image offsets.

[0279] In an exemplary embodiment, using a speed embedded hidden Markov model for motion correction of one or more of the images comprises, defining a state observation probability and a state transition probability; maximizing a value of a function of the state observation probability and the state transition probability; determining a most likely sequence of image offsets; and determining an optimal image offset sequence. In an exemplary embodiment, calculating the global registration for one or more of the images comprises preprocessing one or more of the images; training a motion-estimating model for one or more of the images; and estimating a motion correction model for one or more of the images.

[0280] It is understood that variations may be made in the above without departing from the scope of the invention. While specific embodiments have been shown and described, modifications can be made by one skilled in the art without departing from the spirit or teaching of this invention. The embodiments as described are exemplary only and are not limiting. Many variations and modifications are possible and are within the scope of the invention. Furthermore, one or more elements of the exemplary embodiments may be omitted, combined with, or substituted for, in whole or in part, one or more elements of one or more of the other exemplary embodiments. Accordingly, the scope of protection is not limited to the embodiments described, but is only limited by the claims that follow, the scope of which shall include all equivalents of the subject matter of the claims.

1-42. (canceled)

43. A method for diagnosing and treating a patient, comprising:

obtaining one or more CARS images of tissue within the patient; and as a function of one or more attributes of the CARS images, determining if the tissue comprises abnormal or cancer cells, and if the CARS images indicate that the tissue comprises abnormal or cancer cells, then removing at least a portion of the abnormal or cancer cells.

44. (canceled)

45. The method of claim 43, further comprising:

calculating global registration for one or more of the images;  
applying the global registration to one or more of the images;  
calculating deformable registration for one or more of the images; and  
applying the deformable registration to one or more of the images.

46. The method of claim 45, wherein calculating the global registration for one or more of the images comprises:

calculating the global registration for one or more of the images by iteratively minimizing an energy equation that is a function of normalized mutual information.

47. (canceled)

48. The method of claim 46, wherein calculating the global registration for one or more of the images by iteratively minimizing an energy equation that is a function of normalized mutual information comprises:

iteratively estimating an actual transformation one or more of the images

49. (canceled)

50. The method of claim 46, wherein calculating the global registration for one or more of the images by iteratively minimizing an energy equation that is a function of normalized mutual information comprises:

iteratively estimating an actual transformation one or more of the images; and

optimizing the estimate of the actual transformation using cubature kalman filtering.

51. The method of claim 45, wherein calculating the global registration for one or more of the images comprises:

estimating motion within one or more of the images using line by line searching;

dividing one or more of the images into resting and movement time periods; and using a speed embedded hidden markov model for motion correction of one or more of the images.

52-55. (canceled)

56. The method of claim 51, wherein using a speed embedded hidden markov model for motion correction of one or more of the images comprises:

defining a state observation probability and a state transition probability; maximizing a value of a function of the state observation probability and the state transition probability;

determining a most likely sequence of image offsets; and determining an optimal image offset sequence.

57. (canceled)

58. The method of claim 56, further comprising preprocessing one or more of the images by:

segmenting one or more of the images;

serially registering one or more of the images; and

registering a first timepoint images of the images onto a template image.

**59.** The method of claim **56**, further comprising training the motion estimating model for one or more of the images by a process that comprises:

extracting normalized surface motion vectors and corresponding fiducial motion vectors for one or more of the images;

constructing a motion statistical model by performing kernel principal component analysis on the surface motion vectors; and

training the motion estimating model using least squared support vector machine to model a relationship between the fiducial motion vectors and the surface motion vectors on kernel principal component analysis space.

**60.** The method of claim **56**, further comprising estimating the motion correction model for one or more of the images by a process that comprises:

transferring respiratory signals of a patient onto a template space in order to use the motion estimating model to estimate motion vectors and reconstruct surface motion vectors of the patient;

generating serial deformations using the surface motion vectors as constraints in a serial deformation simulator; and

transforming the serial deformations onto a subject space to generate serial images of the patient.

**61-65.** (canceled)

**66.** The method of claim **43**, further comprising:

estimating motion within one or more of the images using line by line searching;

dividing one or more of the images into resting and movement time periods; and

using a speed embedded hidden markov model for motion correction of one or more of the images.

**67.** The method of claim **66**, wherein using a speed embedded hidden markov model for motion correction of one or more of the images comprises: defining a state observation probability and a state transition probability.

**68.** The method of claim **67**, wherein using a speed embedded hidden markov model for motion correction of one or more of the images comprises: defining a state observation probability and a state transition probability; and

maximizing a value of a function of the state observation probability and the state transition probability.

**69.** The method of claim **68**, wherein using a speed embedded hidden markov model for motion correction of one or more of the images comprises:

defining a state observation probability and a state transition probability; maximizing a value of a function of the state observation probability and the state transition probability; and

determining a most likely sequence of image offsets.

**70.** The method of claim **69**, wherein using a speed embedded hidden markov model for motion correction of one or more of the images comprises:

defining a state observation probability and a state transition probability; maximizing a value of a function of the state observation probability and the state transition probability;

determining a most likely sequence of image offsets; and determining an optimal image offset sequence.

**71.** The method of claim **43**, further comprising:

using a speed embedded hidden markov model for motion correction of one or more of the images that includes defining a state observation probability and a state transition probability.

**72.** (canceled)

**73.** The method of claim **71**, wherein using a speed embedded hidden markov model for motion correction of one or more of the images further comprises: maximizing a value of a function of the state observation probability and the state transition probability.

**74.** (canceled)

**75.** The method of claim **73**, wherein using a speed embedded hidden markov model for motion correction of one or more of the images comprises:

defining a state observation probability and a state transition probability; maximizing a value of a function of the state observation probability and the state transition probability;

determining a most likely sequence of image offsets; and determining an optimal image offset sequence.

**76.** A method for identifying an abnormal tissue within the body of a patient, comprising:

obtaining one or more CARS images of one or more tissues within the body of the patient;

preprocessing or segmenting one or more of the images;

training a motion estimating model for one or more of the images;

estimating a motion correction model for one or more of the images.

serially registering one or more of the images;

registering a first timepoint images of the images onto a template image, and

as a function of one or more attributes of the CARS images, determining whether the one or more tissues is abnormal, and if so, determining a course of treatment based on the resulting diagnosis.

**77.** The method of claim **76**, wherein:

(a) preprocessing one or more of the images comprises:

segmenting one or more of the images;

serially registering one or more of the images; and

registering a first timepoint images of the images onto a template image;

(b) training the motion estimating model for one or more of the images comprises:

extracting normalized surface motion vectors and corresponding fiducial motion vectors for one or more of the images;

constructing a motion statistical model by performing kernel principal component analysis on the surface motion vectors; and

training the motion estimating model using least squared support vector machine to model a relationship between the fiducial motion vectors and the surface motion vectors on kernel principal component analysis space;

or

(c) estimating the motion correction model for one or more of the images comprises:

transferring respiratory signals of a patient onto a template space in order to use the motion estimating model to estimate motion vectors and reconstruct surface motion vectors of the patient;

generating serial deformations using the surface motion vectors as constraints in a serial deformation simulator; and

transforming the serial deformations onto a subject space to generate serial images of the patient.

**78-83.** (canceled)

**84.** The method of claim **43**, wherein removing at least a portion of the abnormal or cancer cells includes RF ablation.

**85.** The method of claim **76**, further comprising ablating or surgically removing the one or more abnormal tissues.

\* \* \* \* \*

专利名称(译)	使用相干反斯托克斯拉曼散射 ( CARS ) 的显微内窥镜系统的诊断和治疗方法		
公开(公告)号	<a href="#">US20140031697A1</a>	公开(公告)日	2014-01-30
申请号	US13/838628	申请日	2013-03-15
[标]申请(专利权)人(译)	公会医院RES INST		
当前申请(专利权)人(译)	循道卫理医院研究所		
[标]发明人	WONG STEPHEN T C WANG ZHIYONG PALPATTU GANESH GAO LIANG		
发明人	WONG, STEPHEN T.C. WANG, ZHIYONG PALPATTU, GANESH GAO, LIANG		
IPC分类号	A61B5/00 A61B18/18		
CPC分类号	A61B18/18 A61B5/0075 A61B1/00009 A61B1/00165 A61B1/00172 A61B1/063 A61B1/07 A61B5/0066 A61B5/0084 A61B5/6847 A61B5/7207 A61B6/12 A61B6/486 G01N21/65 G01N2021/653 G06K9/00134 G06T7/30		
优先权	61/399182 2010-07-08 US 61/399139 2010-07-08 US		
外部链接	<a href="#">Espacenet</a> <a href="#">USPTO</a>		

摘要(译)

公开了一种用于收集和处理图像序列以便提供诊断和治疗的内窥镜微观系统。还公开了在各种诊断和治疗应用中制备和使用该系统的方法。

